INSTITUTE
FOR
AEROSPACE STUDIES

UNIVERSITY OF TORONTO

COUPLED INTERACTIONS OF SHOCK-WAVE STRUCTURE WITH LAMINAR BOUNDARY LAYER IN IONIZING-ARGON SHOCK-TUBE FLOWS

by

K. Takayama and W. S. Liu

March, 1979

UTIAS Report No. 233
CN ISSN 0082-5255

COUPLED INTERACTIONS OF SHOCK-WAVE STRUCTURE WITH LAMINAR BOUNDARY LAYER IN IONIZING-ARGON SHOCK-TUBE FLOWS

by

K. Takayama and W. S. Liu

Submitted February, 1979

March, 1979

UTIAS Report No. 233
CN ISSN 0082-5255

Acknowledgements

The project was carried out under the direction of Dr. I. I. Glass, whose advice and support throughout the course of this work are gratefully acknowledged.

The financial assistance received from the National Research Council of Canada and the Air Force Office of Scientific Research under Grant No. AF-AFOSR 77-3303 is acknowledged with thanks.

The financial support received by one of us (K. Takayama) while on sabbatical leave from the Institute of High Speed Mechanics, Tohoku University, Sendai, Japan, from a Government of Canada Fellowship and by UTIAS are very much appreciated.

Summary

Analyses are made of the mutual interactions between shock structure and the sidewall laminar boundary-layer and their effects on the quasi-steady flat-plate laminar boundary layer in ionizing argon shock-tube flows. The mutual interactions are studied using effective quasi-one-dimensional equations derived from an area-averaged-flow concept in a finite-area shock tube. The effects of mass, momentum and energy non-uniformities and the wall dissipations in the ionization and relaxation regions on the argon shock structure are discussed. The new results obtained for shock structure, shock-tube laminar sidewall and quasi-steady flat-plate boundary-layer flows are compared with dual-wavelength interferometric data obtained from the UTIAS 10 cm x 18 cm Hypervelocity Shock Tube. It is shown that the difference between the results obtained from the present method and those obtained by Enomoto based on Mirels' perfect-gas boundary-layer solutions are significant for lower shock Mach numbers ($M_s \sim 13$) where the relaxation lengths are large ($\sim$ 10 cm). In general, the present results agree better with our experimental data than our previous results for uncoupled ionizing flows.

CONTENTS

Notation

A	shock-tube cross-sectional area
C	$\frac{\rho_w \mu_w}{\rho_\delta \mu_\delta}$
C_f	local skin friction coefficient
c_p	specific heat at constant pressure
D	$\frac{4A}{L}$ hydraulic diameter
D_m	ambipolar-diffusion coefficient
H	plasma total enthalpy
k	Boltzmann constant
L	shock-tube perimeter
M_s	shock-wave Mach number
m_a	atomic mass of argon
Nu	local Nusselt number
n_e	electron-number density
$\dot{n}_e$	electron-number density production-rate
p	pressure
Q_{el}	elastic energy-transfer rate to electrons
Q_{inel}	inelastic energy-transfer rate to electrons
Q_R	radiation energy loss
$\dot{q}$	shock-tube sidewall heat conduction rate
q_c	plasma heat conduction energy flux
q_d	plasma diffusive-energy flux
q_{ce}	electron heat-conduction energy-flux
q_{de}	electron diffusive-energy flux

R	gas constant
Re	Reynolds number
T	temperature
T_I	characteristic ionization temperature
t	time
u	velocity component in x-direction
V	particle velocity
$\vec{v}$	velocity component in y-direction
x	distance along shock-tube sidewall
y	distance normal to shock-tube sidewall

α	degree of ionization
γ	specific heat ratio
δ	boundary layer thicknesses; see Eqs. (28a)~(28j)
δV_i	ion-diffusive velocity
λ	thermal-conduction coefficient
μ	mixture viscosity coefficient
ρ	total-plasma density
τ	shear stress

Subscripts

a	atom
e	electron
i	ion
w	conditions at the shock-tube sidewall
o	conditions in front of shock wave
δ	condition at the boundary layer edge

Operator

$\langle f \rangle = \frac{1}{A} \int f \, dA$ area-averaged values

1. INTRODUCTION

In our previous analyses of ionizing shock-wave structures (Glass et al, Refs. 1, 2) and the ionizing boundary-layer flows induced by a strong shock wave (Liu et al, Refs. 3, 4), the coupled effects between inviscid and viscous flows in a shock tube were neglected. As shown by Glass and Patterson (Ref. 5) and Mirels (Ref. 6), the flow between the shock wave and the contact surface in an actual shock tube is nonuniform owing to the growth of the shock-tube sidewall boundary layer. The gross features of shock-wave structure in an ionizing gas are affected by the sidewall boundary layer. Consequently, the induced ionizing boundary layers on a flat plate in the so-called quasi-uniform flows are affected by these mutual interactions. This nonuniformity has to be considered when interpreting shock-tube data in aerodynamic or chemical-kinetic studies.

The important effects of the growth of the sidewall boundary layer on the freestream flow are the induced wall shearing stress, heat transfers and the consequent nonuniformities in the flow. In order to take into account the flow nonuniformities in a shock-tube, Mirels (Refs. 6, 7, 8) has obtained correlation formulae for a perfect gas, which are often used by many researchers in gasdynamics. These relations are based on similarity solutions of the boundary-layer equations treating the boundary layer as an aerodynamic sink. Local-similarity assumptions cannot be applied to those cases where the variations of the freestream-flow quantities are important and cannot be neglected. As shown by Liu et al (Refs. 3, 4) the similarity assumption is not valid for the electron-temperature and electron-number-density profiles for the sidewall-boundary-layer flow where ionizing nonequilibrium phenomena occur in the freestream flow behind the shock front and the variations of the freestream conditions for the sidewall boundary layer are significant. Also, only mass conservation was considered by Mirels in the study of flow nonuniformity. The effects of the sidewall boundary layer on the freestream momentum and energy equations were neglected. The validity of Mirels' correlation formulae cease to apply to an ionizing-gas flow, although they were used by Enomoto (Ref. 9), McLaren and Hobson (Ref. 10) and Brabbs and Belles (Ref. 11) in their studies of shock structure in an ionizing gas. Enomoto studied the sidewall boundary-layer effects on ionizing shock structure in argon. He applied Mirels' (Ref. 6) perfect-gas-correlation formulae for flow nonuniformity of the mass mixture. Flow nonuniformities in the momentum and energy equations were entirely neglected without giving any reasons. Nevertheless, he found the important physical result that the relaxation length is significantly reduced in tubes of decreasing cross-sectional area owing to the sidewall-boundary-layer growth.

The sidewall boundary-layer growth generates both compression and rarefaction wavelets. However the net effect is that of a rarefaction wave which attenuates the shock front; see Trimpi and Cohen (Ref. 12). Flow uniformity in ionizing gases in the relaxation regions induced by incident and reflected shock waves is still far from being completely understood. In principle, the analytical approach can be made by taking into account the interaction between the boundary-layer growth and the development of a two or three-dimensional inviscid-flow model as well as by taking into account their interaction with unsteady flow effects such as shock-wave attenuation or contact surface acceleration.

For example, Hubbard and de Boer (Ref. 13) studied two-dimensional flow nonuniformities in a perfect gas based on the basic assumption that the

boundary-layer parameters do not change very much in the region where two-dimensional effects are of importance. They showed that the flow in the inviscid region is nearly one-dimensional at a distance from the shock front greater than the shock-tube radius. Demmig (Ref. 14) studied one-dimensional ionization relaxation in krypton under influences of weakly attenuating shock fronts and sidewall boundary-layer effects. He calculated the flow field behind an experimentally determined attenuating shock front by taking into account only the boundary-layer displacement thickness growth in a way similar to Enomoto's method. He showed the combined effects of boundary-layer growth and shock-wave attenuation on the ionizing krypton shock-wave structure at a shock Mach number of about 10.

In the usual one-dimensional model, the boundary layer is assumed thin compared to the shock-tube radius and is replaced by a sink distribution. The inviscid core is assumed to be quasi-one-dimensional in the sense that flow variations are assumed to occur only in the streamwise direction. However, as Glass et al (Ref. 2) showed experimentally that the electron-cascade front approaches the translational shock front near the sidewall, the mutual interaction between ionization mechanisms and the flow field is not simple.

In the present analysis, the inviscid core field is assumed to be effectively one-dimensional by using an area-averaging process instead of treating the boundary layer as a sink distribution as for the perfect-gas case.

The purpose of this work is to extend our previous studies of shock-wave structure and boundary-layer flows for ionizing argon by including the mutual interactions between the inviscid freestream and viscous sidewall boundary-layer flows. The present study of the mutual interactions is based on the effective one-dimensional-flow equation derived from the flow area-averaged concept, where the flow nonuniformities in the freestream mass, momentum and energy equations and the wall dissipation terms are considered. A finite-difference scheme is applied to the ionizing boundary-layer equations. An examination is made of the role of the sidewall-boundary-layer growth on the behaviour of the shock-structure ionization and radiation-cooling regions.

The results of the quasi-steady flat-plate and the sidewall boundary-layer flow induced by a strong shock wave in a finite area shock tube are re-examined and compared with our dual-wavelength interferometric boundary-layer data obtained from the UTIAS 10 cm x 18 cm Hypervelocity Shock Tube. It is shown that the difference between the results obtained from the present method and the simplified Mirels' one-dimensional equations are even more significant at lower shock Mach number where the relaxation lengths are larger. In general, the present analysis gives much better agreement with our experimental data by taking into account the mutual interactions between the inviscid and viscous flows.

2. THEORETICAL CONSIDERATIONS

2.1 Basic Equations

Two methods have been widely applied in obtaining the effective quasi-one-dimensional-flow equations in gas mixtures: (1) control volume method, and (2) flow area-averaged method. In the control volume method, the integral form of the conservation law is applied to the mixture control volume.

The effective equations are obtained by introducing definitions of area-averaged properties and limiting the length of the control volume to zero. In the flow averaged method, local instantaneous conservation equations are obtained from the law of conservation. The effective quasi-one-dimensional-flow equations are obtained by applying an area-average on the local instantaneous conservation equations. Identical results are obtained from both methods for a homogeneous gas-mixture flow.

In this work, the effective quasi-one-dimensional-flow equations for an ionized gas in a shock tube are directly obtained by applying the flow area-average on the local instantaneous macroscopic balance equations. Consider a gas mixture made up of atoms, singly-ionized ions and electrons. The macroscopic balance equations for the plasma mixture are given by Appleton and Bray (Ref. 16) as follows:

Mass conservation:

$$\frac{\partial}{\partial t}\rho + \nabla \cdot (\rho\vec{V}) = 0 \tag{1}$$

Plasma momentum equation:

$$\frac{\partial}{\partial t}\rho\vec{V} + \nabla \cdot (\rho\vec{V}\vec{V}) + \nabla P = \nabla \cdot (\mu\nabla\vec{V}) \tag{2}$$

Plasma energy conservation:

$$\frac{\partial}{\partial t}\rho H + \nabla \cdot (\rho\vec{V}H) = -\nabla \cdot (\vec{q}_c + \vec{q}_d) + \nabla(\vec{V} \cdot \mu\nabla\vec{V}) - Q_R \tag{3}$$

Electron mass conservation:

$$\frac{\partial}{\partial t}\alpha\rho + \nabla \cdot (\alpha\rho\vec{V}) = m_a\dot{n}_e + \nabla \cdot (\rho D_m \nabla\alpha) \tag{4}$$

Electron energy conservation:

$$\frac{\partial}{\partial t}\alpha\rho C_p T_e + \nabla \cdot (\rho\vec{V}\alpha C_p T_e) = (\vec{V} + \delta\vec{V}_i)\nabla p_e$$

$$- \nabla \cdot (\vec{q}_{ce} + \vec{q}_{de}) + Q_{el} + Q_{inel} \tag{5}$$

where the definitions of the variables and other terms are the same as those in Refs. 1 and 2.

Consider a mixture in a constant area of a shock tube with cross-sectional area A. Integration of Eqs. (1)-(5) over the flow area A at any

instant in time gives:

$$\int_A \frac{\partial \rho}{\partial t}\, dA + \int_A \nabla\cdot(\rho\vec{V})dA = 0 \tag{6}$$

$$\int_A \frac{\partial}{\partial t}\, \rho\vec{V}\, dA + \int_A \nabla\cdot(\rho\vec{V}\vec{V} + p)dA = \int_A \nabla\cdot(\mu\nabla\vec{V})dA \tag{7}$$

$$\int_A \frac{\partial}{\partial t}\, \rho H dA + \int_A \nabla(\rho H\vec{V})dA = -\int_A \nabla(\vec{q}_c + \vec{q}_d)dA + \int_A \nabla(\vec{V}\cdot\mu\nabla\vec{V})dA - \int_A Q_R dA \tag{8}$$

$$\int_A \frac{\partial}{\partial t}\, \alpha\rho dA + \int_A \nabla\cdot(\alpha\rho\vec{V})dA = m_a \int_A \dot{n}_e dA + \int_A \nabla\cdot(\rho D_m \nabla\alpha)dA \tag{9}$$

and

$$\int \frac{\partial}{\partial t}\, (\alpha\rho C_p T_e)dA + \int \nabla\cdot(\rho\vec{V}\alpha C_p T_e)dA = \int_A (\vec{V} + \delta\vec{V}_i)\cdot\nabla p_e dA$$

$$-\int_A \nabla\cdot(\vec{q}_{ce} + \vec{q}_{de})dA + \int_A (Q_{el} + Q_{inel})dA \tag{10}$$

where the conduction- and diffusive-energy flux are given by:

$$\begin{aligned} q_c &= -(\lambda_a + \lambda_i)\nabla T_a - \lambda_e \nabla T_e \\ q_d &= -(RT_I + C_p T_e)\rho D_m \nabla\alpha \\ q_{ce} &= -\lambda_e \nabla T_e \\ q_{de} &= -C_p T_e \rho D_m \nabla\alpha \end{aligned} \tag{11}$$

Using the special forms of the Leibnitz and Gauss theorems and taking the dot product to get the x-component yields:

Mass conservation:

$$\frac{\partial}{\partial t} \langle\rho\rangle + \frac{\partial}{\partial x} \langle\rho u\rangle = 0 \tag{12}$$

Plasma momentum equation:

$$\frac{\partial}{\partial t}\langle \rho u \rangle + \frac{\partial}{\partial x}\langle \rho u^2 + p \rangle = -\langle \tau \rangle_w$$

$$\frac{\partial}{\partial y} p = 0 \tag{13}$$

Plasma energy conservation:

$$\frac{\partial}{\partial t}\langle \rho H \rangle + \frac{\partial}{\partial x}\langle \rho u H \rangle = \langle \dot{q} \rangle_w - \langle u\tau \rangle_w - \langle Q_R \rangle \tag{14}$$

Electron mass conservation:

$$\frac{\partial}{\partial t}\langle \rho\alpha \rangle + \frac{\partial}{\partial x}\langle \alpha\rho u \rangle = m_a \langle \dot{n}_e \rangle - \left\langle \rho D_m \frac{\partial \alpha}{\partial y} \right\rangle_w \tag{15}$$

Electron energy conservation:

$$\frac{\partial}{\partial t}\langle \rho\alpha C_p T_e \rangle + \frac{\partial}{\partial x}\langle \rho u \alpha C_p T_e \rangle = \left\langle (u + \delta u_i) \frac{\partial p_e}{\partial x} \right\rangle$$

$$+ \langle Q_{el} + Q_{inel} \rangle + \langle \dot{q}_e \rangle_w \tag{16}$$

where the operator $\langle f \rangle = \frac{1}{A}\int_A f dA$ is introduced, and the boundary-layer approximation with neglecting terms of $O(\delta^2)$ is made.

The wall dissipation terms are defined as follows:

$$\langle \tau \rangle_w = \frac{L}{A}\left(\mu \frac{\partial u}{\partial y} \right)_w$$

$$\langle \dot{q} \rangle_w = \frac{L}{A}(q_c + q_d)_w$$

$$\left\langle \rho D_m \frac{\partial \alpha}{\partial y} \right\rangle_w = \frac{L}{A}\left(\rho D_m \frac{\partial \alpha}{\partial y} \right)_w \tag{17}$$

$$\langle u\tau \rangle_w = \frac{L}{A}\left(\mu u \frac{\partial u}{\partial y} \right)_w$$

$$\langle \dot{q}_e \rangle_w = \frac{L}{A}(q_{ce} + q_{de})_w$$

Equations (12)-(16) are the basic equations for the unsteady area-averaged flow model. Demmig (Ref. 14) studied the effects of boundary layer growth and unsteady shock-wave motion on ionizing krypton shock-wave structure by solving Eqs. (12)-(16). He took into account only the boundary layer displacement thickness growth in Eq. (12), neglecting other boundary layer effects and the wall dissipation terms in Eqs. (13)-(16) as well as a radiation-energy loss term in Eq. (14). He calculated the flow structure behind an experimentally obtained attenuating shock wave by an inverse method, so that important unsteady effects propagating across the contact front were not taken into account. In his experiments, the shock wave Mach number varied from 10.6 to 10.1 over a distance of 2.27 m in a 5.2 cm x 5.2 cm shock tube. On the other hand, in the UTIAS 10 cm x 18 cm Hypervelocity Shock Tube, the shock attenuation rates $\Delta M_s/L$ are about 0.2 (Mach number/m) for shock Mach numbers $M_s = 13$ and 16. Therefore, throughout the present analysis, it is acceptable that the shock front propagates with constant velocity and shock-fixed coordinates are applicable.

In the shock-fixed coordinate, the quasi-one-dimensional flow equations are obtained from Eqs. (12)-(16):

Mass conservation:

$$\frac{d}{dx}\langle \rho u \rangle = 0 \tag{18}$$

Plasma momentum equation:

$$\frac{d}{dx}\langle \rho u^2 + p \rangle = -\frac{L}{A}\left(\mu \frac{\partial u}{\partial y}\right)_w \tag{19}$$

where the pressure, p, is constant across the cross sectional area of the shock tube.

Plasma energy conservation:

$$\frac{d}{dx}\langle \rho u H \rangle = \langle \dot{q} \rangle_w - \langle Q_R \rangle - \frac{1}{A}\left(\mu u \frac{\partial u}{\partial y}\right)_w \tag{20}$$

Degree of ionization:

$$\frac{d}{dx}\langle \rho u \alpha \rangle = m_a \langle \dot{n}_e \rangle - \frac{L}{A}\left(\rho D_m \frac{\partial \alpha}{\partial y}\right)_w \tag{21}$$

Electron energy conservation:

$$\frac{d}{dx}\langle \rho u \alpha C_p T_e \rangle = \left\langle (u + \delta u_i) \frac{dp_e}{dx} \right\rangle$$

$$+ \langle Q_{el} + Q_{inel} \rangle - \langle \dot{q}_e \rangle_w \tag{22}$$

The sidewall boundary layer effects are thus taken into consideration in the area-averaged terms of the above equations. Equations (18)-(22) finally become (for details of the derivation see Appendix A):

Mass conservation:

$$\frac{d}{dx}\,\rho u(A - \delta^* L) = 0 \tag{23}$$

or

$$\rho u(A - \delta^* L) = \rho_o u_s A \tag{23a}$$

Plasma momentum equation:

$$\frac{d}{dx}\,\rho u^2(A - \delta_m L) + A\,\frac{dp}{dx} = -\,L\left(\mu\,\frac{\partial u}{\partial y}\right)_w \tag{24}$$

Plasma energy conservation:

$$\frac{5}{2}\,\frac{d}{dx}\,pu(A - \delta_u L) + RT_I\,\frac{d}{dx}\,\rho u\alpha(A - \delta_\alpha L) + \frac{1}{2}\,\frac{d}{dx}\,\rho u^3(A - \delta_e L)$$

$$= L\dot{q}_w - Q_R(A - \delta_R L) - L\left(\mu u\,\frac{\partial u}{\partial y}\right)_w \tag{25}$$

Electron mass conservation:

$$\frac{d}{dx}\,\rho u\alpha(A - \delta_\alpha L) = m_a \dot{n}_e(A - \delta_n L) - L\left(\rho D_m\,\frac{\partial \alpha}{\partial y}\right)_w \tag{26}$$

Electron energy conservation:

$$\frac{3}{2}\,R\,\frac{d}{dx}\,\rho u\alpha T_e(A - \delta_{T_e} L) + \rho\alpha R T_e(A - \delta_{n_e} L)\,\frac{d}{dx}\,u(A - \delta_u L)$$

$$= (Q_{el} + Q_{inel})(A - \delta_Q L) - L\dot{q}_{ew} \tag{27}$$

The various boundary layer thicknesses defined and used in Eqs. (22)-(27), which are related to the known definitions of the boundary layer thicknesses (for example, Schlichting, Ref. 18), are given as follows:

Displacement thickness:

$$\delta^* = \int\left(1 - \frac{\rho' u'}{\rho u}\right) dy \tag{28a}$$

where the primed variables are those across the boundary layer [see Eq. (A3)]:

Momentum thickness:

$$\delta_m = \int \left(1 - \frac{\rho' u'^2}{\rho u^2} \right) dy = \delta^* + \int \frac{\rho' u'}{\rho u} \left(1 - \frac{u'}{u} \right) dy \qquad (28b)$$

Velocity thickness:

$$\delta_u = \int \left(1 - \frac{u'}{u} \right) dy \qquad (28c)$$

Degree of ionization thickness:

$$\delta_\alpha = \int \left(1 - \frac{\rho' u' \alpha'}{\rho u \alpha} \right) dy = \delta^* + \int \frac{\rho' u'}{\rho u} \left(1 - \frac{\alpha'}{\alpha} \right) dy \qquad (28d)$$

Energy-dissipation thickness:

$$\delta_e = \int \left(1 \frac{\rho' u'^3}{\rho u^3} \right) dy = \delta^* + \int \frac{\rho' u'}{\rho u} \left(1 - \frac{u'^2}{u^2} \right) dy \qquad (28e)$$

Radiation energy loss thickness:

$$\delta_R = \int \left(1 - \frac{Q_R'}{Q_R} \right) dy \qquad (28f)$$

Reaction rate thickness:

$$\delta_{\dot{n}} = \int \left(1 - \frac{\dot{n}_e'}{\dot{n}_e} \right) dy \qquad (28g)$$

Electron number density thickness:

$$\delta_{n_e} = \int \left(1 - \frac{n_e'}{n_e} \right) dy \qquad (28h)$$

Electron energy-transfer rate thickness:

$$\delta_Q = \int \left(1 - \frac{Q_{el}' + Q_{inel}'}{Q_{el} + Q_{inel}} \right) dy \qquad (28i)$$

Electron temperature thickness:

$$\delta_{T_e} = \int \left(1 - \frac{\rho' u' \alpha' T_e'}{\rho u \alpha T_e} \right) dy = \delta^* + \int \frac{\rho' u'}{\rho u} \left(1 - \frac{\alpha' T_e'}{\alpha T_e} \right) dy \qquad (28j)$$

As shown in the shock-tube sidewall boundary-layer analysis in ionizing argon by Liu et al (Refs. 3, 4), if the electron temperature is assumed constant across the boundary layer, the electron temperature thickness δ_{T_e} is approximately equal to the degree of ionization thickness δ_α, that is,

$$\delta_{T_e} \approx \delta_\alpha$$

It should be noted that in the shock-fixed coordinate δ^*, δ_m, δ_u and δ_e are negative and δ_R, $\delta_{\dot{n}_e}$, δ_{n_e} and δ_Q are positive, whereas the sign of δ_α depends on the type of boundary-layer flow, that is, frozen or nonequilibrium. The growth and details of these boundary-layer thicknesses are shown in Appendix B. The dissipation terms - shearing stress at the shock-tube sidewall; wall heat transfers due to the mixture of atoms, ions and electrons, and the energy deposition at the wall due to the diffusion of ions - are explained in Appendix B.

It is worth noting that the existence of the electron-cascade front in the ionizing inviscid core gives rise to the nonuniform boundary-layer development with distance quite differently from the boundary-layer development in perfect argon. Some of the defined boundary-layer thicknesses are maxima or minima at the electron-cascade front and eventually influence the shock-wave structure.

Enomoto (Ref. 9) first showed that the relaxation distance was reduced due to the existence of the shock-wave induced sidewall boundary layer. His analytical model accounted for the effects due only to the displacement thickness of the sidewall boundary layer. His boundary-layer displacement thickness was based on Mirels' similar boundary-layer analysis for perfect argon (Ref. 6):

$$A - \delta^* L = A \left\{ 1 - \left(\frac{x}{\ell_m} \right)^N \right\}^{-1} \qquad (29)$$

where $N = 0.5$ for the laminar boundary-layer flow and ℓ_m is the separating distance between an incident shock wave and a contact front calculated from the formulas given by Mirels (Ref. 6). However, Enomoto disregarded the other mutual interaction terms such as the other boundary-layer thicknesses and the wall dissipation terms which appeared in the source terms of the quasi-one-dimensional equations, Eqs. (24)-(27). He also neglected the radiation energy loss term Q_R in the energy conservation equation.

The same discussions are applicable to Demmig's model (Ref. 14). He studied ionizing krypton shock-wave structures at shock Mach number of about 10 and initial pressure of 8 torr. He considered the effects of the growth of a sidewall boundary layer as well as effects of unsteady shock-wave behaviour, and solved the unsteady one-dimensional flow equations by applying the characteristic method to the so-called inverse problem with an experimentally given shock-wave trajectory. However, even in his boundary-layer model, only the growth of the boundary-layer displacement thickness obtained from the similar boundary-layer analysis for perfect krypton was considered. Other boundary-layer effects as well as wall dissipation terms used in the present study are neglected. Further, although shock attenuation effects were considered in Demmig's analysis, the radiation energy-loss term Q_R, was neglected in the energy conservation equation.

The boundary-layer displacement thickness that Demmig obtained from an analysis given by Dem'yanov (Ref. 15) is written as

$$A - \delta^* L = A \left\{ 1 - \frac{5.44}{\sqrt{dRe}} \left(\int U_s dt - x \right)^{1/2} \right\} \tag{29a}$$

where $\int U_s dt - x$ is the distance from the unsteady shock front, d and Re are the diameter of the shock tube and the Reynolds number referring to the inviscid uniform flow region and d, respectively. Dem'yanov (Ref. 15) assumed a velocity profile across the boundary layer as

$$\frac{u}{u_\delta} = \frac{3}{2} \left(\frac{\eta}{\eta_\delta} \right) - \frac{1}{2} \left(\frac{\eta}{\eta_\delta} \right)^3$$

where $\eta = \int \frac{\rho}{\rho_\delta} dy$ and η_δ corresponds to η at the outer edge of the boundary layer. He used the above mentioned velocity profile and solved the nonuniformity flow behind a shock wave.

Brabbs et al (Ref. 11) used the same formula as Eq. (29) to demonstrate the effects of flow nonuniformities induced by a laminar sidewall boundary layer on the chemical kinetic study in a shock tube. Belles et al (Ref. 17) also used the same formula for a turbulent boundary layer by putting N = 0.8 in Eq. (29).

Consequently, only the mass conservation equation, Eq. (23), is common to Enomoto's basic equations. In the present study the displacement thickness, other boundary layer thicknesses and wall dissipation terms were obtained by solving the two-dimensional ionizing boundary-layer equations. The profiles along the shock-tube sidewall distance were significantly different from those resulting from a similar boundary-layer analysis such as given by Mirels (Ref. 6). These profiles used in this study are shown in Appendix B.

Details of an implicit six-point finite difference method for solving the two-temperature nonequilibrium boundary-layer equations in ionizing argon were given by Liu et al (Refs. 3, 4). Comparison between the first-order results where the mutual interaction between inviscid shock-wave structures and boundary-layer flows were not taken into account, and the experimental data for both quasi-steady flat-plate and sidewall boundary-layer flows were also given.

Once all the boundary layer thicknesses and wall dissipation terms are known from the analysis of the boundary-layer flows in ionizing argon, Eqs. (23)-(27) can be numerically solved. Glass et al (Refs. 1, 2) solved Eqs. (23)-(27) for shock-wave structures in ionizing argon and krypton where contributions from the sidewall boundary layers and the wall dissipation terms were not taken into consideration. The results were compared with interferometric data in some details in Refs. 1 and 2.

By rearranging Eqs. (23)-(27) we have

$$\frac{d\alpha}{dx} = \frac{A - \delta_n L}{A - \delta_\alpha L} m_a \frac{\dot{n}_e}{\rho u} + \alpha \frac{d}{dx} \ell n \frac{A - \delta^* L}{A - \delta_\alpha L} - \frac{A}{A - \delta_\alpha L} \frac{L}{A\rho u} \left(\rho D_m \frac{\partial \alpha}{\partial y} \right)_w \quad (30)$$

$$\frac{1}{u} \frac{du}{dx} = \left\{ \frac{5}{2} \frac{A - \delta_m L}{A} \frac{d}{dx} \ell n \frac{A - \delta^* L}{A - \delta_m L} + \frac{5}{2} \frac{p}{\rho u^2} \frac{d}{dx} \ell n (A - \delta_u L) \right.$$

$$+ \frac{A - \delta_n L}{A - \delta_u L} \cdot \frac{RT_I}{u^2} \frac{m_a \dot{n}_e}{\rho u} - \frac{1}{2} \frac{A - \delta_e L}{A - \delta_u L} \frac{d}{dx} \ell n \frac{A - \delta^* L}{A - \delta_e L} + \frac{Q_R}{\rho u^3} \frac{A - \delta_R L}{A - \delta_u L}$$

$$\left. + (\text{dissipation terms}) \right\} \Big/ \left\{ \frac{5}{2} \left(\frac{A - \delta_m L}{A} - \frac{p}{\rho u^2} \right) - \frac{A - \delta_e L}{A - \delta_u L} \right\} \quad (31)$$

where

$$(\text{dissipation terms}) = - \frac{5}{2} \frac{L}{A\rho u^2} \left(\mu \frac{\partial u}{\partial y} \right)_w + \frac{A}{A - \delta_u L} \frac{L}{A\rho u^3} \left\{ \left(\mu u \frac{\partial u}{\partial y} \right)_w \right.$$

$$\left. - (\lambda_a + \lambda_i) \left(\frac{\partial T_a}{\partial y} \right)_w - \left(\lambda_e \frac{\partial T_e}{\partial y} \right)_w - RT_I \left(\rho D_m \frac{\partial \alpha}{\partial y} \right)_w \right\}$$

The momentum conservation equation is given by

$$\frac{1}{\rho u^2} \frac{dp}{dx} = \frac{A - \delta_m L}{A} \left(\frac{d}{dx} \ell n \frac{A - \delta^* L}{A - \delta_m L} - \frac{1}{u} \frac{du}{dx} \right) - \frac{L}{A\rho u^2} \left(\mu \frac{\partial u}{\partial y} \right)_w \quad (32)$$

The electron energy equation is rewritten as

$$\frac{1}{T_e} \frac{dT_e}{dx} = \frac{2}{3} \frac{A - \delta_u L}{A - \delta_\alpha L} \cdot \frac{A - \delta_{n_e} L}{A} \left(\frac{d}{dx} \ell n \frac{A}{A - \delta_m L} - \frac{1}{u} \frac{du}{dx} \right) + \frac{2}{3} \frac{A - \delta_Q L}{A - \delta_\alpha L} \frac{Q_{el} + Q_{inel}}{\rho u \alpha R T_e}$$

$$+ \frac{A}{A - \delta_\alpha L} \frac{L}{A\rho u} \left\{ \frac{8}{3} \left(\rho D_m \frac{\partial \alpha}{\partial y} \right)_w + \frac{2}{3RT_e} \left(\lambda_e \frac{\partial T_e}{\partial y} \right)_w \right\} \quad (33)$$

Since the electron energy-transfer rate due to inelastic collisions is larger than that due to elastic collisions in the electron temperature range now under discussion, the following approximation can be made across the boundary layer:

$$\frac{Q'_{el} + Q'_{inel}}{Q_{el} + Q_{inel}} \sim \frac{Q'_{inel}}{Q_{inel}} = \frac{(\dot{n}_e)'_e}{(\dot{n}_e)_e}$$

since $Q'_{el} < Q'_{inel}$, and $Q_{el} < Q_{inel}$.

Consequently, from the definitions of the boundary-layer thicknesses, Eqs. (28g) and (28i), it is possible to assume the following relationship:

$$\delta_Q \approx \delta_{\dot{n}} \tag{34}$$

Variations of both δ_Q and $\delta_{\dot{n}}$ along the shock-tube sidewall are compared for $M_s = 13.1$ and 15.9 in Appendix B, Fig. B8. Finally, by introducing the above approximation, Eq. (34), we can rewrite the electron energy-transfer rate due to the inelastic collision as follows (Glass et al, Ref. 2):

$$Q_{inel} = - k(\dot{n}_e)_e \left(T_I + \frac{3}{2} T_e \right) \tag{35}$$

Equations (29)-(32) together with the mass conservation equation, Eq. (23a) and the equation of state

$$p = \rho R(T_a + \alpha T_e) \tag{36}$$

can be numerically solved with given initial conditions by using, for instance, the Runge-Kutta-Gill method. It is worth noting that if the mutual interactions between inviscid and viscous flows are not taken into consideration, the above-mentioned equations are exactly consistent with the basic equations of Glass et al (Ref. 2).

2.2 Initial Conditions

If all the boundary layer properties and the wall dissipation terms are known from a shock-tube sidewall boundary-layer analysis, the basic equations of shock-wave structures, Eqs. (30)-(33), (23a) and (36), can be solved for the unknowns p, T_a, T_e, u, α and ρ with the following initial conditions:

$$\frac{u}{\sqrt{\gamma R T_o}} = \frac{(\gamma - 1)M_s^2 + 2}{(\gamma + 1)M_s^2}$$

$$\frac{p}{p_o} = \frac{2\gamma M_s^2 - (\gamma - 1)}{\gamma + 1}$$

$$\frac{T_a}{T_o} = \frac{p}{\rho} \frac{1}{R T_o} \tag{37}$$

$$\frac{T_e}{T_o} = 1$$

$$\alpha = 0$$

and

$$\frac{\rho}{\frac{p_o}{R T_o}} = \frac{(\gamma + 1)M_s^2}{(\gamma - 1)M_s^2 + 2}$$

where $\gamma = 5/3$ and the subscript o denotes the condition in front of the shock wave in the shock-fixed coordinate.

2.3 Numerical Procedures

The procedures of the present iteration scheme are described as follows:

(1) Calculate the first-order ionizing shock-wave structure by neglecting the mutual interaction terms such as the boundary-layer thicknesses and the wall dissipation terms.

(2) Using these shock-wave structure results, obtain all the boundary-layer thicknesses and wall dissipation terms by solving the laminar boundary-layer equations in ionizing argon.

(3) Applying these boundary-layer thicknesses and wall dissipation terms, solve the area-averaged quasi-one-dimensional shock-wave-structure equations.

(4) Repeat procedures (2) and (3) until the iterative solutions converge to a given criterion.

There is no guarantee that the present iterative scheme will converge. However, from our experience the solutions converge quite quickly, within two or three iterations.

As an example, variations of the boundary-layer displacement thickness with distance x at each iteration number are shown in Figs. 1(a) and 1(b) for shock-wave Mach numbers 13.1 and 15.9. It is found that the solutions almost converge at the iteration numbers of 2 for $M_s = 15.9$ and 3 for $M_s = 13.1$.

2.4 Discussions

In the present study, an iterative scheme for solving Eqs. (23)-(27) together with the boundary-layer equations was proposed. The shock-wave structures, sidewall boundary-layer flows and the quasi-steady flat-plate boundary-layer flows were re-examined and compared with the experiments given in Refs. 1~4.

In the summary of the theoretical considerations, the following differences are pointed out between the present study and the previous works:

(1) In the previous works by Enomoto (Ref. 9) for ionizing argon, Demmig (Ref. 14) for ionizing krypton and Brabbs (Ref. 11) for chemical kinetic studies, the boundary-layer effects are represented only by the boundary-layer displacement thickness. The mutual interactions between the inviscid shock-wave structure and the boundary-layer flows, such as various boundary-layer thicknesses as well as the wall dissipation terms in the momentum and energy conservation equations and so on, are considered in this work.

(2) Similar solutions obtained by Mirels (Ref. 6) were applied by Enomoto and others in the evaluation of the boundary-layer displacement thickness. In the present study the exact boundary-layer equations were solved by an implicit six-point finite difference scheme. In addition, the variations of transport

properties across the boundary layer were taken into consideration.

There were no concurrent analyses or experiments to show that Mirels' formulation (Ref. 6) of the boundary-layer effects was a proper basis for making corrections to the previous analytical results or experimental data for ionizing gases. Enomoto made use of Mirels' boundary-layer formulation to study the ionizing argon shock-wave structure. There were still large differences between his analysis and the experiments.

3. EFFECTS OF SIDEWALL BOUNDARY LAYER ON SHOCK-WAVE STRUCTURE

3.1 General Considerations

In our previous studies of ionizing argon shock-wave structure (Glass et al, Ref. 2), it was shown that the experiments for higher shock-wave Mach number ($M_S \approx 16$) are in good agreement with the analysis. However the agreement between analysis and experiments was not satisfactory for the lower shock Mach number case ($M_S \approx 13$) comparing ionization relaxation lengths and the electron number density at the electron cascade front. Enomoto (Ref. 9) showed that due to the boundary-layer displacement thickness effect, the ionizing relaxation length was reduced and, especially in the lower shock-wave Mach number, reduction of the relaxation length became significant. However, his postulated analytical model seems to be physically oversimplified. In this chapter the results are compared with the experimental data and the previous analyses.

3.2 Comparison of Numerical Results with Experimental Results

Figure 2 shows comparisons between the various analyses and the interferometric experimental data given by Glass et al (Refs. 1, 2), for the electron number density profile of the lower shock-wave Mach number, $M_S \approx 13$. The result of the first order solution neglecting the sidewall boundary-layer effects, is shown by curve A. Curve B shows the result obtained by taking into account only the boundary-layer displacement thickness effects, calculated from the similar boundary-layer analysis for frozen argon; this is similar to Enomoto's model. Coefficients of the growth of the boundary-layer displacement thickness $-\delta^*/\sqrt{x}$ are shown in Fig. B2 of Appendix B. The boundary-layer displacement thickness used in curve B is written as follows:

$$-\delta^* = 0.1006\sqrt{x} \text{ for } M_s = 13.1,\ p_o = 5.16 \text{ torr and } T_o = 300 \text{ K},$$

and

$$-\delta^* = 0.1064\sqrt{x} \text{ for } M_s = 15.1,\ p_o = 5.10 \text{ torr and } T_o = 298 \text{ K}.$$

Curve C is the first iterative result of the present method where the boundary layer equations were solved exactly, and not only the displacement thickness but also other boundary layer effects and the wall dissipation terms were applied in the analysis of shock-wave structures. Curve D shows the higher order iterative result of the present method. It is obvious that the difference between the present results (curve D) and Enomoto's model (curve B) is significant for this lower shock Mach number.

The relaxation length, x_E, is drastically reduced in Enomoto's model, $x_E = 7.8$ cm, and the corresponding result for the first-order model is about 10 cm, whereas the present method gives $x_E = 8.93$ cm. The experimental value

is about $x_E = 9.0$ cm. The agreement between the present analysis and the experimental data is significantly improved at lower shock-wave Mach number $M_s = 13.1$. These results are tabulated in Table 1(a) and 1(b) and compared with other results with different parametric values.

The electron number density at the electron-cascade front predicted by using Enomoto's model gives a much higher value than that predicted by the present analysis. The reduction of the relaxation length and the overshoot of the electron number density in Enomoto's model can be explained as follows. In the first-order analysis neglecting the mutual interaction effects the mass flux ρu is always smaller than $\rho_o u_s$ as shown in Eq. (23a):

$$\rho u < \rho u \frac{A - \delta^* L}{A} = \rho_o U_s \tag{38}$$

where the boundary-layer displacement thickness ($\delta^* < 0$) acts as though it enlarges the shock-tube cross-sectional area in the shock fixed coordinate.

The production of the electron number density, described in Eq. (26), is as follows:

$$\frac{dn_e}{dx} \sim \frac{m_a \dot{n}_e}{\rho u} > \frac{m_a \dot{n}_e}{\rho_o U_s} \tag{39}$$

Therefore the quasi-equilibrium peak value of the electron number density is roughly proportional to the inverse of the mass flux ρu. In Enomoto's model, the relaxation length is always shortened and the degree of ionization is overreached. However, in the present model the overshoot of the degree of ionization is comparatively suppressed and consequently the relaxation length is not so drastically shortened as Enomoto's model predicts.

The comparison between the analyses and the experimental data of the total plasma density is plotted in Fig. 3. The total plasma density initially increases gradually from its frozen value, suddenly increases near the electron-cascade front, and then reaches the quasi-equilibrium value as shown by arrows in Fig. 3. The total plasma density gradient is a maximum near the electron-cascade front where the electron number density production rate $\dot{n}_e$ is a maximum. Due to the radiation energy loss, the total plasma density slowly increases behind the electron-cascade front. This will be explained later together with the interpretation of the pressure profiles. It is shown that much better agreement between the present model and experiments is obtained.

A comparison of the degree of ionization is also shown in Fig. 4. The relaxation length is reduced by about 12% due to the sidewall boundary layer effects at this lower shock-wave Mach number $M_s = 13.1$. Arrows on the curves and the experimental data indicate termination of the relaxation length. Good agreement between the present model and the experiment is obtained with respect to the relaxation length. However, the predicted quasi-equilibrium values determined from the present model, curve D, are larger than the experimental results by about 25%. The general tendency of the data points is similar to the prediction and they are almost parallel to the curve D at the quasi-equilibrium region. The reason for this discrepancy between the analysis and experiments in

the lower shock Mach number case is not clear. However, as found later for the case of higher shock Mach number, agreement of α/α_E between the analysis and experiments is good. In the present analysis, the most reasonable formulae and the most reliable coefficients to them are used for the excitational cross-section for atom-atom and electron-atom collisions, the momentum transfer cross-sections for electron-atom and electron-ion collisions and the radiation energy loss term (Ref. 2). There may be analytically undetermined factors in estimating these cross-sections and the radiation energy loss term. Therefore, it is not clear how these unknown factors depend on the shock Mach number.

Normalized pressure profiles p/p_o, and temperature profiles are shown in Figs. 5 and 6, respectively. Curves A, B and D correspond to the first-order results, Enomoto's model, and the present model, respectively.

In the first-order results the pressure initially increases gradually from its frozen value, and then suddenly increases to its quasi-equilibrium value. The pressure gradient is a maximum near the electron-cascade front where the electron number density production rate $\dot{n}_e$ is a maximum. Over the quasi-equilibrium region, the pressure still increases slowly. The reasons are explained in the following argument.

If we rewrite Eq. (31) by taking into account only the boundary-layer displacement thickness for the sake of simplicity,

$$\frac{1}{u}\frac{du}{dx} \sim \frac{2\frac{d}{dx}\ell n(A - \delta^* L) + \frac{RT_I}{u^2}\frac{m_a \dot{n}_e}{\rho u} + \frac{Q_R}{\rho u^3}}{1.5\left(1 - \frac{1}{M^2}\right)} \tag{40}$$

where $M^2 = \rho u^2/\gamma p < 1$ gives the local flow Mach number behind the shock front which is less than unity in the shock-fixed coordinate. The pressure gradient is also written as

$$\frac{1}{\rho u^2}\frac{dp}{dx} \sim -\frac{1}{u}\frac{du}{dx} > 0 \tag{41}$$

As shown in Eq. (40), the velocity gradient is composed of contributions from (1) the sidewall boundary-layer displacement thickness growth $d/dx\ \ell n(A - \delta^* L)$, (2) the electron number density production rate, $\dot{n}_e$, and (3) the radiation-energy losses Q_R. Initially the contribution from the boundary-layer displacement thickness effects are greater. Near the electron-cascade front the contribution from the electron number density production rate is more prominent. Finally, behind the electron-cascade front the contribution from the radiation-energy loss is significant.

Since the flow field behind the shock front in the shock-fixed coordinates is subsonic, and the boundary-layer displacement thickness acts to expand the cross-sectional area of a shock tube, the sign of velocity gradient, Eq. (40), is always negative. Physically this indicates that due to subsonic flow behind the shock wave in the shock-fixed coordinate, the above mentioned effects encourage the

velocity profile $U_s - u$ to keep on decreasing with distance x. In other words, the particle velocity u is increasing with distance from the shock front in the laboratory-fixed coordinate (see Glass et al, Ref. 2). Therefore, as obviously seen from the momentum equation, Eq. (41), the pressure should keep on increasing with distance behind the shock front. The curves B and D in Fig. 5 show comparatively sharp initial pressure rises from the frozen value as a result of taking into account the boundary-layer growth effects. The present results (curve D) lie between the first-order results (curve A) and Enomoto's model (curve B) except at the beginning.

The same interpretation is applicable to the total plasma density profile. The total plasma density is inversely proportional to the velocity; see Eq. (23a). Consequently, the atom temperature T_a and the electron temperature T_e are over-reached in curve D as shown in Fig. 6, and are very much over-reached in Enomoto's model, curve B. Atom and electron temperature-overshoots subsequently give rise to more atom-atom collisions and as a result the electron number density in front of the electron cascade front increases. Therefore the relaxation length is significantly reduced. It is found that Enomoto's model gives an overestimation to the reduction of the relaxation length. This interpretation is of course consistent with the previous one that the reduction of the relaxation length can be explained from the point of view of boundary layer displacement thickness growth and the reduction of the mass flux.

It is worth noting that an initial sharp pressure rise and a temperature overshoot are peculiar to the analysis where the growth of boundary-layer displacement thickness is taken into account. Demmig (Ref. 14) studied combined effects of the sidewall boundary-layer displacement thickness and the unsteady shock-wave motion on ionizing krypton shock wave structure. He showed that the temperature overshoot occurs despite shock-wave attenuation.

One of the interesting features of ionizing argon shock wave structures is the existence of an incubation period in which a gas particle passes from the translational shock front to the electron-cascade front. In the incubation period, no significant changes in the flow properties occur but internal electronic states are excited and the electron number density is very slightly increasing. After this period all the flow properties change very suddenly. The electron-cascade front appears. Therefore it is physically acceptable that any change in the dynamic flow properties such as a pressure rise induced by the boundary-layer growth would sharply influence the whole shock wave structure and eventually reduce the relaxation length.

Experimental data obtained from shock tubes with various configurations are compared by means of using the hydraulic diameter D. Here we compared our predicted values with experimental data obtained by the UTIAS 10 cm x 18 cm Hypervelocity Shock Tube, so that we employ the standard $D = 4A/L = 12.86$ cm for a 10 cm x 18 cm shock tube.

In order to examine the shock tube diameter effects on the ionizing shock wave structure, computations were done for these different diameter shock tubes: $D_{0.5} = 6.43$ cm, $D_{1.0} = 12.86$ cm, $D_{2.0} = 25.73$ cm and $D_\infty \to \infty$. The computational results for the infinite shock tube diameter D_∞ is equivalent to those of the first order analysis since, as shown in Eqs. (23)-(27), the terms representing the mutual interaction effects are inversely proportional to the hydraulic diameter. On the other hand, in a small diameter shock tube the mutual interaction effects are even greater, and in the extreme case of a very small diameter

shock tube, the area-averaged quasi-one-dimensional analysis is no longer valid. In this case, a two or three-dimensional flow model and the subsequent strong shock attenuation effect should be considered. Sometimes a very small diameter shock tube is used as a common shock tube or a detonation tube. For example, Enomoto (Ref. 9) compared the reduction of relaxation length from a one-inch diameter shock tube. However, it is not clear whether the present method can be applied to this small diameter shock tube or not. In Table 1(a) the quasi-equilibrium peak value of α_E, n_{eE}, ρ_E and the relaxation length x_E are tabulated at $M_s = 13.1$, $p_o = 5.16$ torr and $T_o = 300$ K for various shock-tube diameters. In addition both nonequilibrium and frozen boundary-layer profiles are compared. However it is known from the results of the shock-tube sidewall boundary layer that the nonequilibrium profile is closer to the experimental data (see Chapter 4 of this report and Liu and Glass, Ref. 4). Therefore, the higher-order iteration is applied only in the nonequilibrium flow.

Figure 7 shows the result of the electron number density for the various hydraulic diameters where n_{eE} is the equilibrium electron number density for $D_{1.0} = 12.86$ cm. As shown in Fig. 7, the relaxation length decreases and the electron number density at the electron-cascade front increases as the shock-tube diameter is made smaller.

As a second example at higher shock-wave Mach number $M_s = 15.9$, the experimental and analytical results for the electron number density are shown in Fig. 8. In this case the difference between the present model (as shown in curve D) and Enomoto's model (curve B) is smaller than that in the previous low shock-wave Mach number case $M_s = 13.1$. The reason is that effects of the various boundary layer thicknesses and wall dissipation terms on the shock-wave structure are not so important since the quasi-equilibrium temperature is higher and the relaxation length is shorter, $x_E = 2$ cm for the higher shock Mach number $M_s = 15.9$.

In Fig. 9 the total-plasma density profiles are shown. Good agreement is obtained between the present model and the experiments. Results for the degree of ionization profile are shown in Fig. 10 for comparison. Pressure and temperature profiles are shown in Figs. 11 and 12, respectively. The same remarks as for the lower shock Mach number are applied to this case. The quasi-equilibrium peak values are shown in Table 1(b) for various shock-tube diameters. The effects of the shock-tube diameter on the shock-wave structure are plotted in Fig. 13. As expected, effects of the shock-tube diameter on the shock-wave structure are smaller, since the relaxation length is shorter in this case so that the time duration in which the boundary layer influences the structure is shorter. It is found that the profiles for a $D_{2.0}$ shock tube and an infinite diameter shock tube are almost the same. The profile for a $D_{1.0} = 12.86$ cm shock tube is very close to that for D_∞. This shows that the UTIAS Hypervelocity Shock Tube gives almost one-dimensional shock-wave structures at higher shock Mach numbers. In the first-order analysis, the relaxation length is 2.15 cm, whereas in the present model $x_E = 2.03$ cm after the iteration number of 2. Consequently, at this higher shock wave Mach number, the boundary-layer effect reduces the relaxation length by only 6% whereas it is about 12% at the previous lower shock wave Mach number.

3.3 Discussions

Comparing our area-averaged quasi-one-dimensional model with Enomoto's model and the first-order analysis as well as interferometric data, the following discussions are pointed out:

(1) The formerly selected value of argon-argon collisional cross-section constant of 10^{-19} eV/cm^2 (Glass et al, Ref. 2), which was used throughout the present study, is accurate. The argon-argon collisional cross-section constant is known to affect the relaxation length. Good agreement was obtained between experiments and the present analysis for both M_s = 13.1 and 15.9.

(2) The relaxation length is significantly reduced due to the sidewall boundary-layer growth as predicted by Enomoto (Ref. 9). The reduction of the relaxation length is more pronounced for the lower shock-wave Mach number (M_s = 13.1) where the length is much longer ($x_E \approx 9.0$ cm) than that (x_E = 2.0 cm) for the higher shock-wave Mach number (M_s = 15.9).

(3) The model suggested by Enomoto over-predicted the effect of boundary-layer growth on the shock-wave structure. Therefore the application of Mirels' method to ionizing gas flows is inadequate, except for a rough estimation of the effects of the sidewall boundary layer on the shock-wave structure.

(4) The effect of the sidewall boundary layer on the shock-wave structure is more pronounced in a shock tube of smaller diameter. For higher shock-wave Mach numbers the reduction of the relaxation length is small enough for us to conclude that the UTIAS 10 cm x 18 cm Hypervelocity Shock Tube, with which the present experiments were conducted, is large enough for us to ignore the effect of the boundary layer on experiments in ionizing argon flows.

4. SHOCK-TUBE SIDEWALL BOUNDARY-LAYER FLOWS

4.1 General Considerations

Shock-tube sidewall boundary-layer flows in ionizing argon, without taking into account the mutual interactions between the inviscid and the viscous flows, were analyzed and compared with dual-wavelength interferometric data by Liu et al (Refs. 3, 4). Satisfactory agreement was obtained for the low-Mach-number case, M_s = 13.1. The experimental results lie between the frozen and nonequilibrium solutions. However, it was found that two-dimensional effects are significant for the higher Mach number case, M_s = 15.9. The phenomenon of the electron-cascade front moving toward the wall to approach the translational shock wave was found more prominent for stronger shock waves by Glass et al (Ref. 2). The reasons for this premature ionization and relaxation process close to the wall are still unknown.

The present sidewall boundary-layer results were obtained by using the shock-structure solutions described previously as the edge conditions of the boundary layer. The difference between the previous model by Liu et al (Ref. 4) without taking into account the mutual interactions and the present results arises from the variations of freestream flow properties. As expected, a change in the freestream flow conditions will cause changes in the boundary-layer flows.

4.2 Comparison of Numerical and Experimental Results and Discussions

Figure 14 shows the corresponding first order and present results for M_s = 13.1, p_o = 5.16 torr and T_o = 300 K together with the experimental data for the total-plasma-density profiles, ρ/ρ_δ, where δ denotes the conditions outside the boundary layer. Curve A shows the first-order results for the nonequilibrium

boundary layer; curve B shows the present results for the nonequilibrium boundary layer and curve C shows the first-order results for the frozen boundary layer. The difference between the first-order and the present coupled results is small since it was shown before by Liu et al (Refs. 3, 4) that the total plasma-density profile is not a sensitive indicator of boundary-layer structure. However, the difference between the first-order and the present results for the electron-number-density profiles can be readily seen in Fig. 15, even though the difference is small. As drawn in curve B, the experimental data are closer to the present results. This shows that the experimental boundary-layer profile for $n_e/n_{e\delta}$ is closer to the nonequilibrium profile. In this case the sidewall boundary-layer profiles are measured at x = 9.5 cm behind the shock front. The relaxation length is about 9.0 cm as predicted in the present model and in experiments. Therefore, curve B still shows strong influence from the electron-cascade front where the profile is very much different from the similar profile in Liu et al (Ref. 4). The same tendency is observable in the degree of ionization profile plotted in Fig. 16. It is evident that the present results agree better with the experimental data than with the first-order results for lower shock Mach number, where premature ionization and recombination close to the wall is not significant in the experiments (see Glass et al, Ref. 2). The premature ionization is discussed later in some detail.

Figure 17 shows the first-order and present results for the higher shock Mach number case M_s = 15.9 and p_o = 5.10 torr for the total plasma density ρ/ρ_δ. The agreement between the present result and experimental data is not as good as expected in the lower shock Mach number case. The electron number density profiled are shown in Fig. 18. The present results (curve B) lie between the nonequilibrium profile (curve A) and the frozen profile (curve C), and apart from the experimental data. The experimental data differ from the analytical results outside the boundary layer edge at $Y \geq 2$ mm. This obviously shows the two-dimensional effect of the ionizing shock-wave structure in higher shock Mach number (see Glass et al, Ref. 19).

A tendency similar to the electron-number-density profile is shown in Fig. 19 for the degree of ionization α/α_δ. The agreement of the present results with the experimental data is worse. The reason for the discrepancy between the lower and higher shock Mach number cases is argued as follows. It was shown by Glass et al (Ref. 2) that coupled sinusoidal disturbances occur at higher shock Mach numbers in the translational shock front as well as in the electron cascade front and beyond. Recently the flow profiles in the direction normal to the wall were measured by Glass et al (Ref. 19) in the inviscid flow region. It was found that the flow is nonuniform in the inviscid region at this high Mach number M_s = 16. In the experiment, the electron-number density as well as the degree of ionization increased with distance Y from the wall and did not reach asymptotic values at the outer edge of the boundary layer Y = 14 mm, whereas the total-plasma density decreased from the wall and reached its asymptotic value at the edge of the boundary layer. However, it decreased again when the distance from the wall was greater than 8 mm. This flow nonuniformity behind a moving shock wave at higher shock Mach numbers results mainly from radiation energy transfer. The radiation energy losses are prominent in the inviscid core with respect to the nonequilibrium boundary-layer flow (see Fig. B6).

The two-dimensional effects on the shock structure cannot be predicted simply by using the quasi-one-dimensional models as used in the previous and present analysis. Further analysis such as using the unsteady two-dimensional

model may be tried in order to know propagation of disturbances induced by radiation-energy transfer. In addition to this, although we have argued about the optically thin argon plasma, it may be necessary in a future study to take into account effects of reabsorption of the radiation energy loss in the inviscid core as well as in the boundary layer. This effect is very difficult to include because the reabsorption coefficient is a function of the complete structure of the radiation cooling zone. This effect was not included in the present analysis (see Liu et al, Ref. 3).

Figures 20(a) and 20(b) show experimental contours of constant degree of ionization α for shocks (M_s = 16.5 and M_s = 13.6) redrawn from Glass et al (Ref. 2). The solid lines indicate the outer edge of the degree of ionization boundary layer $\alpha/\alpha_\delta = 0.99$, obtained from the present sidewall boundary-layer analysis for (a) M_s = 16.6, p_o = 4.81 torr, T_o = 296 K and α_E = 15.7%, and (b) M_s = 13.1, p_o = 5.16 torr, T_o = 300 K and α_E = 6.4%. These small discrepancies of initial conditions between analyses and experiments do not lead to significant errors in comparing both results. The boundary-layer thickness for degree of ionization reaches a maximum at a distance where the electron number density production rate $\dot{n}_e$ is a maximum, and then temporarily decreases. The reasons for this strange behaviour of the degree of ionization can be explained as follows.

Boundary-layer flows are first assumed to be similar just behind the shock front. Boundary-layer flows become nonequilibrium gradually as x increases. In the electron-cascade front, the flow properties are much different from the similar original flow properties since the electron-number-density production rate and the radiation-energy losses are greatest there, as shown in Fig. 16, for example. Consequently, the boundary-layer profiles are also changed sharply with distance x near the electron-cascade front. Far behind the electron-cascade front, the boundary-layer profiles recover to the weak nonequilibrium profiles, since radiation-energy losses are prominent and new uniform flow conditions are established, for example, Fig. 4. The transition of the boundary-layer profile from a strong nonequilibrium profile to a new similar profile occurs just behind the electron cascade front. In addition the degree of ionization decreases from its quasi-equilibrium value in the inviscid core. Therefore the boundary-layer thickness of the degree of ionization ($\alpha/\alpha_\delta = 0.99$) temporarily decreases, as shown in Fig. 20(a). It is found that the overshoot in the α profile across the boundary layer occurs just behind the electron-cascade front for the following reasons. The velocity boundary layer as well as the boundary-layer displacement thickness develop almost monotonically with distance x by the same mechanism as in the flat-plate boundary-layer case [see Figs. B1(a) and B1(b)]. Their growths are also encouraged by acceleration of particle velocity in the inviscid core. The temperature in the inviscid core decreases so sharply at the electron-cascade front that the temperature boundary layer cannot develop as quickly as the velocity boundary layer. The temperature boundary layer decreases temporarily. Consequently, for total enthalpy to be maintained across the boundary layer, the temperature profile across the boundary layer should have an overshoot. As a result, this temperature overshoot across the boundary layer induces the overshoot of degree of ionization profile at the electron-cascade front.

It is clear that this overshoot significantly affects the boundary-layer thickness of the degree of ionization, δ_α, defined by Eq. (28d). In Fig. B5, variations of δ_α with distance x are shown for shocks with M_s = 15.9 and 13.1. It is worth noting that due to this overshoot profile, δ_α can be

a maximum near the electron-cascade front in the case of the nonequilibrium boundary layer. However, in the frozen boundary layer, the overshoot of α is not found. For details see Appendix B.

Arrows with figures along $\alpha/\alpha_\delta = 0.99$ curves in Fig. 20(a) show the degree of ionization (%) at the marked points. The value of α along the curve $\alpha/\alpha_\delta = 0.99$ increases monotonically from 0% at the shock front to 4% at x = 1.25 cm. Then it suddenly increases across the electron-cascade front and reaches a maximum of $\alpha = 15.7\%$. It is shown that experimental α contours indicate the α overshoot at the electron-cascade front. The agreement of α between the present analysis and experiments is very good at and behind the electron-cascade front; but it is poor in the incubation region between the shock front and the electron-cascade front, since the 2% contour intersects with the $\alpha/\alpha_\delta = 0.99$ curve where the predicted values are less than 1%. The reason for this discrepancy is not clear. The same remarks can be applied to the lower shock Mach number case, $M_s = 13.1$ as drawn in Fig. 20(b).

Agreement between experimentally obtained α contours and predicted $\alpha/\alpha_\delta = 0.99$ curves is very good. It is worth noting that the premature ionization near the sidewall is merged with the predicted degree of ionization boundary layer.

It is known that far behind the electron-cascade front the degree of ionization and electron-number density in experiments do not approach their asymptotic values but still increase beyond the outer edge of the boundary layer for higher shock Mach number $M_s = 15.9$. Glass et al (Ref. 17) studied these phenomena and concluded that a two-dimensional effect is mainly due to the radiation energy transfer mechanism. The details are still far from clear. Experimental indications, for example in Fig. 20(a), show that the degree of ionization profile across the boundary layer at the electron-cascade front $x \approx 17$ mm initially increases with distance Y from the sidewall. Then it reaches the quasi-equilibrium peak value $\alpha_E = 15.8\%$. Finally it gradually decreases in the inviscid core $Y > 2$ mm since the experimental α contours are concave to the shock front. It is found that this profile shows a completely different tendency from that far behind the electron-cascade front at x = 18 cm as shown by Glass et al (Ref. 19) or in Fig. 19. The reasons for this difference are explained as follows. The α profile across the shock tube is affected by the boundary-layer growth, radiation energy losses and ionization and recombination rate processes. Since these effects themselves and their coupled effects vary significantly with distance x, it is quite acceptable to assume that the experimental α profile measured at the electron-cascade front is very different from that measured far behind the electron-cascade front.

In an actual unsteady two-dimensional flow, especially behind the electron-cascade front, disturbances generated by the boundary-layer growth, radiation energy losses and ionization and recombination processes are nonuniformly propagating along the characteristic surfaces. These nonuniformly propagating disturbances interact with the electron-cascade front as well as the shock front. However, it is far from clear how these disturbances interact two-dimensionally with the electron-cascade front and how they are related to the sinusoidal configuration of a perturbed shock front, as found by Glass et al (Ref. 2). Although the premature ionization near the sidewall is found to be merged with the degree of ionization boundary layer, their detailed interpretations are still far from being completed. It will be an important future research task to understand their origin and interactions with ionizing argon shock-tube flows.

Deckker et al (Ref. 20), applying the hot wire anemometry to shock-tube flows, showed that flow property distributions are not uniform close to the shock front even at very low shock Mach number $M_s = 1.16$ (the pressure ratio across the shock front $P_{21} = 1.57$). Velocity and temperature profiles are found to be different from those profiles predicted by the similar boundary-layer analyses. Although a critical examination of the reproducibility of their shock-tube experiments and disturbing effects of the probe on the subsonic shock-tube flow is needed, the question arises as to which mechanisms cause the flow nonuniformity close to the shock front. They concluded that the flow nonuniformity may be due to the unsteady effects of the shock-tube flow, especially due to the propagation of disturbances generated at the contact front.

Further experiments and more sophisticated analyses applying the unsteady two or three-dimensional Navier-Stokes equations to the ionizing argon shock-tube flow are necessary to understand the flow nonuniformity.

5. QUASI-STEADY FLAT-PLATE BOUNDARY-LAYER FLOWS

5.1 General Discussions

The first-order results of quasi-steady flat-plate boundary-layer flows generated by a strong shock wave in a shock tube for ionizing argon were given and compared with dual-wavelength interferometric data by Liu et al (Ref. 3). Satisfactory agreement was obtained between analysis and experimental total plasma-density and electron-number density profiles for shocks $M_s = 13.1$ and 15.9.

Two cases reported previously, $M_s = 12.8$, $p_o = 5.01$ torr and $T_o = 297$ K, and $M_s = 16.6$, $p_o = 4.81$ torr and $T_o = 298$ K, are re-analysed by using the present method. The difference between the previous result by Liu et al (Ref. 3) and the present analysis arises from the changes in the free-stream flow conditions which result from mutual interactions between inviscid and viscous flows.

5.2 Comparison of Numerical and Experimental Results and Discussions

Figure 21 shows comparisons between analyses and experimental data for the case with $M_s = 16.6$, $p_o = 4.81$ torr and $T_o = 297$ K for the total-plasma-density. The difference between the present analysis and the first-order results is quite small. The corresponding results for the electron-number density $n_e/n_{e\delta}$ and degree of ionization profiles α/α_δ are plotted in Figs. 22 and 23, respectively. A bump appears in the experimental data for the electron-number density profile and in the present analysis, but the maximum deviation from the asymptotic value of $n_e/n_{e\delta} \to 1$ is very small, at most 2%. The disagreement between analysis and experiments for the electron-number density results mainly from the fact that the boundary-layer flow is assumed to be quasi-steady while in the experiments it is unsteady due to radiation-energy losses. That is, the electron-number density and degree of ionization are slowly decreasing with distance from the electron-cascade front and the pressure, particle velocity and total plasma density are slightly increasing with distance from the electron-cascade front, as discussed in Chapter 3. However, variations of these flow properties with distance x were not considered in the present flat-plate boundary-layer flow in order to satisfy

the steady-state conditions. The boundary-layer displacement thickness growths are shown with distance x in Fig. 24 for both nonequilibrium and frozen boundary-layer flows. As expected in the steady flat-plate flow, the displacement thickness grows almost proportional to the square root of the distance from the leading edge of the flat-plate, whereas in the sidewall boundary layer, bumps appear at the electron-cascade front. The boundary-layer displacement thickness in the frozen flow is thinner than that in the nonequilibrium flow, although the Reynolds numbers referring to the inviscid core flow properties are the same. The reason is that in the nonequilibrium boundary-layer flow, kinetic energy is spent for internal electronic excitation of argon atoms as well as for ionization processes. As a result, a temperature gradient and other flow property gradients across the boundary layer are comparatively smoothed out. For example, Figs. 23 and 24 show the electron number density and degree of ionization profiles, respectively. Therefore the nonequilibrium boundary-layer displacement thickness is thicker than that of the frozen flow.

In Table 2 comparisons of the uniform conditions between the first-order results and the present results are tabulated. The differences between these results are not significant. The local flow Mach numbers M_δ are increased by about 3% for $M_s = 16.6$ and by about 5% for $M_s = 12.8$. For the latter case, $M_s = 12.8$, the nonequilibrium and frozen flow profiles for total plasma density ρ/ρ_δ and for electron-number density are shown in Figs. 25 and 26, respectively, together with experimental data. A small improvement is found. The experimental results for the electron-number density lie between the analytical nonequilibrium and the frozen-flow profiles. The corresponding results for the degree of ionization are shown in Fig. 27.

Figure 28 shows variations of nonequilibrium and frozen boundary-layer displacement thicknesses with distance x for lower shock Mach number $M_s = 12.8$. It is found that the frozen boundary-layer displacement thickness is much thinner than that of the nonequilibrium flow. Effects of ionization and recombination processes are more significant in the lower shock Mach number, as shown in Figs. 26 and 27. Comparing the result for $M_s = 12.8$ with the higher shock Mach number $M_s = 16.6$, it is found that the growth of the boundary-layer displacement thickness for the lower shock Mach number is much slower than that for the higher shock Mach number. The Reynolds numbers referring to the inviscid freestream properties are different in each case.

It is shown that effects of the mutual interactions between the inviscid and viscous flows on the quasi-steady flat-plate boundary-layer flows are small. However, the flow model used in the present analysis is a quasi-steady one. Unsteady effects appearing in the experiments are not considered in the analysis. Therefore, in order to obtain better agreement between analysis and experiments, the unsteady two-dimensional Navier-Stokes equations should be solved with proper unsteady inviscid freestream conditions. They are, of course, one of the important research tasks for the future.

6. DISCUSSIONS AND CONCLUSIONS

An analysis is presented of the mutual-interaction effects of ionizing-argon shock-wave structure and shock-tube sidewall as well as flat-plate boundary-layer flows. The effective quasi-one-dimensional shock-wave-structure equations for a tube of finite area are derived from the flow area-averaged concept. Flow nonuniformities resulting from the boundary-layer-displacement thickness and

other defined thicknesses, as well as the wall dissipation terms, are included in the shock-wave-structure analysis. The results are compared with a previous first-order analysis and interferometric data at nominal shock Mach numbers of 13 and 16 at an initial pressure of 5 torr. It is shown that a perfect-gas analysis based only on displacement thickness overestimates the reduction in shock-wave-structure thickness. However, a real-gas analysis shows that the actual shock-wave structure thickness is closer to the idealized one-dimensional case. In addition, the interferometric measurements of the electron-number density and total-plasma density shock-wave-structure profiles as well as the derived degree of ionization profiles are in much better agreement with the present analysis than those done previously. The same remarks apply to the ionizing sidewall as well as flat-plate boundary-layer interferometric profiles. Agreement of the experimental data with the present analysis is very good for both the shock-wave structure and the boundary layer at $M_s \sim 13$ and good at $M_s \sim 16$. It is found that the premature ionization near the sidewall is merged with the degree of ionization boundary-layer thickness.

Further investigation based on the time-dependent Navier-Stokes equation may be required in order to predict the two-dimensional effects on shock-wave structure and the unsteady effects on induced flat-plate boundary-layer flows.

REFERENCES

1. Glass, I. I.; Liu, W. S.; Tang, F. C. "Effect of Hydrogen Impurities on Shock Structure and Stability in Ionizing Monatomic Gases: II. Krypton", Can. J. Phys. 56, 1269 (1977).

2. Glass, I. I.; Liu, W. S. "Effects of Hydrogen Impurity on Shock Structure and Stability in Ionizing Monatomic Gases, Part 1. Argon", J. Fluid Mech. 84, 55 (1978).

3. Liu, W. S.; Whitten, B. T.; Glass, I. I. "Ionizing Argon Boundary Layer, Part 1. Quasi-Steady Flat-Plate Laminar Boundary Layer Flows", J. Fluid Mech. 87, 609 (1978).

4. Liu, W. S.; Glass, I. I. "Ionizing Argon Boundary Layer, Part 2. Shock-Tube Sidewall Boundary-Layer Flows", J. Fluid Mech. (in press) (1979).

5. Glass, I. I.; Patterson, G. N. "A Theoretical and Experimental Study of Shock Tube Flows", J. Aeronaut. Sci. 22, 73 (1955).

6. Mirels, H. "Flow Nonuniformity in Shock Tube Operating at Maximum Test Times", Phys. Fluids 9, 1907 (1966).

7. Mirels, H "Shock Tube Test Time Limitation Due to Turbulent Wall Boundary Layer", AIAA J. 2, 84 (1964).

8. Mirels, H. "Test Time in Low Pressure Shock Tubes", Phys. Fluids 6, 1201 (1963)

9. Enomoto, Y. "Wall Boundary Layer Effects on Ionizing Shock Structure in Argon", J. Phys. Soc. Japan 35, 1228 (1973).

10. McLaren, T. I.; Hobson, R. M. "Initial Ionization Rates and Collision Cross Sections in Shock Heated Argon", Phys. Fluids 9, 2162 (1968).

11. Brabbs, T. A.; Belles, F. E. "Experimental Study of Effects of Laminar Boundary Layers on Chemical-Kinetic Measurements in a Shock Tube", Proc. 8th International Shock Tube Symposium, London (1971).

12. Trimpi, R. L.; Cohen, N. B. "A Theory for Predicting the Flow of Real Gases in Shock Tubes with Experimental Verification", NACA TN 3375 (1955).

13. Hubbard, E. W.; de Boer, P. C. T. "Flow Field Behind a Shock Wave in a Low Pressure Test Gas", Proc. 7th International Shock Tube Symposium, Toronto (1969).

14. Demmig, F. "Ionization Relaxation in Shock Tubes Under the Influence of a Weakly Unsteady Shock Front and Wall Boundary Layer Effect", Proc. 11th International Shock Tube Symposium, Seattle (1977).

15. Dem'yanov, Yu. A. "The Influence of the Boundary Layer on the Character of the Flow of Gas in a Tube Behind a Moving Shock Wave", Library Translation No. 796 (1959).

16. Appleton, J P.
Bray, K. N. C. "The Conservation Equations for a Nonequilibrium Plasma", J. Fluid Mech. 20, 659 (1964).

17. Belles, F. E.
Brabbs, T. A. "Experimental Verification of Effects of Turbulent Boundary Layers on Chemical Kinetic Measurements in a Shock Tube", NASA TM X-52761 (1970).

18. Schlichting, H. Boundary Layer Theory, McGraw-Hill, New York (1966).

19. Glass, I. I.
Liu, W. S.
Tang, F. C. "Radiation-Induced Shock Tube Flow Nonuniformities in Ionizing Argon", Submitted to Phys. Fluids (1979).

20. Deckker, B. E. L.
Weekes, M. E. "Development of Velocity and Temperature of the Flow Behind a Moving Shock Wave in a Duct", Proc. Inst. Mech. Engrs. 190, 287 (1976).

Table 1(a)

Quasi-equilibrium peak values of α, n_e and ρ and relaxation lengths.

The first iteration results at M_s = 13.1, p_o = 5.16 torr and T_o = 300 K.

M_s = 13.1					
	D cm	x_E cm	α_E	n_{eE} $x10^{17}/cm^3$	ρ_E $x10^{-4}g/cm^3$
First order	∞	10.00	0.0590	0.566	0.650
Non-equilibrium **	6.43	6.63	0.0711	0.771	0.719
	12.86	7.93	0.0639	0.655	0.680
		8.93	0.0579	0.576	0.660 *
	25.71	8.88	0.0596	0.594	0.661
Frozen***	6.43	7.88	0.0676	0.694	0.681
	12.86	8.98	0.0612	0.609	0.660
	25.71	9.48	0.0589	0.578	0.650

* Results by higher iteration number
** Nonequilibrium boundary-layer profile
*** Frozen boundary-layer profile

Table 1(b)

Quasi-equilibrium peak values of α, n_e and ρ and relaxation lengths.

The first iteration results at $M_s = 15.9$, $p_o = 5.10$ torr and $T_o = 297$ K.

$M_s = 15.9$					
	D cm	x_E cm	α_E	n_{e_E} $\times 10^{18}/cm^3$	ρ_E $\times 10^{-4} g/cm^3$
First order	∞	2.15	0.1361	0.168	0.821
Non-equilibrium **	6.43	1.83	0.1414	0.182	0.852
	12.86	2.03	0.1363	0.170	0.828
		2.03	0.1359	0.170	0.830 *
	25.71	2.12	0.1355	0.168	0.824
Frozen***	6.43	1.93	0.1424	0.182	0.848
	12.86	2.03	0.1371	0.173	0.825
	25.71	2.13	0.1362	0.170	0.823

* Results by higher iteration number
** Nonequilibrium boundary-layer profile
*** Frozen boundary-layer profile

Table 2

Initial conditions and freestream conditions for flat-plate boundary-layer flow.

Comparison of present conditions with those in Ref. 3.

M_s	16.6		12.8	
p_o (torr)	4.81		5.01	
T_o (°K)	296		297	
	Ref. 3	Present	Ref. 3	Present
u_δ (cm/s)	4.86×10^5	4.97×10^5	3.53×10^5	3.59×10^5
p_δ (torr)	2025	2160	1200	1189
$T_{a\delta}$ (°K)	1.049×10^4	1.043×10^4	1.065×10^4	1.043×10^4
α_δ	0.021	0.020	0.031	0.028
$n_{e\delta}$ (cm^{-3})	3.75×10^{16}	3.87×10^{16}	3.27×10^{16}	2.97×10^{16}
M_δ	2.9	3.0	2.1	2.2
a_δ (cm/s)	1.681×10^5	1.673×10^5	1.676×10^5	1.650×10^5
x_m (cm)	14	14	14	14
x_s (cm)	46	46	46	46
x_E (cm)	1.7	1.57	13.0	11.0

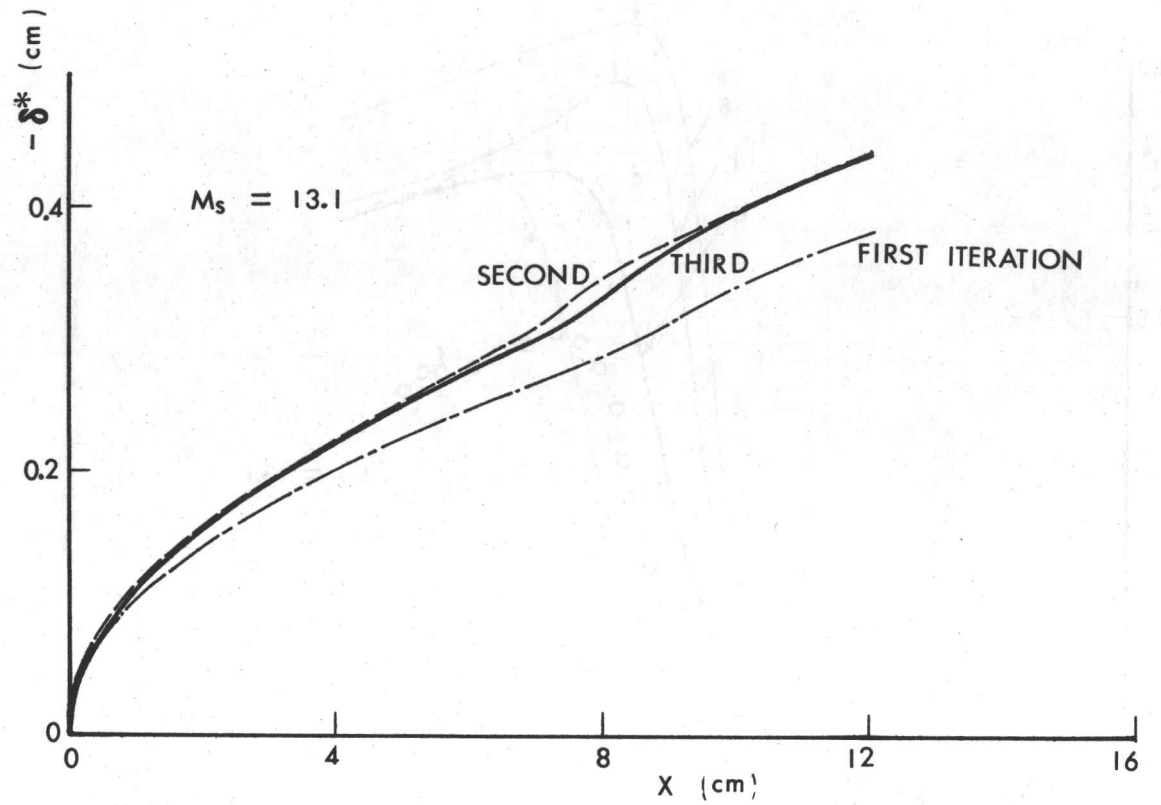

FIG. 1(a) COMPARISON OF BOUNDARY-LAYER DISPLACEMENT-THICKNESS GROWTHS FOR THREE ITERATIONS FOR M_s = 13.1, p_o = 5.16 TORR AND T_o = 300 K.

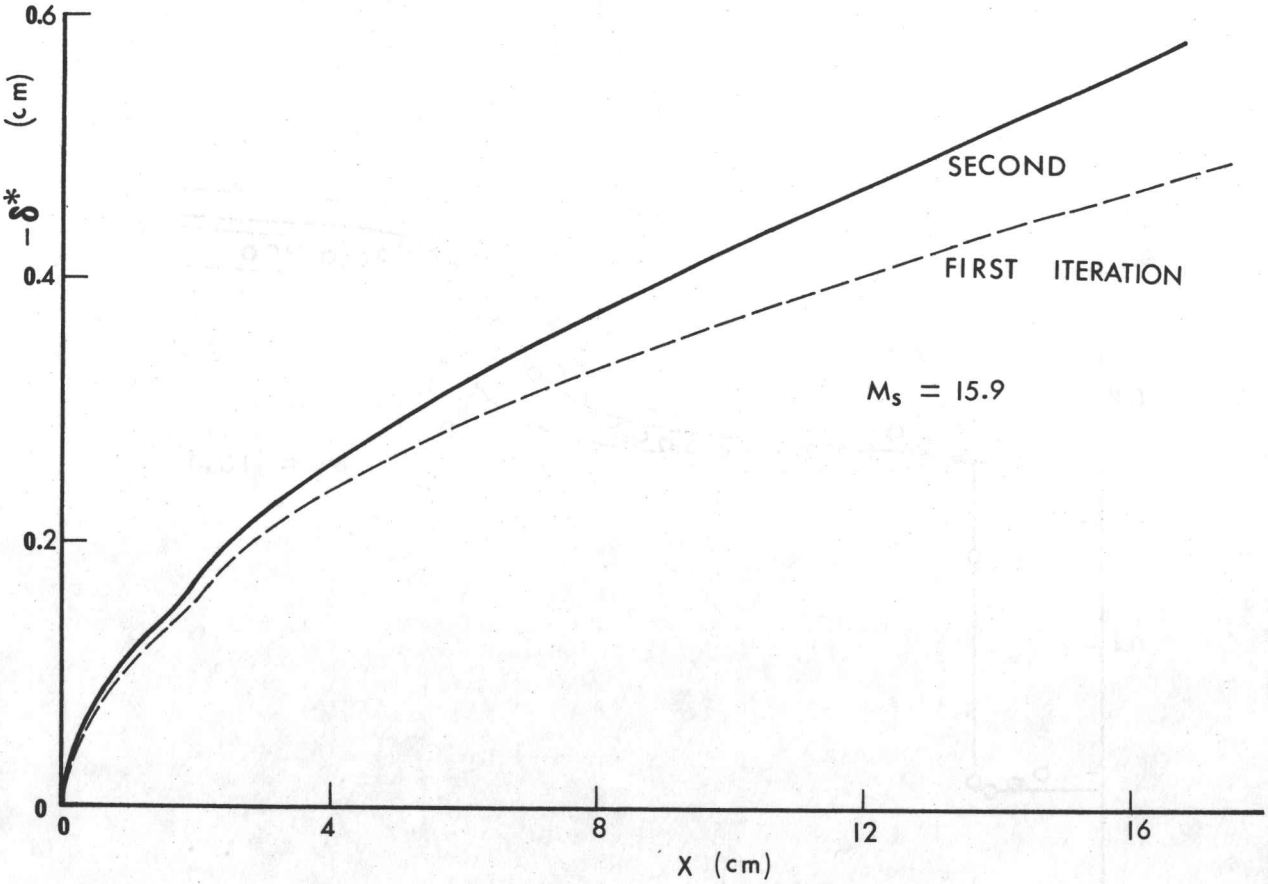

FIG. 1(b) COMPARISON BOUNDARY-LAYER DISPLACEMENT-THICKNESS GROWTHS FOR TWO ITERATIONS FOR M_s = 15.9, p_o = 5.10 TORR AND T_o = 298 K.

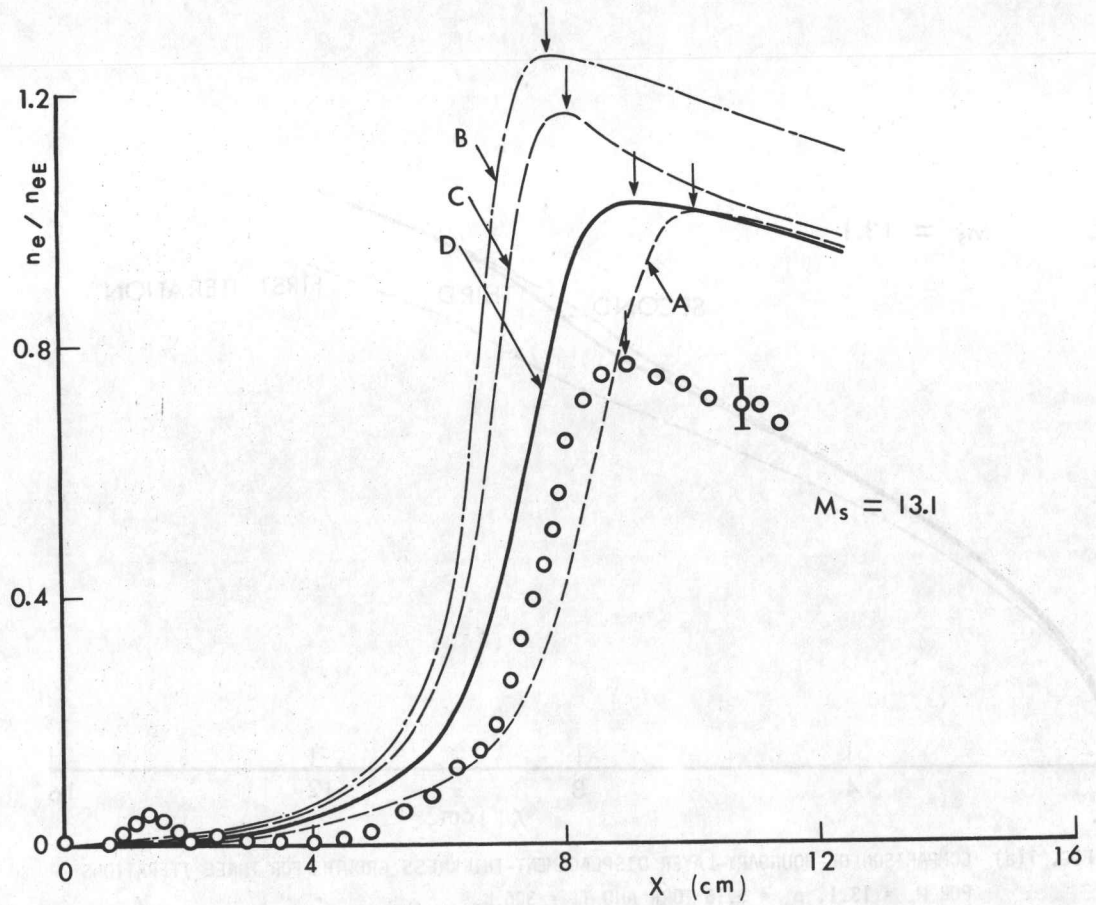

FIG. 2 VARIATIONS OF NORMALIZED ELECTRON-NUMBER DENSITY n_e/n_{eE} WITH DISTANCE X FOR M_s = 13.1, p_o = 5.16 TORR AND T_o = 300 K. SUBSCRIPT E DENOTES QUASI-EQUILIBRIUM VALUE. CURVE A: FIRST-ORDER RESULTS WITHOUT MUTUAL INTERACTIONS; CURVE B: ENOMOTO'S MODEL; CURVE C: FIRST-ITERATIVE RESULT; CURVE D: FINAL ITERATIVE RESULT. ARROWS SHOW TERMINATION OF RELAXATION.

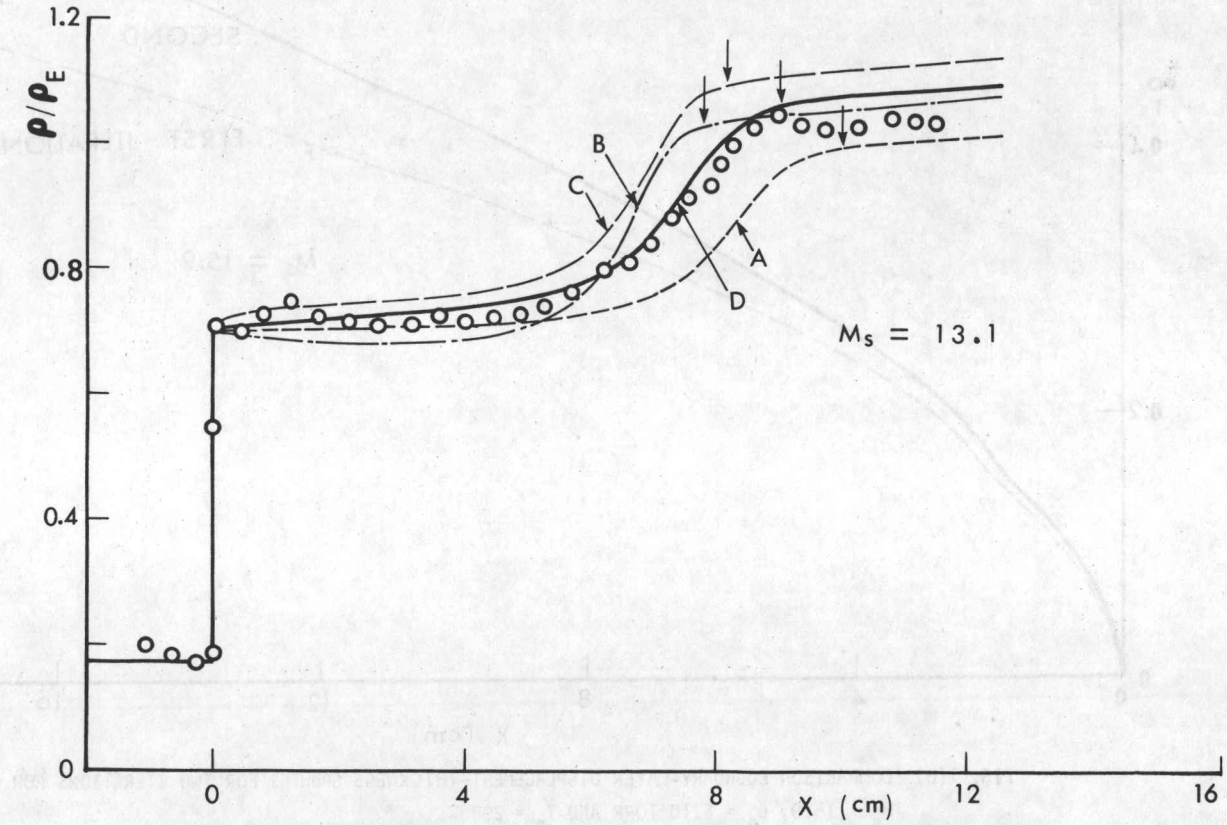

FIG. 3 VARIATIONS OF NORMALIZED TOTAL-PLASMA-DENSITY PROFILES ρ/ρ_E WITH DISTANCE X FOR M_s = 13.1, p_o = 5.16 TORR AND T_o = 300 K. (FOR OTHER NOTATIONS, SEE FIG. 2.)

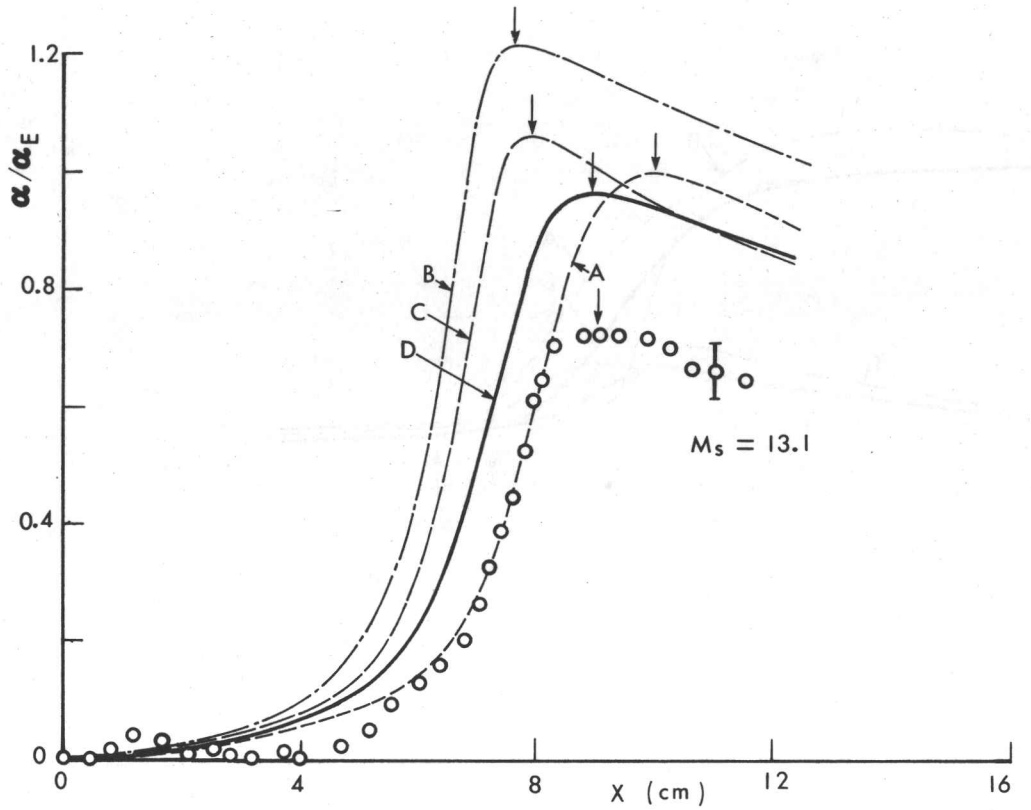

FIG. 4 VARIATIONS OF NORMALIZED DEGREE OF IONIZATION PROFILES α/α_E WITH DISTANCE X FOR M_s = 13.1, p_o = 5.16 TORR AND T_o = 300 K. (FOR OTHER NOTATIONS, SEE FIG. 2.)

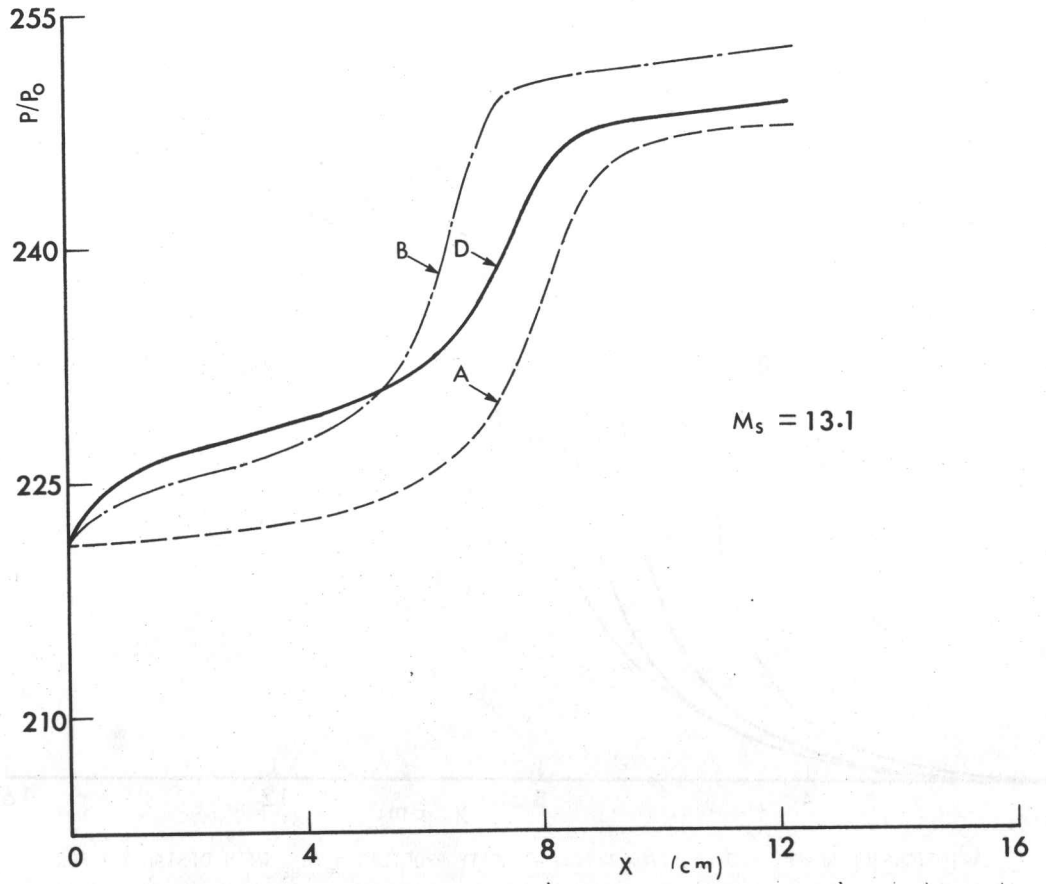

FIG. 5 VARIATIONS OF NORMALIZED PRESSURE P/P_o WITH DISTANCE X FOR M_s = 13.1, p_o = 5.16 TORR AND T_o = 300 K. CURVE A: FIRST-ORDER RESULTS WITHOUT MUTUAL INTERACTIONS; CURVE B: ENOMOTO'S MODEL; CURVE D: FINAL ITERATIVE RESULTS OF PRESENT MODEL.

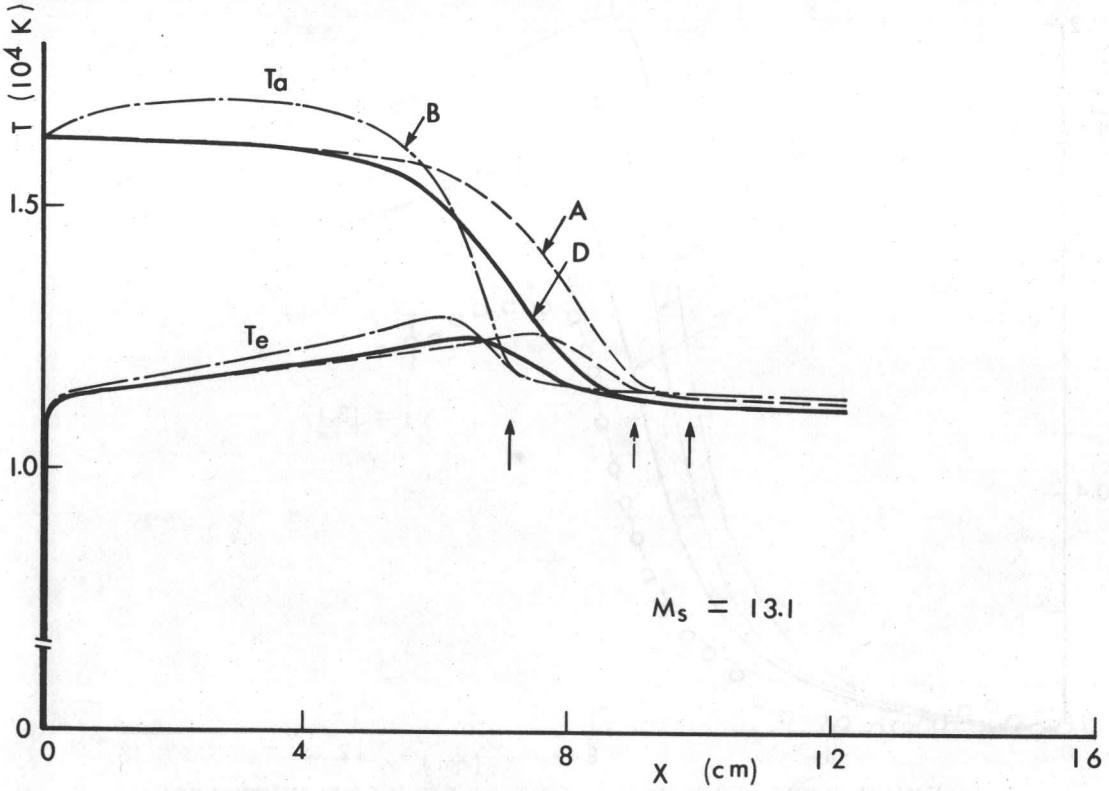

FIG. 6 VARIATIONS OF ATOM TEMPERATURE T_a AND ELECTRON TEMPERATURE T_e WITH DISTANCE X FOR M_s = 13.1, p_o = 5.16 TORR AND T_o = 300 K. (FOR OTHER NOTATIONS, SEE FIG. 5.)

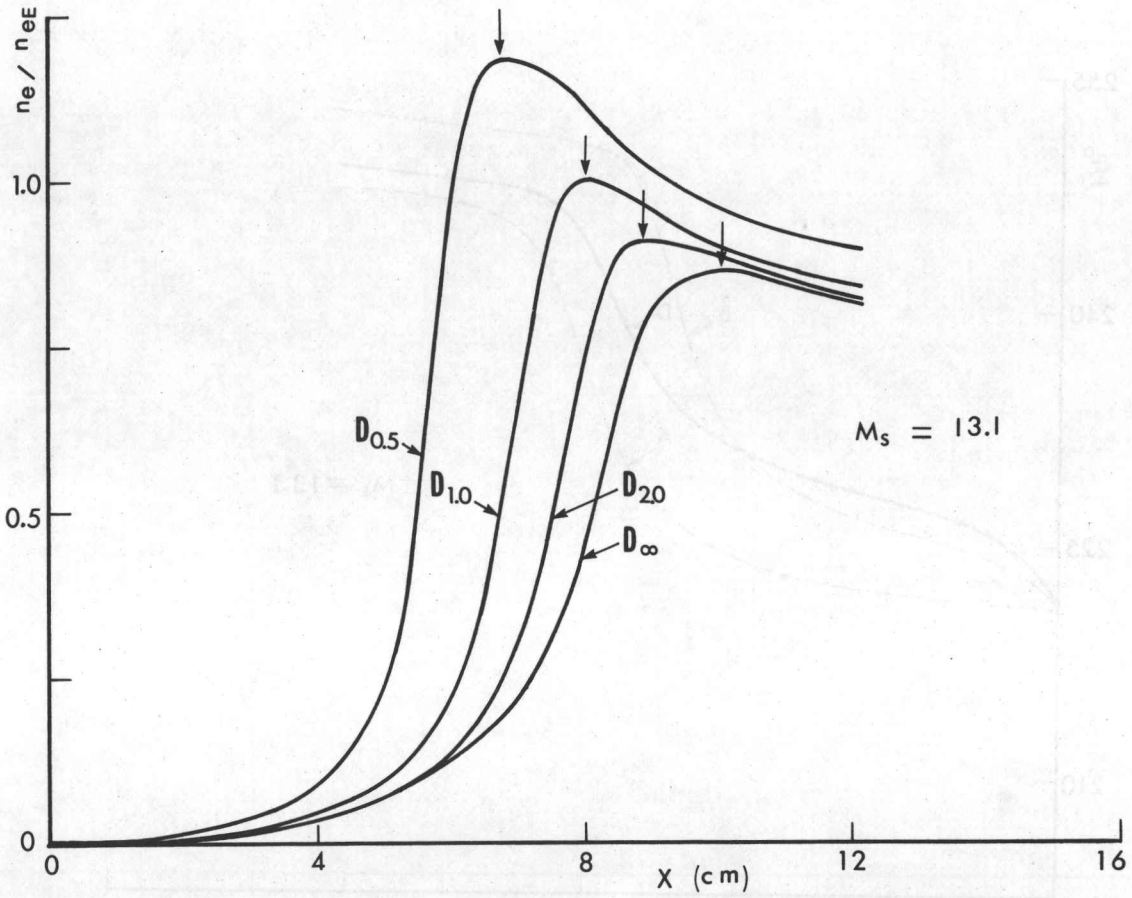

FIG. 7 VARIATIONS OF NORMALIZED ELECTRON-NUMBER-DENSITY PROFILES n_e/n_{eE} WITH DISTANCE X FOR VARIOUS SHOCK-TUBE HYDRAULIC-DIAMETERS D FOR M_s = 13.1, p_o = 5.16 TORR AND T_o = 300 K. CURVE $D_{0.5}$: D = 6.43 CM; CURVE $D_{1.0}$: D = 12.86 CM EQUIVALENT TO UTIAS 10 CM x 18 CM HYPERVELOCITY SHOCK TUBE; CURVE $D_{2.0}$: D = 25.72 CM; AND CURVE D_∞: D = ∞ CM.

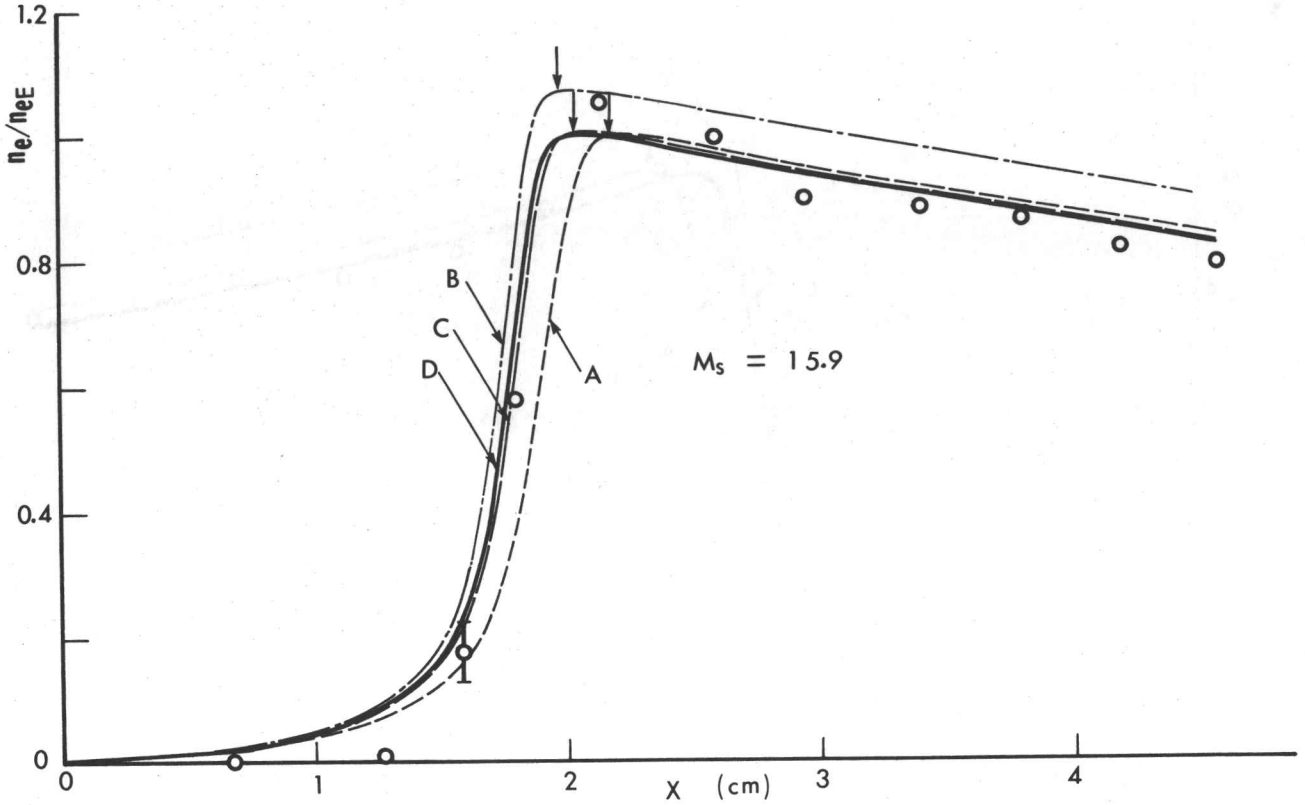

FIG. 8 VARIATIONS OF NORMALIZED ELECTRON-NUMBER-DENSITY PROFILES n_e/n_{eE} WITH DISTANCE X FOR M_s = 15.9, p_o = 5.1 TORR AND T_o = 298 K. (FOR OTHER NOTATIONS, SEE FIG. 2.)

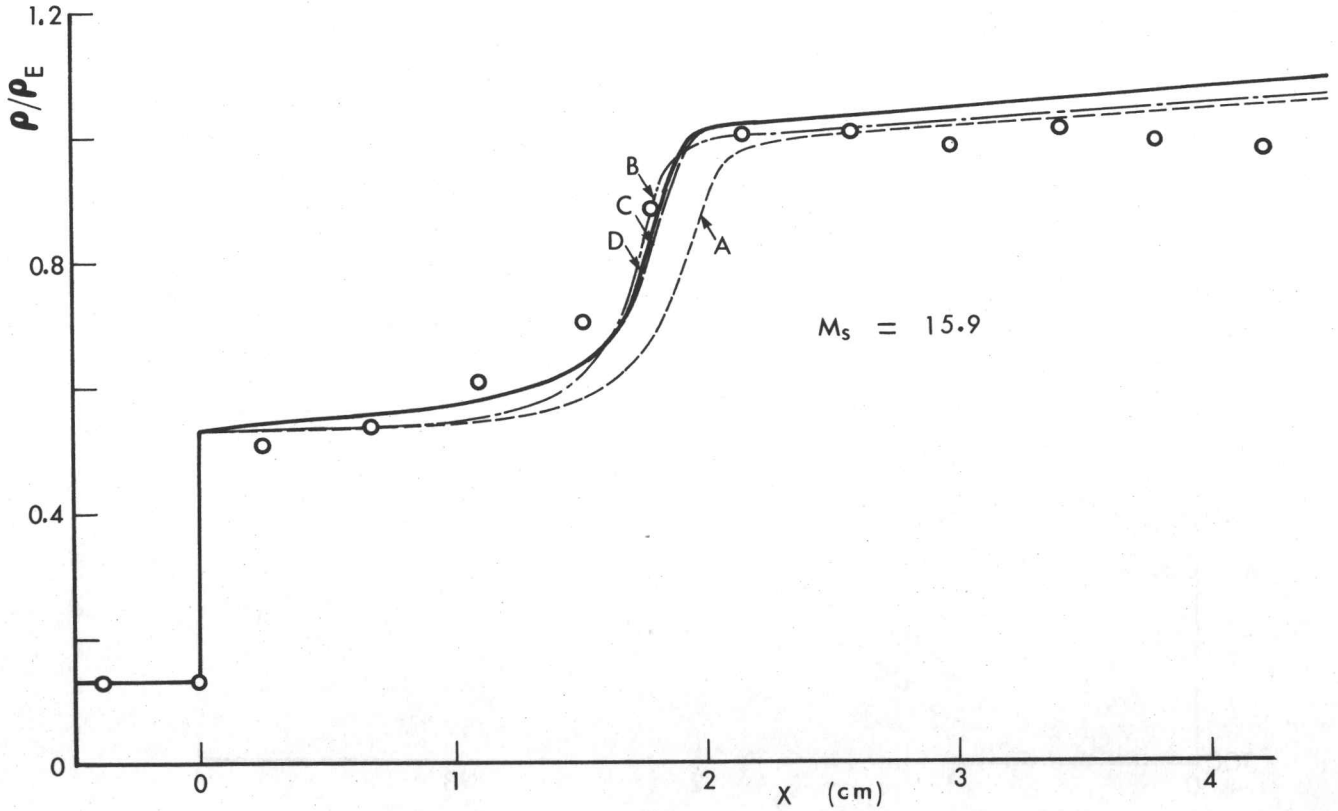

FIG. 9 VARIATIONS OF NORMALIZED TOTAL-PLASMA-DENSITY PROFILES ρ/ρ_E WITH DISTANCE X FOR M_s = 15.9, p_o = 5.1 TORR AND T_o = 298 K. (FOR OTHER NOTATIONS, SEE FIG. 2.)

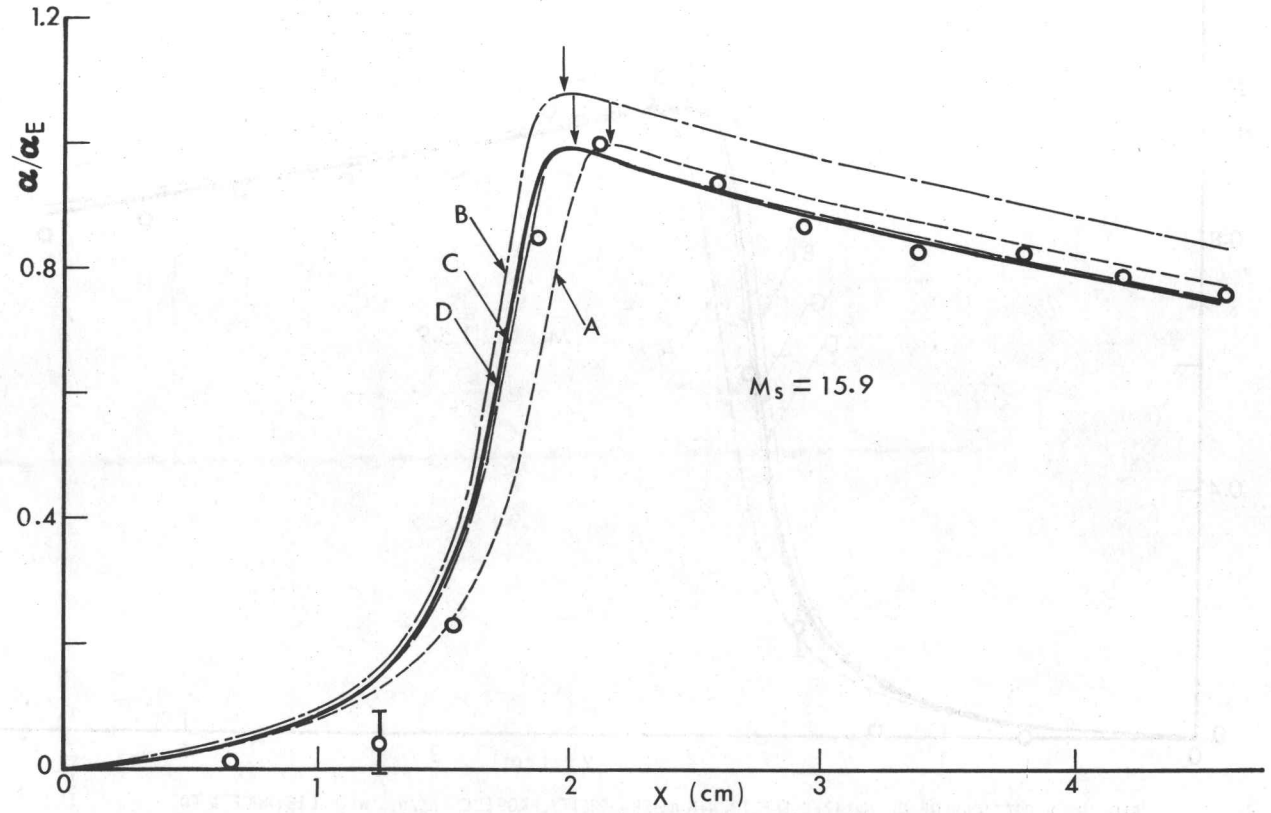

FIG. 10 VARIATIONS OF NORMALIZED DEGREE OF IONIZATION PROFILES α/α_E WITH DISTANCE X FOR M_s = 15.9, p_o = 5.1 TORR AND T_o = 298 K. (FOR OTHER NOTATIONS, SEE FIG. 2.)

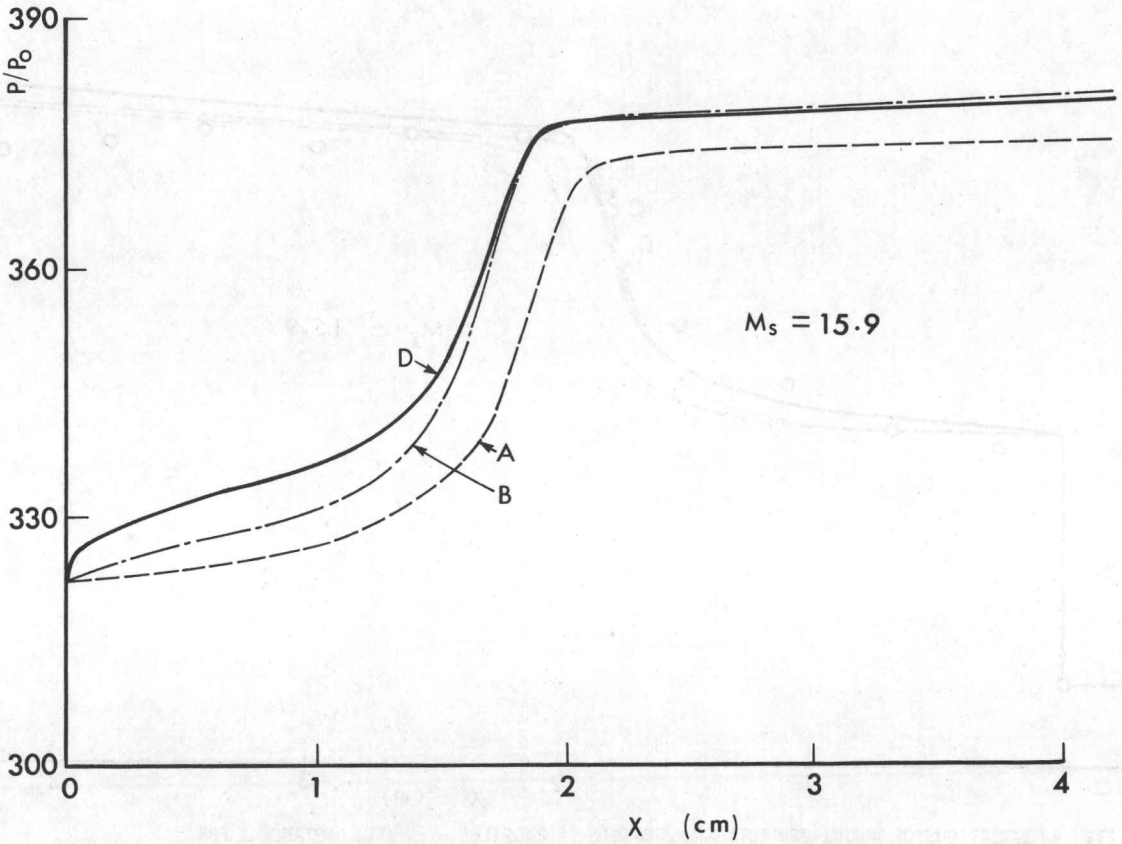

FIG. 11 VARIATIONS OF NORMALIZED PRESSURE P/P_o WITH DISTANCE X FOR M_s = 15.9, p_o = 5.10 TORR AND T_o = 298 K. (FOR OTHER NOTATIONS, SEE FIG. 5.)

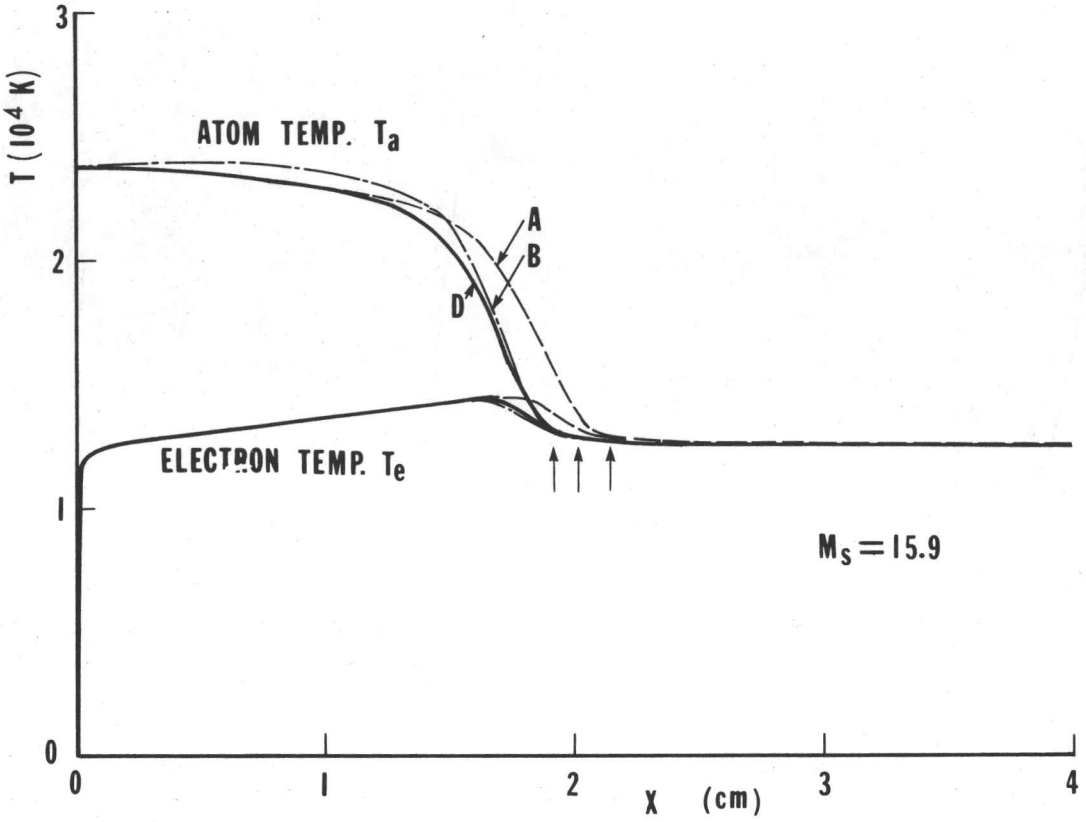

FIG. 12 VARIATIONS OF ATOM TEMPERATURE T_a AND ELECTRON TEMPERATURE T_e WITH DISTANCE X FOR M_s = 15.9, p_o = 5.10 TORR AND T_o = 300 K. (FOR OTHER NOTATIONS, SEE FIG. 6.)

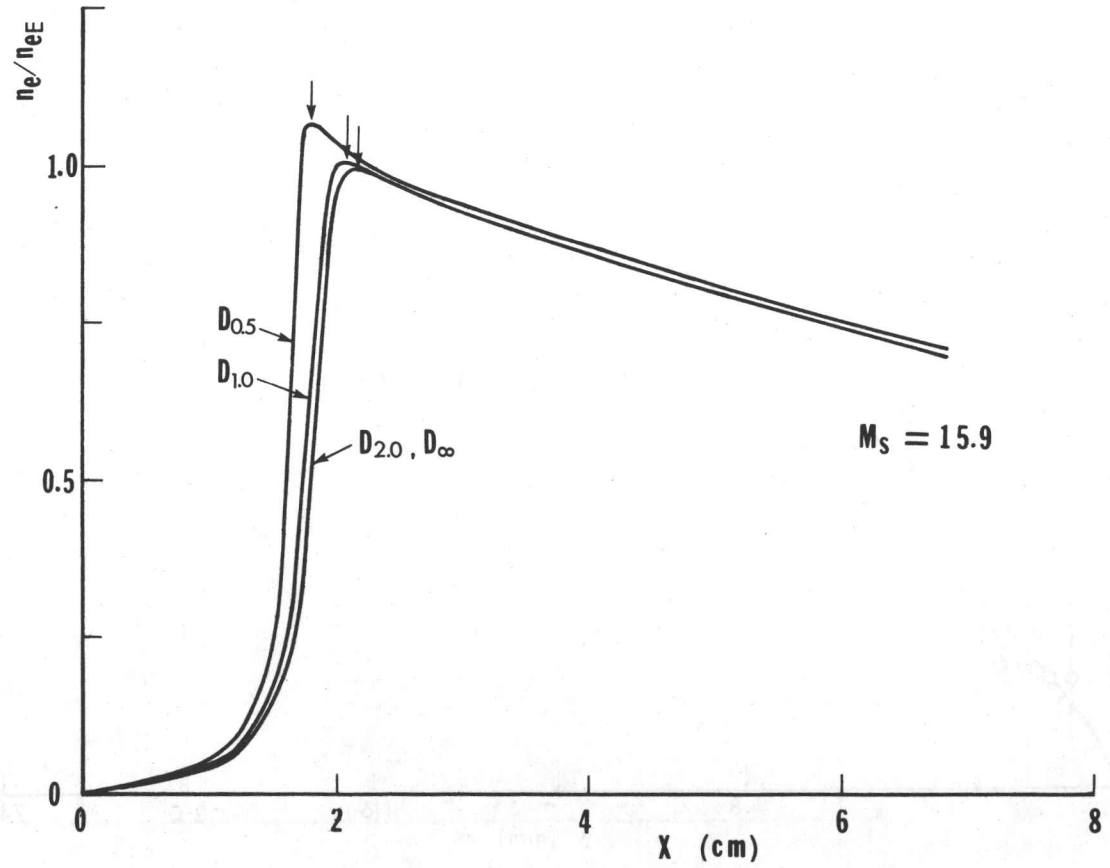

FIG. 13 VARIATIONS OF NORMALIZED ELECTRON-NUMBER-DENSITY PROFILES n_e/n_{eE} WITH DISTANCE X FOR VARIOUS SHOCK-TUBE HYDRAULIC-DIAMETER D FOR CASE WITH M_s = 15.9, p_o = 5.1 TORR AND T_o = 298 K. (FOR OTHER NOTATIONS, SEE FIG. 7.)

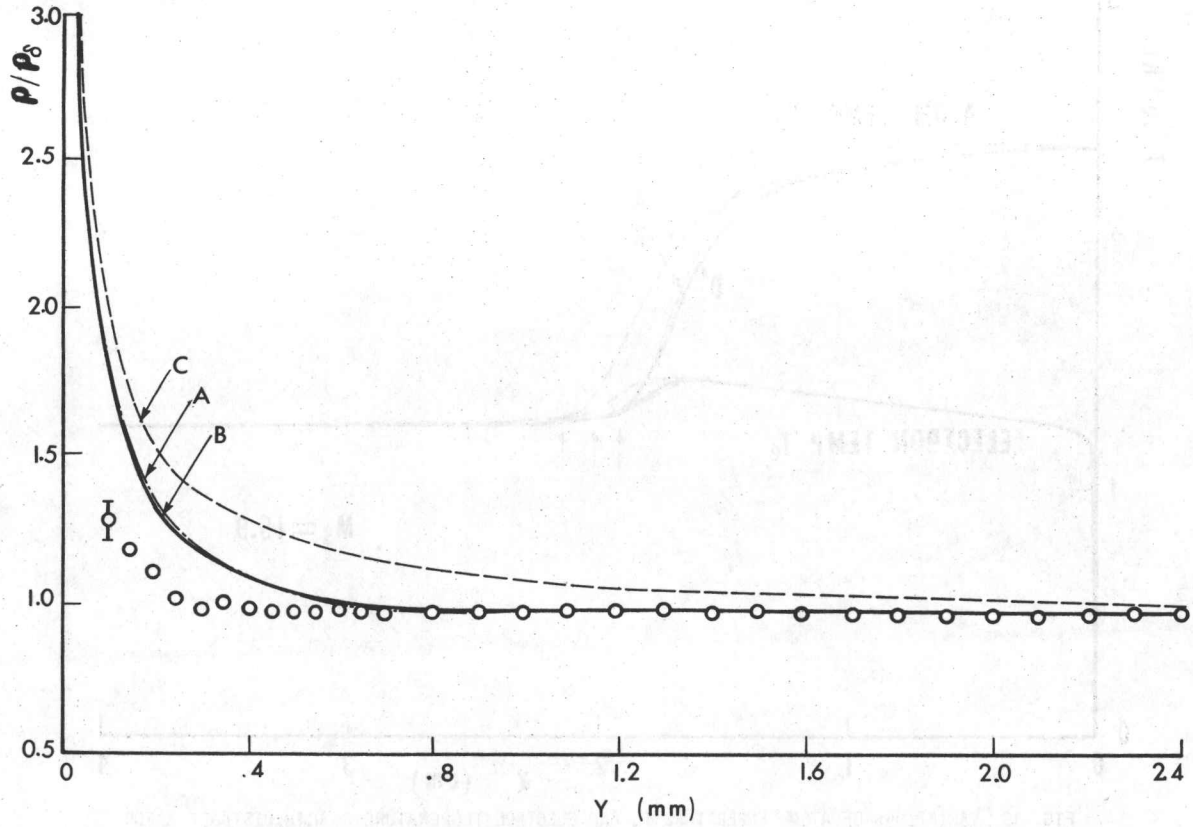

FIG. 14 COMPARISON OF ANALYTICAL AND EXPERIMENTAL NORMALIZED PROFILES OF PLASMA DENSITY ρ/ρ_δ WITH DISTANCE Y IN THE SIDEWALL BOUNDARY LAYER IN ARGON AT X = 9.5 CM, M_s = 13.1, p_0 = 5.16 TORR AND T_0 = 300 K. CURVE A: FIRST-ORDER RESULT; CURVE B: PRESENT RESULT; CURVE C: FROZEN SOLUTION.

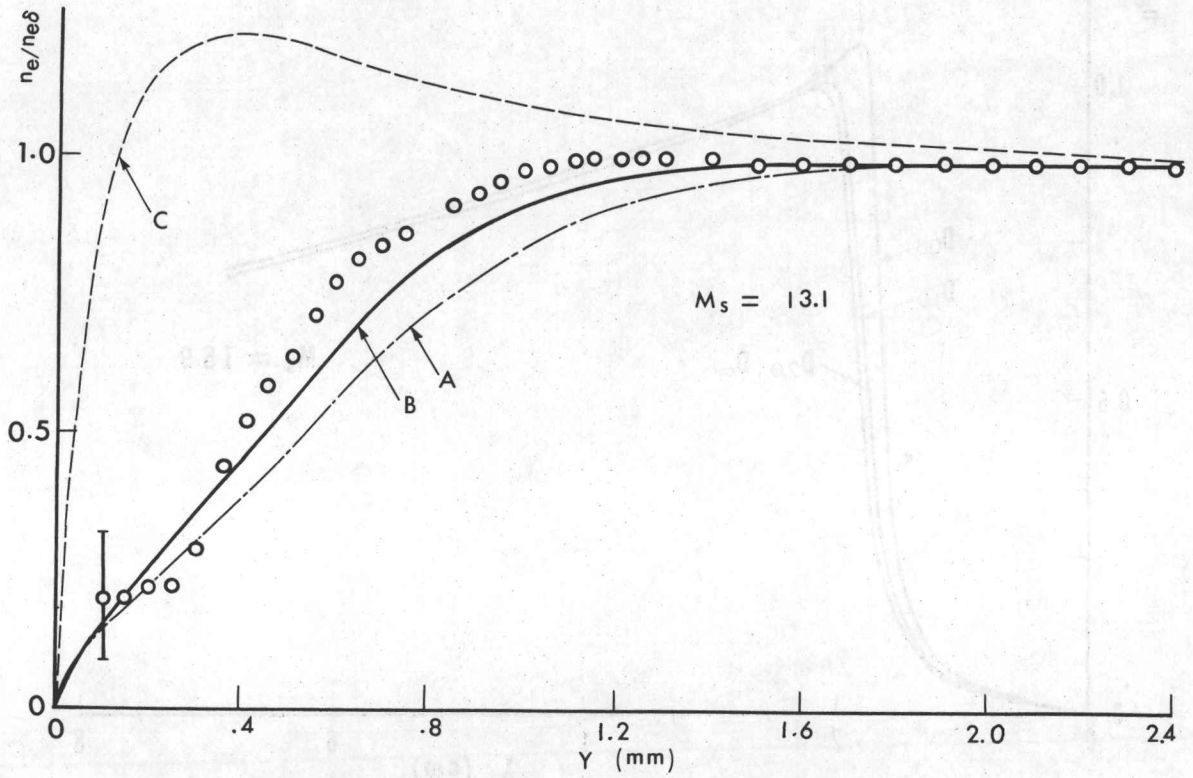

FIG. 15 COMPARISON OF ANALYTICAL AND EXPERIMENTAL NORMALIZED ELECTRON-NUMBER-DENSITY PROFILES $n_e/n_{e\delta}$ WITH DISTANCE Y IN THE SIDEWALL BOUNDARY LAYER IN ARGON AT X = 9.5 CM, M_s = 13.1, p_0 = 5.16 TORR AND T_0 = 300 K. (FOR OTHER NOTATIONS, SEE FIG. 14.)

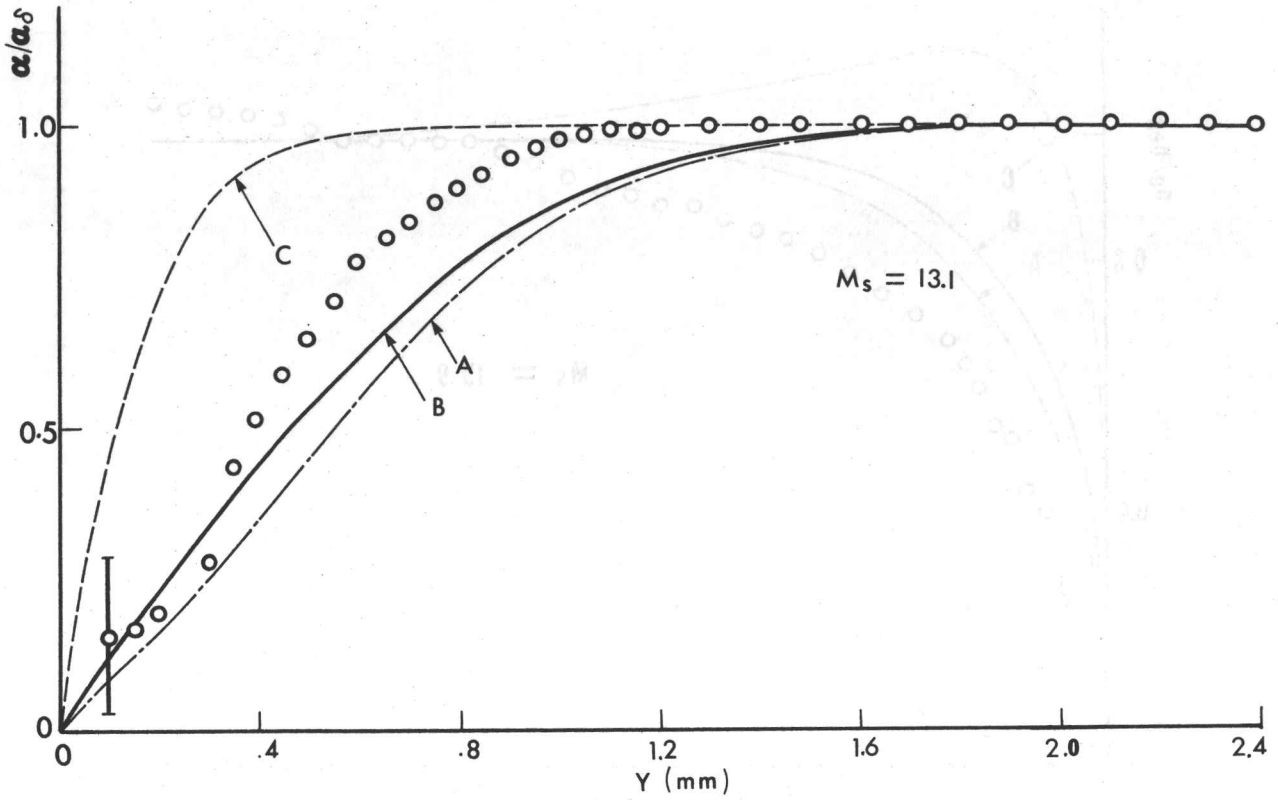

FIG. 16 COMPARISON OF ANALYTICAL AND EXPERIMENTAL NORMALIZED PROFILES OF DEGREE OF IONIZATION α/α_δ WITH DISTANCE Y IN THE SIDEWALL BOUNDARY LAYER AT X = 9.5 CM, M_s = 13.1, p_o = 5.16 TORR AND T_o = 300 K. (FOR OTHER NOTATIONS, SEE FIG. 14.)

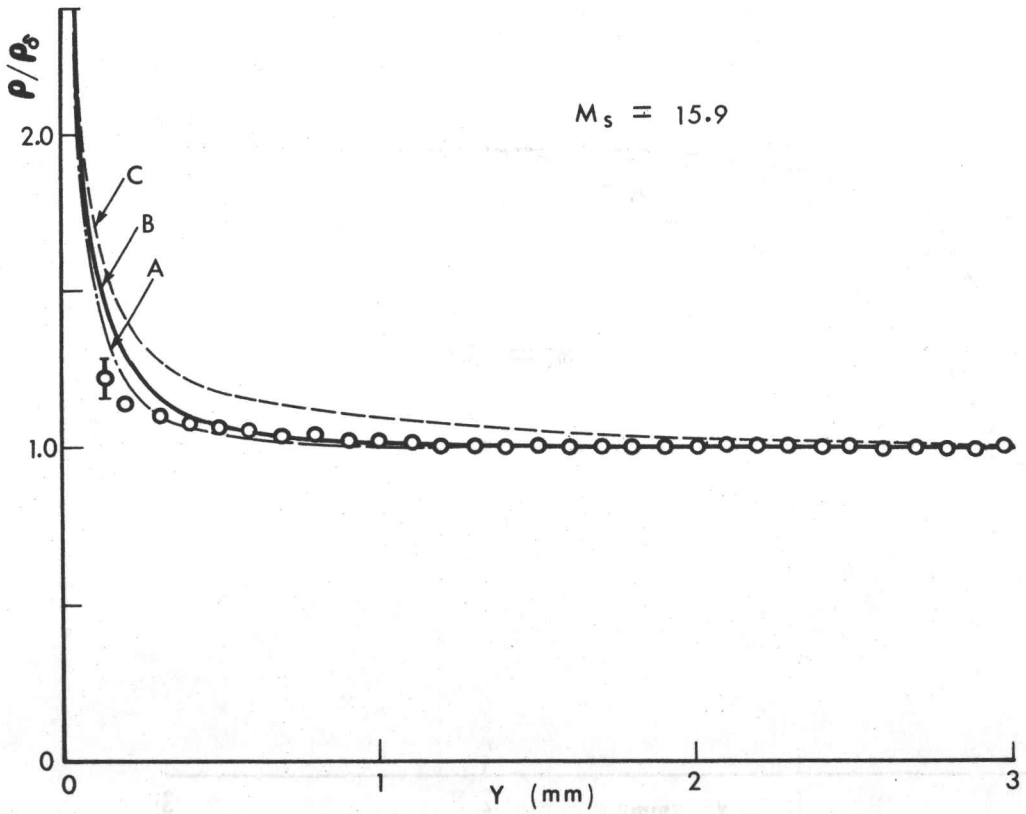

FIG. 17 COMPARISON OF ANALYTICAL AND EXPERIMENTAL NORMALIZED PROFILE OF PLASMA DENSITY ρ/ρ_δ WITH DISTANCE Y IN THE SIDEWALL BOUNDARY LAYER AT X = 18 CM, M_s = 15.9, p_o = 5.10 TORR AND T_o = 298 K. (FOR OTHER NOTATIONS, SEE FIG. 14.)

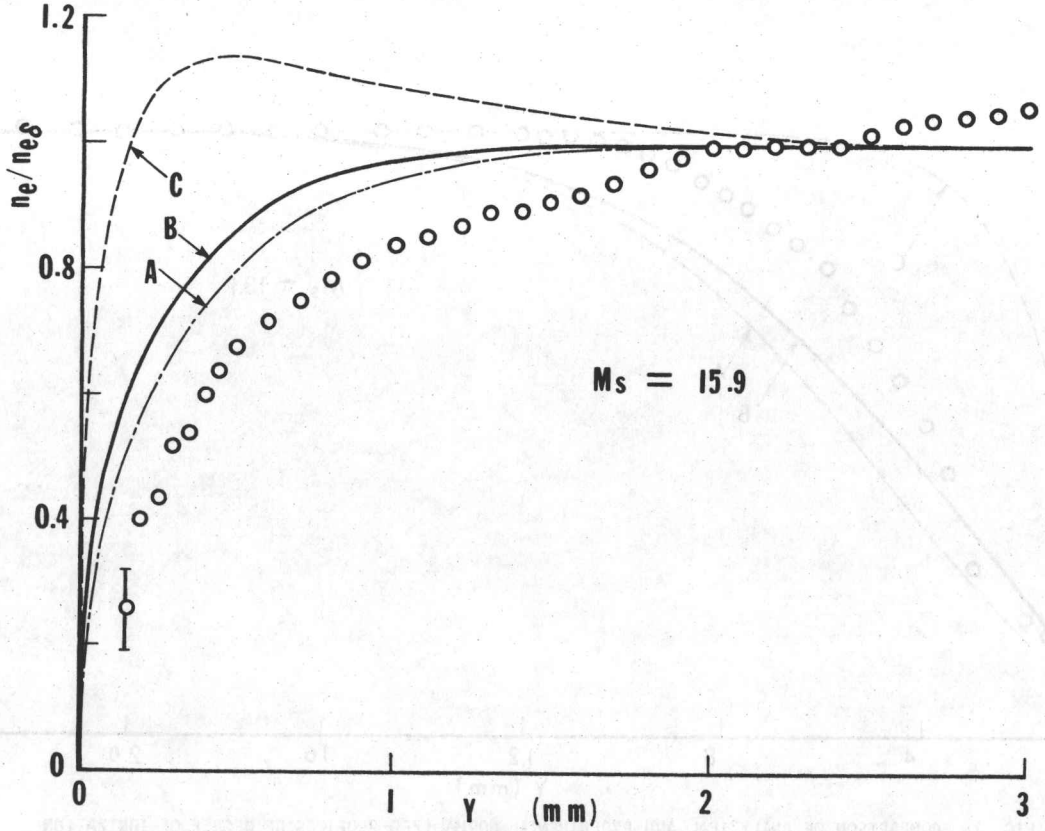

FIG. 18 COMPARISON OF ANALYTICAL AND EXPERIMENTAL NORMALIZED PROFILES OF ELECTRON NUMBER DENSITY $n_e/n_{e\delta}$ WITH DISTANCE Y IN THE SIDEWALL BOUNDARY LAYER AT X = 18 CM, M_s = 15.9, p_o = 5.1 TORR AND T_o = 298 K. (FOR OTHER NOTATIONS, SEE FIG. 14.)

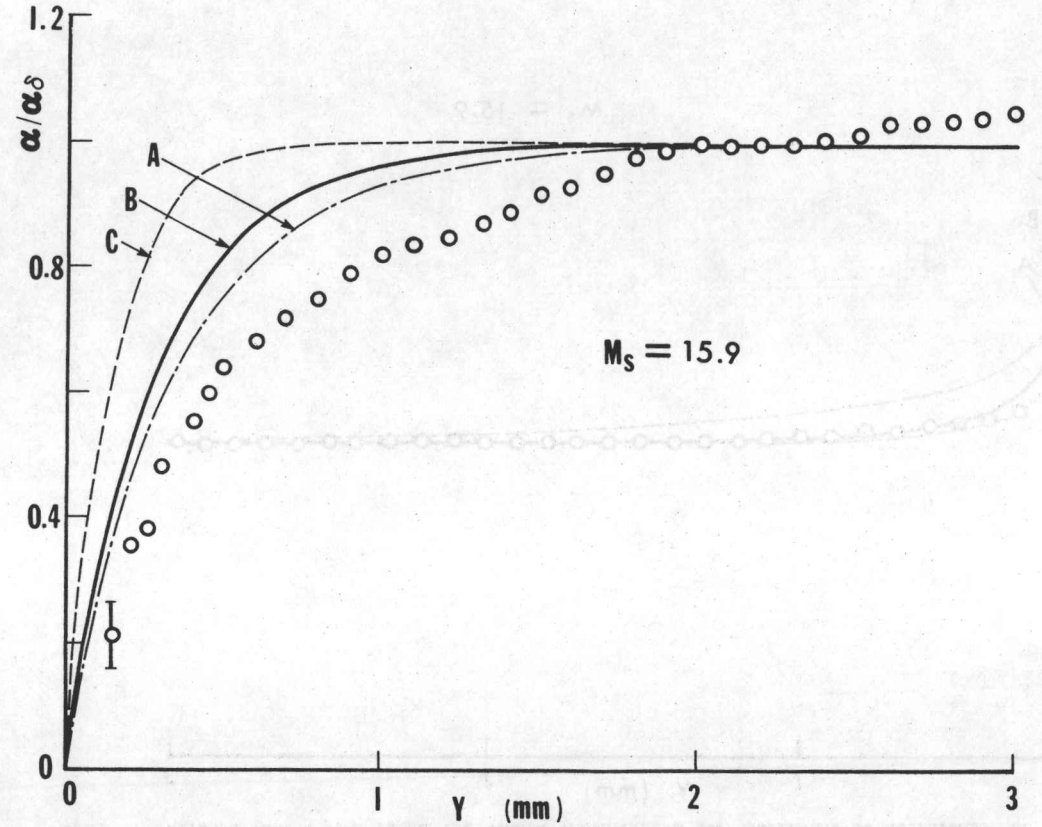

FIG. 19 COMPARISON OF ANALYTICAL AND EXPERIMENTAL NORMALIZED PROFILES OF DEGREE OF IONIZATION α/α_δ WITH DISTANCE Y IN THE SIDEWALL BOUNDARY LAYER AT X = 18 CM, M_s = 15.9, p_o = 5.1 TORR AND T_o = 298 K. (FOR OTHER NOTATIONS, SEE FIG. 14.)

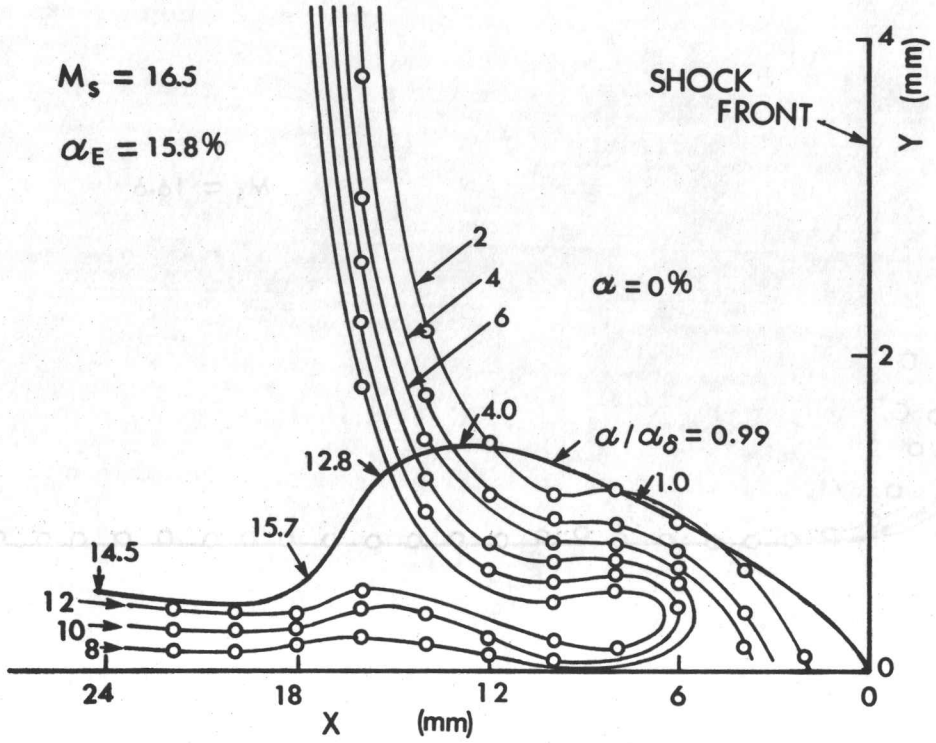

FIG. 20(a) CONTOURS OF CONSTANT DEGREE OF IONIZATION IN RELAXATION REGION CLOSE TO WALL IN ARGON AT M_s = 16.5, p_0 = 5.12 TORR AND T_0 = 297 K (SEE REF. 2). SOLID LINE: CONTOUR OF DEGREE OF IONIZATION BOUNDARY LAYER α/α_δ = 0.99 AT M_s = 16.6, p_0 = 4.81 TORR AND T_0 = 298 K.

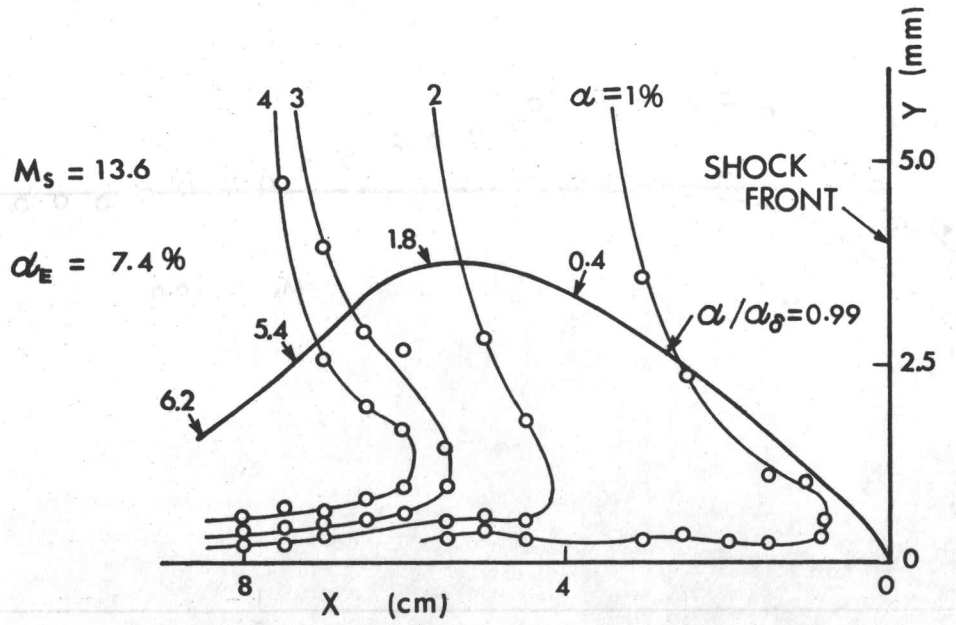

FIG. 20(b) CONTOURS OF CONSTANT DEGREE OF IONIZATION IN RELAXATION REGION CLOSE TO WALL IN ARGON AT M_s = 13.6, p_0 = 5.09 AND T_0 = 296.7 K (SEE REF. 2). SOLID LINE: CONTOUR OF DEGREE OF IONIZATION BOUNDARY LAYER α/α_δ AT M_s = 13.1, p_0 = 5.16 TORR AND T_0 = 300 K.

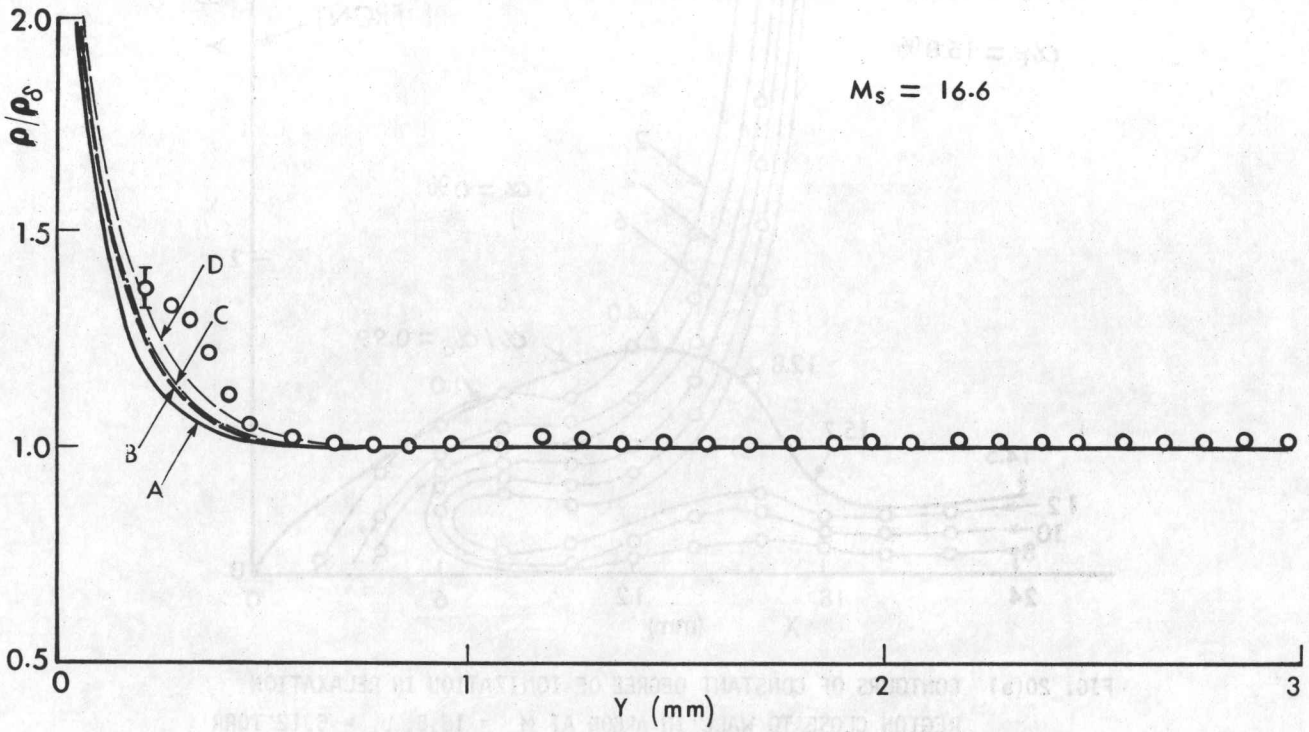

FIG. 21 COMPARISON OF ANALYTICAL AND EXPERIMENTAL NORMALIZED PROFILES OF PLASMA DENSITY ρ/ρ_δ WITH DISTANCE Y FOR FLAT-PLATE BOUNDARY LAYER AT X = 14 CM, M_s = 16.6, p_o = 4.81 TORR AND T_o = 296 K. CURVE A: PRESENT NONEQUILIBRIUM; CURVE B: PRESENT FROZEN; CURVE C: FIRST-ORDER NONEQUILIBRIUM; CURVE D: FIRST-ORDER FROZEN.

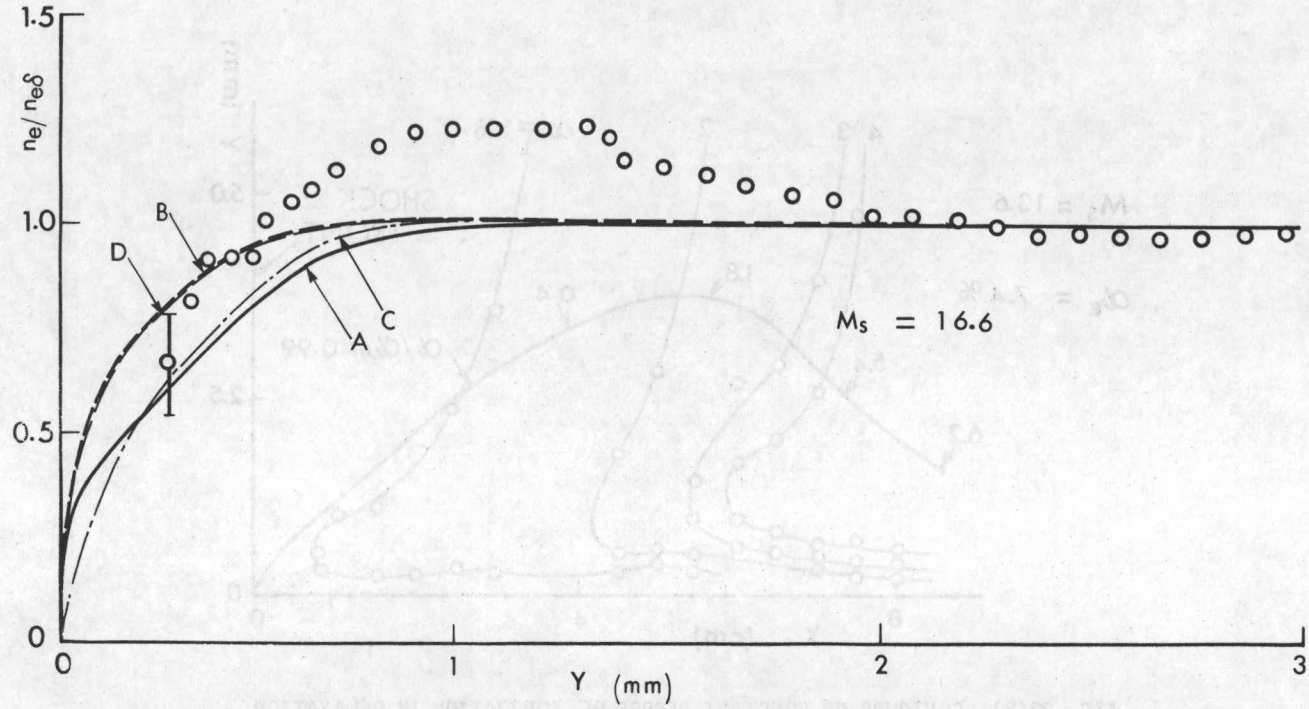

FIG. 22 COMPARISON OF ANALYTICAL AND EXPERIMENTAL NORMALIZED ELECTRON-NUMBER-DENSITY PROFILE $n_e/n_{e\delta}$ WITH DISTANCE Y FOR FLAT-PLATE BOUNDARY LAYER. (INITIAL CONDITIONS AND NOTATIONS ARE GIVEN IN FIG. 21.)

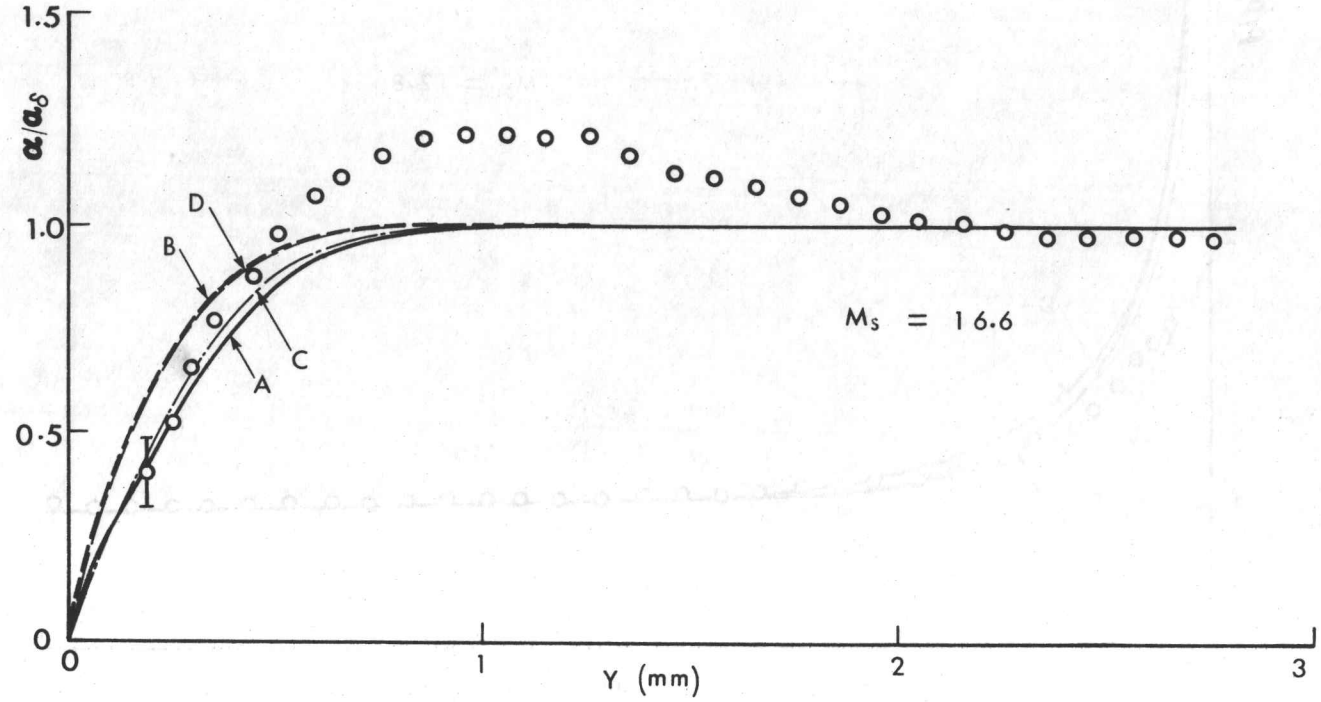

FIG. 23 COMPARISON OF ANALYTICAL AND EXPERIMENTAL NORMALIZED PROFILE FOR DEGREE OF IONIZATION α/α_δ WITH DISTANCE Y FOR FLAT-PLATE BOUNDARY LAYER. (FOR OTHER NOTATIONS, SEE FIG. 21.)

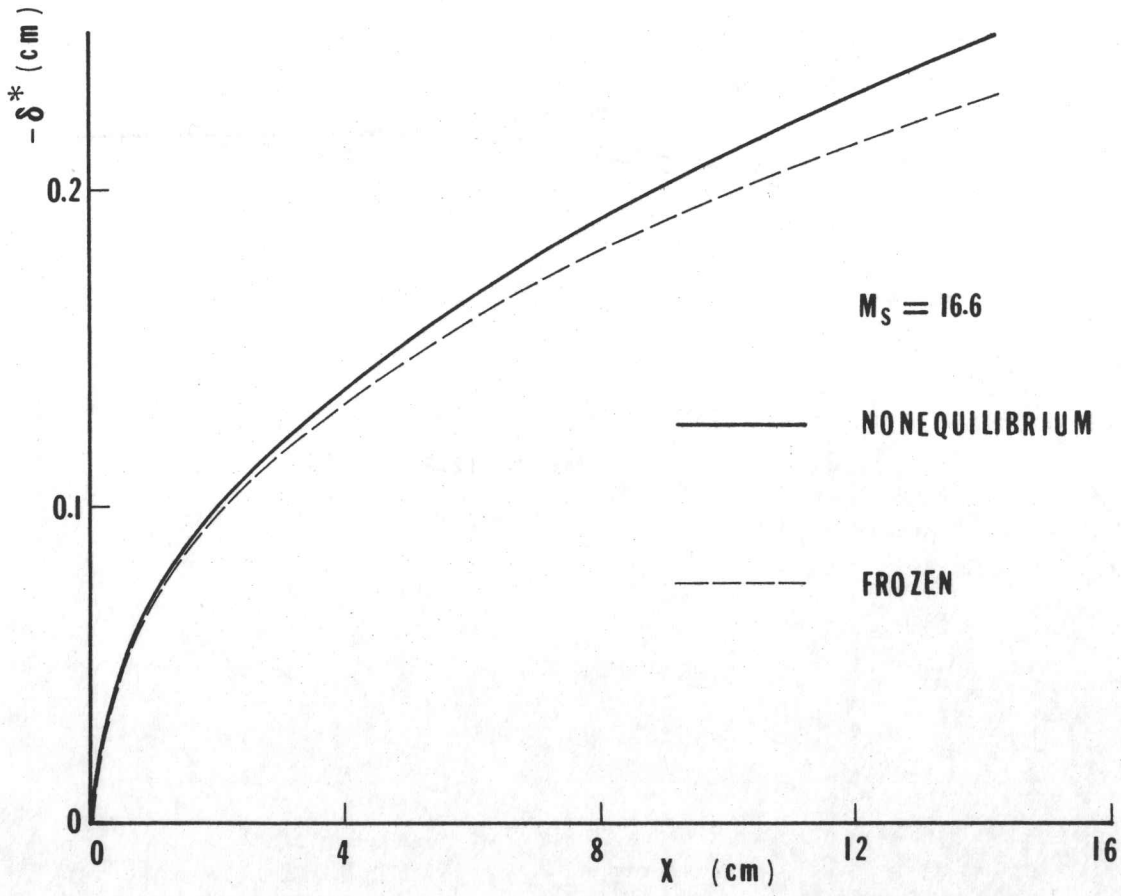

FIG. 24 VARIATIONS OF FLAT-PLATE NONEQUILIBRIUM AND FROZEN BOUNDARY-LAYER DISPLACEMENT-THICKNESSES WITH DISTANCE X FOR M_s = 16.6, p_o = 4.81 TORR AND T_o = 296 K.

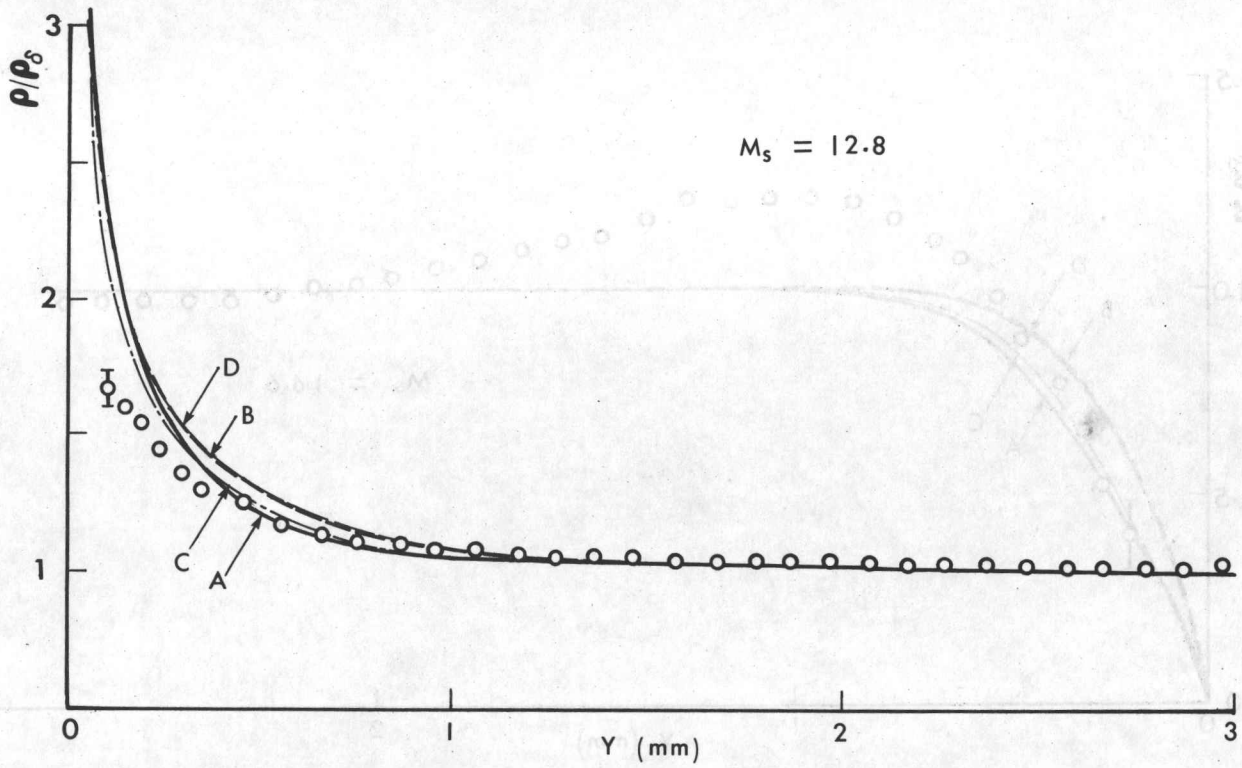

FIG. 25 COMPARISON OF ANALYTICAL AND EXPERIMENTAL NORMALIZED PROFILE FOR PLASMA DENSITY ρ/ρ_δ FOR FLAT-PLATE BOUNDARY LAYER AT X = 14 CM, M_s = 12.8, p_o = 5.01 TORR AND T_o = 297 K. (FOR OTHER NOTATIONS, SEE FIG. 21.)

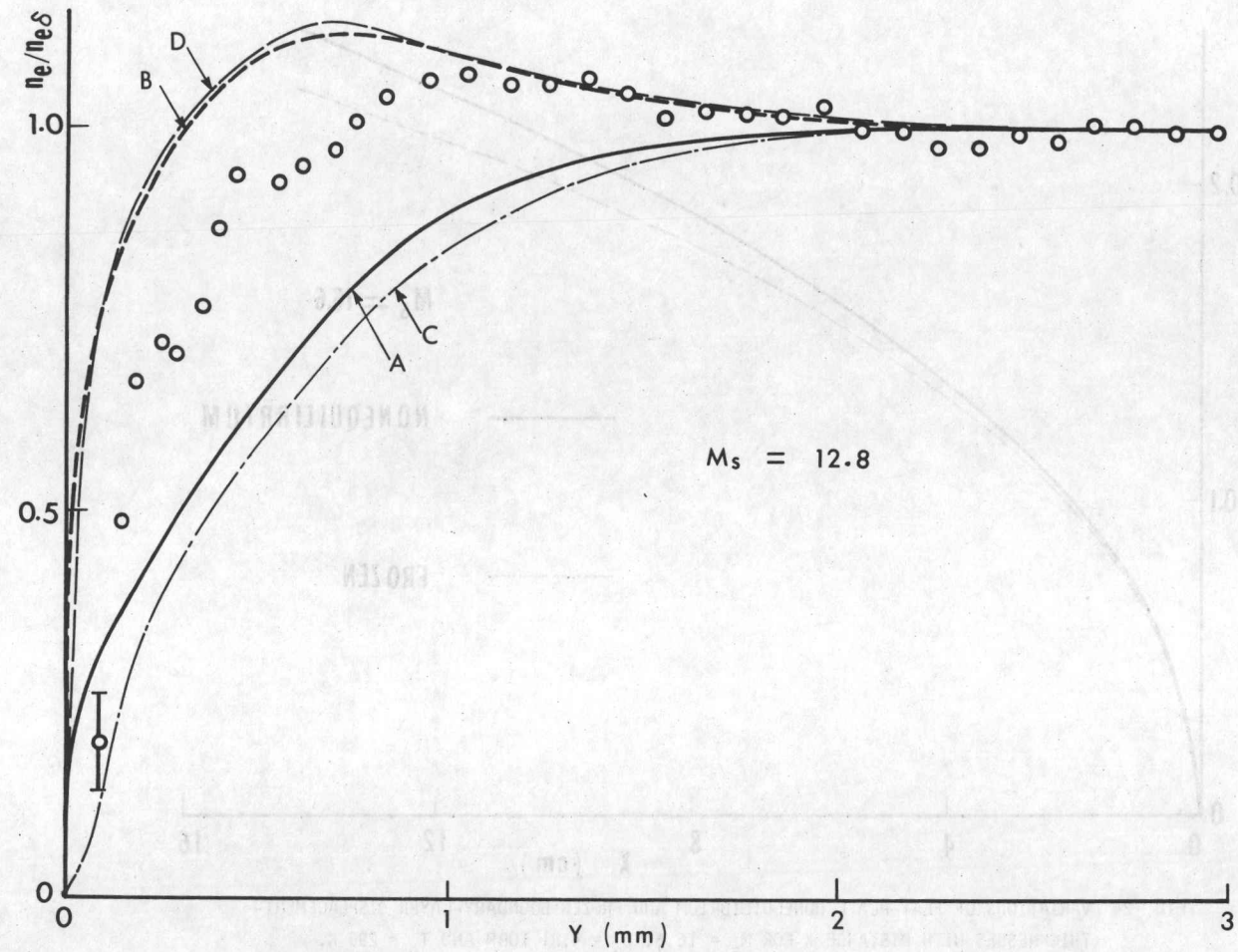

FIG. 26 COMPARISON OF ANALYTICAL AND EXPERIMENTAL NORMALIZED PROFILE FOR ELECTRON NUMBER DENSITY $n_e/n_{e\delta}$ IN THE FLAT-PLATE BOUNDARY LAYER AT X = 14 CM, M_s = 12.8, p_o = 5.01 TORR AND T_o = 297 K. (FOR OTHER NOTATIONS, SEE FIG. 21.)

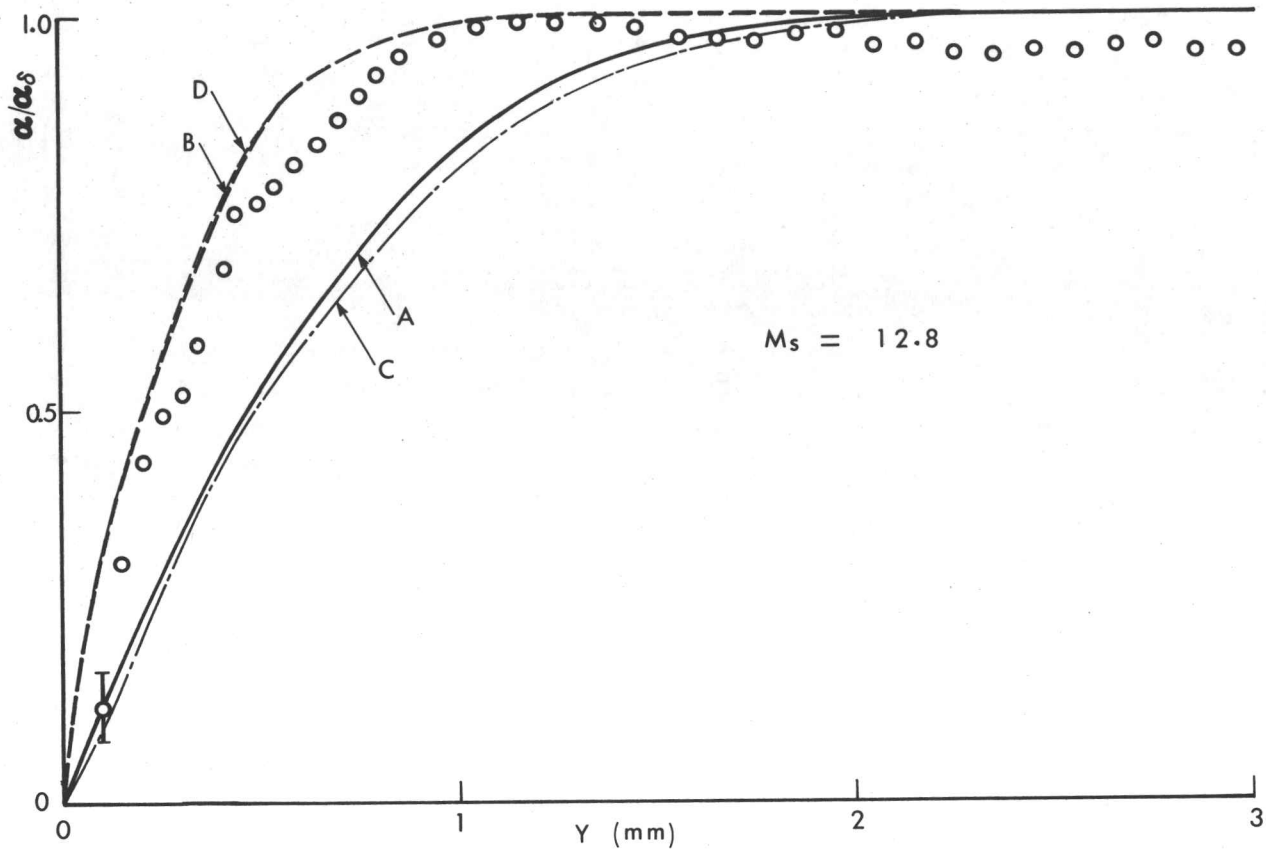

FIG. 27 COMPARISON OF ANALYTICAL AND EXPERIMENTAL NORMALIZED PROFILE FOR DEGREE OF IONIZATION α/α_δ FOR FLAT-PLATE BOUNDARY LAYER AT X = 14 CM, M_s = 12.8, p_o = 5.01 TORR AND T_o = 297 K. (FOR OTHER NOTATIONS, SEE FIG. 21.)

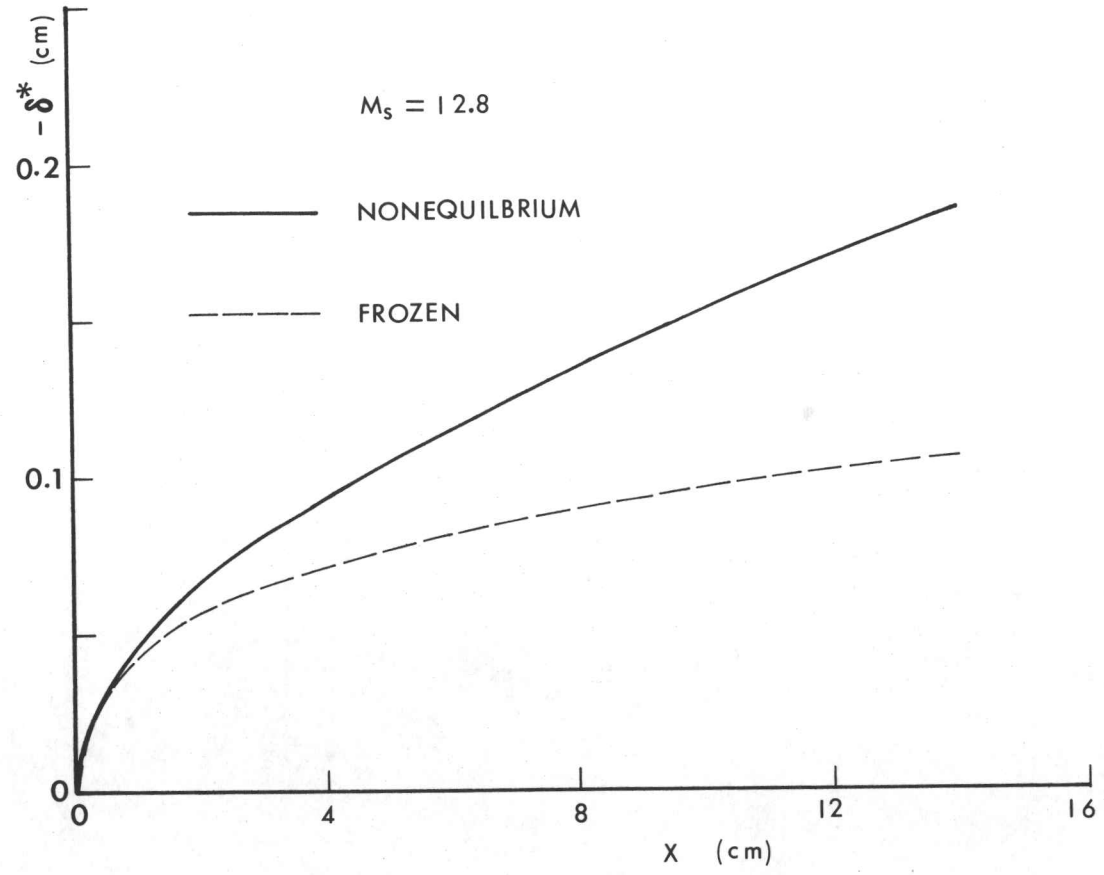

FIG. 28 VARIATIONS OF FLAT-PLATE NONEQUILIBRIUM AND FROZEN BOUNDARY-LAYER DISPLACEMENT-THICKNESSES WITH DISTANCE X FOR M_s = 12.8, p_o = 5.01 TORR AND T_o = 297 K.

APPENDIX A

AREA AVERAGED QUASI-ONE-DIMENSIONAL FLOW EQUATIONS

In the shock-fixed coordinates, the area-averaged mass conservation equation (Eq. 18) is rewritten as follows. Let the operator $< >$ be introduced in an area-averaging process, and let A and L be the cross-sectional area and perimeter of a shock tube, respectively. A schematic profile is shown in Fig. A1.

$$\langle \rho u \rangle = \frac{1}{A} \int \rho u dA$$

$$= \frac{1}{A} \left\{ \rho u \int dA + L \int_{\text{b.layer}} (\rho' u' - \rho u) dy \right\} \tag{A1}$$

$$= \frac{1}{A} \rho u (A - L\delta^*)$$

where the primed quantities represent variables across the boundary layer and δ^* is the boundary-layer-displacement thickness defined by

$$\delta^* = \int_{\text{b.layer}} \left(1 - \frac{\rho' u'}{\rho u} \right) dy \tag{A2}$$

which is negative, as expected. ρ and u are the uniform values.

Here inside the boundary layer, the mass conservation equation

$$\frac{\partial \rho' u'}{\partial x} + \frac{\partial \rho' v'}{\partial y} = 0 \tag{A3}$$

holds. If we integrate Eq. (A3) across the boundary layer, we have the following relation:

$$(\rho' v')_\delta = - \frac{d}{dx} \int_{\text{b.layer}} \rho' u' dy \tag{A4}$$

where δ denotes the condition at the outer edge of the boundary layer.

For an arbitrary quantity Q, its convective derivative averaged across the shock tube cross-sectional area is given, taking into account Eqs. (A4) and (A3), by

$$\frac{d}{dx}\langle \rho u Q\rangle + \frac{\partial}{\partial y}\langle \rho v Q\rangle$$

$$= \frac{1}{A}\frac{d}{dx}\rho u Q(A - \delta^* L) + \frac{L}{A}\frac{d}{dx}\int_{\text{b.layer}} (\rho' u Q' - \rho' u' Q)dy$$

$$= \frac{1}{A}\frac{d}{dx}\rho u Q\{A - L(\delta^* + \delta_Q')\} \tag{A5}$$

where δ_Q' is defined by

$$\delta_Q' = \int_{\text{b.layer}} \frac{\rho' u'}{\rho u}\left(1 - \frac{Q'}{Q}\right)dy \tag{A6}$$

This is the commonly used boundary-layer thickness for Q, which represents u, α, H and αT_e corresponding to the momentum, electron mass, energy and electron energy conservation equations, respectively.

Here we rewrite the boundary-layer thickness for Q as

$$\delta_Q = \delta^* + \delta_Q' \tag{A7}$$

$$= \int_{\text{b.layer}} \left(1 - \frac{\rho' u' Q'}{\rho u Q}\right)dy$$

Finally we have an area-averaged quasi-one-dimensional expression as follows:

$$\langle \rho u Q\rangle = \frac{1}{A}\rho u Q(A - \delta_Q L) \tag{A8}$$

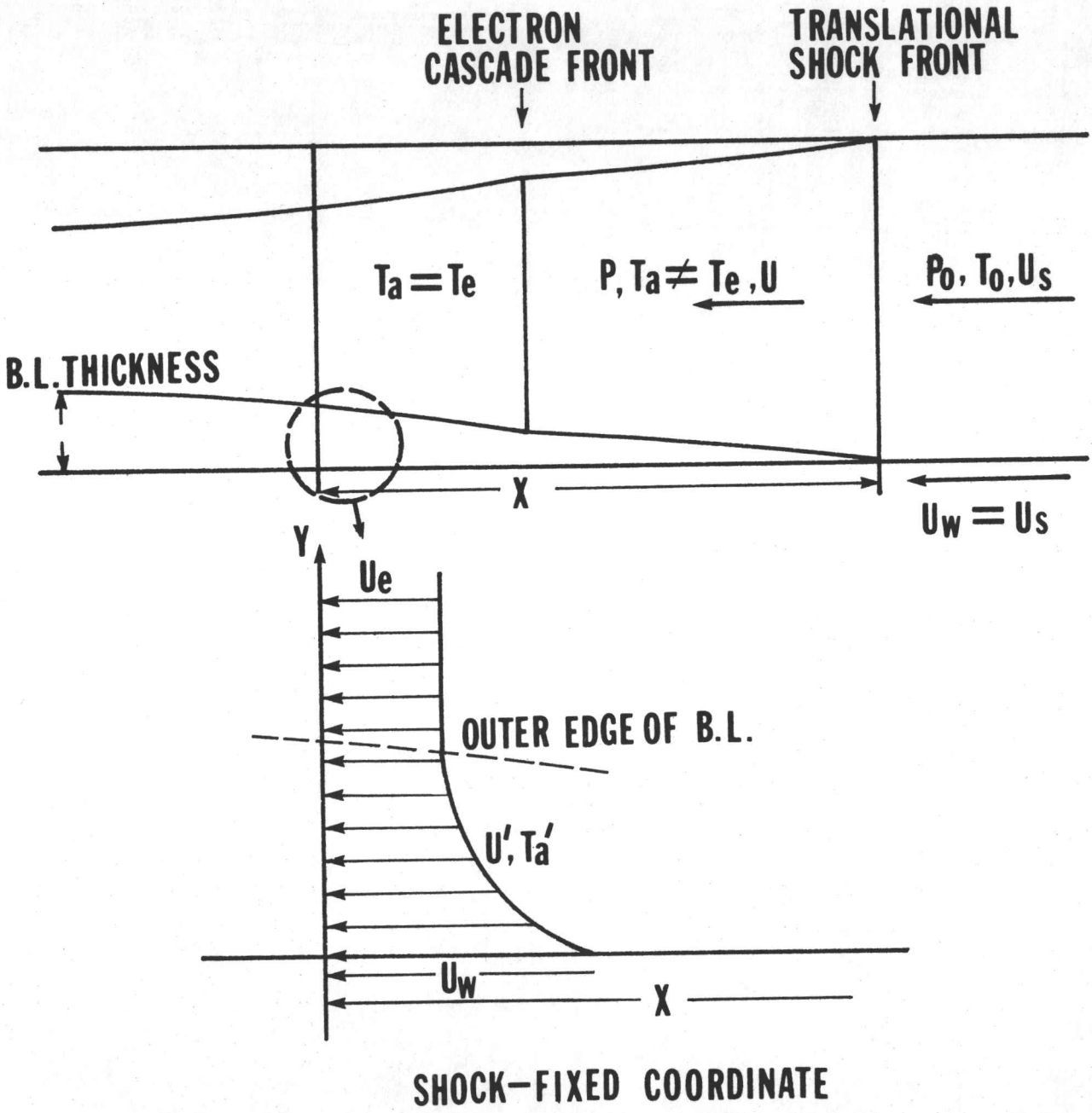

FIG. A1 IONIZING ARGON SIDEWALL BOUNDARY LAYER IN SHOCK-FIXED COORDINATES.

APPENDIX B

BOUNDARY LAYER THICKNESSES AND WALL DISSIPATION TERMS

Once various boundary-layer thicknesses and wall dissipation terms are given, we can determine the shock-wave structure in ionizing argon by making use of these mutual interaction terms. The boundary-layer thicknesses as well as wall dissipation terms used in the present analyses are presented here.

In Figs. B1(a) and B1(b), variations of the boundary-layer displacement thickness $-\delta^*$ and the velocity thickness $-\delta_u$ with distance x are shown for shocks with shock Mach numbers $M_s = 13.1$ and $M_s = 15.9$, respectively. The thicknesses are defined by

$$\delta^* = \int \left(1 - \frac{\rho' u'}{\rho u} \right) dy < 0$$

$$\delta_u = \int \left(1 - \frac{u'}{u} \right) dy < 0 \qquad \text{(B1)}$$

where primed quantities show those across the boundary layer. δ^* and δ_u are negative in the shock-fixed coordinate, as expected. It is noted that the bump appears in both nonequilibrium and frozen boundary-layer flows at the electron-cascade front where the electron number density production rate $\dot{n}_e$ is greatest. Therefore these boundary-layer thickness growths are no longer monatonically increasing as seen in the similar boundary layer analysis for perfect argon. The velocity boundary-layer thicknesses $-\delta_u$ temporarily decrease at the electron-cascade front due to the sharp changes of boundary-layer profiles. The phenomena are even greater in higher shock-wave Mach numbers.

Figure B2 shows the variation of $-\delta^*/\sqrt{x}$ with distance x for shock-waves with $M_s = 13.1$ and 15.9. In the similar laminar boundary-layer analysis for perfect argon, the sidewall boundary-layer displacement thickness $-\delta^*$ is growing with $\sqrt{x}$. Figure B2 shows roughly a coefficient of the displacement thickness growth, which is proportional to the square root of the Reynolds number referring to the uniform flow condition. The value of $-\delta^*/\sqrt{x}$ is initially constant in the incubation region between the shock front and the electron-cascade front and then suddenly changes to another quasi-equilibrium value across the electron-cascade front. The reasons for this are as follows. Pressure changes roughly from a constant value in the incubation region to another constant value behind the electron-cascade front. In other words, the flow Reynolds number changes suddenly across the electron-cascade front. Values of $-\delta^*/\sqrt{x}$ at $x = 0$ ($-\delta^*/\sqrt{x} = 0.1006$ at $M_s = 13.1$ and $-\delta^*/\sqrt{x} = 0.1064$ at $M_s = 15.9$) are important because these values are used in calculating shock-wave structures by Enomoto's model. This model considers only the boundary-layer displacement thickness which is obtained by a similar boundary-layer analysis. In Fig. B3, variations of momentum thickness δ_m with distance x are shown for shocks $M_s = 13.1$ and 15.9,

$$\delta_m = \delta^* + \int \frac{\rho' u'}{\rho u} \left(1 - \frac{u'}{u} \right) dy \qquad \text{(B2)}$$

Solid lines and dashed lines show nonequilibrium and frozen boundary layer, respectively. Inflection points appear at the electron-cascade front owing to the same reasons as explained in Figs. B1(a) and B1(b). Differences between nonequilibrium and frozen boundary-layer flows are found to be very small.

Figure B4 shows the energy dissipation thickness δ_e for shocks M_s = 13.1 and 15.9, where

$$\delta_e = \delta^* + \int \frac{\rho' u'}{\rho u} \left(1 - \frac{u'^2}{u^2} \right) dy \qquad \text{(B3)}$$

Curve A (——) and curve B (---) correspond to nonequilibrium and frozen boundary-layer flows, respectively. The same remarks made for Fig. B3 can be applied to this case.

Figure B5 shows variations of the degree of ionization thickness δ_α with distance x for shocks M_s = 13.1 and 15.9, where

$$\delta_\alpha = \delta^* + \int \frac{\rho' u'}{\rho u} \left(1 - \frac{\alpha'}{\alpha} \right) dy \qquad \text{(B4)}$$

Curve A (——) and curve B (---) correspond to nonequilibrium and frozen boundary-layer flows, respectively. As mentioned previously, overshoots of the α profile occur across the nonequilibrium boundary layer just behind the electron-cascade front as shown in Figs. 16 and 19. They do not appear in the frozen boundary-layer flow. Consequently, δ_α in the nonequilibrium boundary-layer flow can be positive around the electron-cascade front and is a maximum at a distance where the electron number density production rate is greatest. On the other hand, δ_α in the frozen boundary-layer flow is always negative and monotonically decreases with distance x. It is worth noting that $\alpha/\alpha_\delta = 0.99$ contours in Figs. 20(a) and 20(b) are similar to the results obtained for the degree of ionization boundary-layer thickness in the nonequilibrium boundary-layer, which is defined as

$$\int \frac{\rho' u'}{\rho u} \left(1 - \frac{\alpha'}{\alpha} \right) dy$$

Figure B6 shows variations of the radiation energy loss thickness δ_R with distance x for shocks M_s = 13.1 and 15.9, where

$$\delta_R = \int \left(1 - \frac{Q_R'}{Q_R} \right) dy \qquad \text{(B5)}$$

Curves A (——) and B(---) correspond to nonequilibrium and frozen boundary-layer flows, respectively. δ_R in the nonequilibrium boundary layer is

always positive. This fact indicates that radiation energy losses inside the nonequilibrium boundary layer are smaller than those in the inviscid core. δ_R is a maximum at the electron-cascade front where the averaged radiation energy loss inside the nonequilibrium boundary layer is smallest. The radiation energy losses in the frozen boundary layer are larger than those in the inviscid core, since δ_R is negative, as shown in Fig. B6. In the nonequilibrium boundary layer, kinetic energy is transformed into excitation of the internal electronic states, and ionization rate processes. Hence the temperature decreases more than in the frozen boundary layer where the ionization and recombination processes are assumed completely frozen. Therefore, the radiation energy losses are more prominent in the frozen boundary-layer flow than in the nonequilibrium boundary-layer flow. However, throughout the previous and present analysis, the effect of re-absorption of radiation energy in the radiation cooling zone is not considered.

Figure B7 shows variations of the nonequilibrium electron-number density thickness δ_{n_e} with distance x for shocks M_s = 13.1 and 15.9, where

$$\delta_{n_e} = \int \left(1 - \frac{n'_e}{n_e} \right) dy \tag{B6}$$

As shown, there is a maximum at the electron-cascade front. The electron number density in the inviscid core is a maximum. The electron number density profile across the nonequilibrium boundary layer near the electron-cascade front is shown in Fig. 15 where the profiles are compared at x = 9.5 cm behind the shock front and the experimental relaxation length is about 9.0 cm. In Fig. 18 similar comparisons are made at x = 18.0 cm behind the shock front and the experimental relaxation length is 2.0 cm. There is evidence, from Figs. 15 and 18, that the maximum deviation of the electron number density between the inviscid core and the boundary layer occurs at the electron-cascade front.

In Fig. B8, variations of the electron energy transfer rate thickness δ_Q and the electron production rate thickness $\delta_{\dot{n}}$ with distance x are shown by curves A and B, respectively, where

$$\delta_Q = \int \left(1 - \frac{Q'_{el} + Q'_{inel}}{Q_{el} + Q_{inel}} \right) dy$$

$$\delta_{\dot{n}} = \int \left(1 - \frac{n'_e}{n_e} \right) dy \tag{B7}$$

As shown, these curves are similar to each other and the largest deviation between curves A and B is at most 25% at M_s = 13.1. Therefore, the approximation of $\delta_Q \approx \delta_{\dot{n}}$ in Eq. (34) is acceptable. δ_Q and $\delta_{\dot{n}}$ are negligible in the quasi-equilibrium region since in the processes of computation δ_Q and $\delta_{\dot{n}}$ are written as $(Q_{el} + Q_{inel})\delta_Q$ and $\dot{n}_e \delta_{\dot{n}}$, On the other hand, in the quasi-equilibrium region the ionization rate processes are in equilibrium, $\dot{n}_e$ $(x > x_E) \rightarrow 0$, and consequently the electron energy transfer rate is negligibly small.

Wall dissipation terms were used to express the mutual interaction in analysing the area averaged quasi-one-dimensional ionizing shock-wave structure. It is helpful to show the proper expressions of these terms in Figs. B9-B12.

In perfect-gas boundary-layer flows in a shock tube, the local skin friction coefficient c_f is related to the Reynolds number by (see Glass et al, Ref. B1),

$$c_f \sqrt{Re} = \frac{\sqrt{2}\, f''(0)}{\left|1 - \frac{u_w}{u_\delta}\right|} \tag{B8}$$

where the local skin friction coefficient

$$c_f = \frac{\tau_w}{\frac{1}{2}\rho_w U_\delta \left(1 - \frac{u_w}{u_\delta}\right)^2} \tag{B9}$$

$$Re = \frac{\rho_w U_\delta X}{\mu_w}\left(1 - \frac{u_w}{u_\delta}\right)^2$$

and the shear stress at the wall

$$\tau_w = \left(\mu \frac{\partial u}{\partial y}\right)_w$$

For strong shock waves in perfect argon, Eq. (B8) is given by

$$c_f \sqrt{Re} = 1.914 \tag{B10}$$

where $f''(0) = -4.062$ and $U_w/U_s = 4$ (see Mirels, Ref. B2).

For a real-gas sidewall boundary-layer analysis in ionizing argon, the shear stress is given in boundary-layer coordinates as

$$\tau_w = \frac{\rho_w \mu_w u_s^2}{\sqrt{2\xi}} f''(0) \tag{B11}$$

where

$$\xi = \int \rho_\delta(x)\mu_o(x)u_e(x)\,dx$$

By defining the Reynolds number

$$Re = \frac{\rho_w U_s \bar{X}}{\mu_w} \left(1 - \frac{u_w}{u_s} \right)^2$$

where

$$\bar{X} = \frac{\int \rho_\delta \mu_\delta u_\delta dx}{\rho_\delta \mu_\delta u_\delta}$$

We obtain an expression similar to Eq. (B8):

$$c_f \sqrt{Re} = \frac{\sqrt{2}\, Cf''(0)}{\left| 1 - \frac{u_w}{u_\delta} \right|} \tag{B12}$$

where

$$C = \frac{\rho_w \mu_w}{\rho_\delta \mu_\delta}$$

As expected, this equation reduces to Eq. (B8), if we assume constant inviscid uniform flow properties along the shock-tube axis and C = 1 across the sidewall boundary layer. In Fig. B9, the local skin friction coefficient profiles are shown for M_s = 13 and 16. As expected, the local skin friction coefficients are not monotonically decreasing functions of x but increase with x near the electron-cascade front. Since the pressure gradient is a maximum there, the shear stress increases. Therefore, the value of $c_f \sqrt{Re}$, shown in Fig. B10, is also a maximum at the electron-cascade front. This effect is much different from the results in the boundary-layer analysis in perfect argon, and even greater at higher shock Mach number M_s = 16, as drawn. The value of $c_f \sqrt{Re}$ at x = 0 cm is about 1.58 for both M_s = 13.1 and 15.9. Although this value is calculated from a similar boundary-layer analysis for the frozen uniform flow conditions, it is different from that of the perfect gas where $c_f \sqrt{Re}$ = 1.914. This is due to the two-temperature effect of the argon plasma used in the analysis, and the variation of transport properties across the boundary layer, such as C = C(y) ≠ const, was taken into account.

The sidewall heat-transfers due to atom and electron are shown in Figs. B11(a) and B11(b) for M_s = 13.1 and 15.9, respectively. The wall heat transfer due to atom temperature gradient $-\dot{q}_a$ is not a monotonically decreasing function of x but locally increases at the electron-cascade front. This effect is even greater at higher shock Mach number M_s = 16. However, the heat transfer due to the electron $-\dot{q}_e$ has a maximum at the electron-cascade front.

The local Nusselt numbers are defined as follows:

$$Nu = \frac{-\bar{X}\, \dot{q}}{\lambda (T_\delta - T_w)} \tag{B13}$$

where $\dot{q}$ is the heat flux at the sidewall,

$$q = -\left(\lambda \frac{\partial T}{\partial y}\right)_w \tag{B14}$$

Therefore, the local Nusselt numbers are related to the local Reynolds number defined previously, that is,

$$\frac{Nu_a}{\sqrt{Re}} = \frac{\theta'(0)}{\sqrt{2}\ \left|1 - \frac{u_w}{u_\delta}\right| \left(1 - \frac{T_{aw}}{T_{a\delta}}\right)} \tag{B15}$$

where $\theta = T_a/T_{a\delta}$ for the atom temperature. For the electron, the relationship between Nu_e and Re is

$$\frac{Nu_e}{\sqrt{Re}} = \frac{\frac{T_{e\delta}}{T_{a\delta}}\theta'(0)}{\sqrt{2}\ \left|1 - \frac{u_w}{u_\delta}\right| \left(1 - \frac{T_{aw}}{T_{a\delta}}\right)} \tag{B16}$$

where $\Theta = T_e/T_{e\delta}$.

The ion-recombination heat transfer at the sidewall $\dot{q}_\alpha$ is defined by

$$\dot{q}_\alpha = -RT_I \left(\rho D_m \frac{\partial \alpha}{\partial y}\right)_w \tag{B17}$$

The Nusselt number due to $\dot{q}_\alpha$ and the local Reynolds number are related as follows:

$$\frac{Nu_\alpha}{\sqrt{Re}} = \frac{\frac{\alpha T_I}{T_{a\delta}} Z'(0)}{\sqrt{2}\ \left|1 - \frac{u_w}{u}\right| \left(1 - \frac{T_{aw}}{T_{a\delta}}\right)} \tag{B18}$$

where $Z = \alpha/\alpha_\delta$.

Figures B12(a) and B12(b) show variations of $Nu/\sqrt{Re}$ defined by Eqs. (B15), (B16) and (B18) for shock Mach numbers M_s = 13.1 and 15.9, respectively. $Nu_a/\sqrt{Re}$ and $Nu_e/\sqrt{Re}$ are maxima at the electron-cascade front. However, for the ion-recombination heat transfer, $Nu_\alpha/\sqrt{Re}$ is a maximum at a distance behind the electron-cascade front. The reason for this is as follows. The gradient of the degree of ionization at the sidewall $Z'(0)$ is monotonically decreasing with distance x. However, α_δ, at first, increases from its frozen value at x = 0 to the quasi-equilibrium peak value and then slowly decreases due to the radiation energy loss. Therefore $\alpha_\delta Z'(0)$ is a maximum not at the electron-cascade front but at a distance behind it. This effect is obvious in Fig. 12(b) for M_s = 15.9.

In the present analyses, variations of the local skin friction coefficient c_f and the wall heat transfer $-\dot{q}$ are found to differ greatly from the result by the similar boundary layer analysis for perfect argon. The local maxima appear at the electron-cascade front and their variations are not simple in the incubation region as expected in the previous analysis. This shows the importance of taking into account the mutual interaction terms in solving the ionizing shock-wave structure problem.

In the actual flow field, these bumps may be reduced by dissipation effects but there is no experimental evidence that this indeed happens.

REFERENCES

B1. Glass, I. I.
Hall, J. G.
Handbook of Supersonic Aerodynamics, Sec. 18, Shock Tubes. NAVORD Rep. 1488 (1959).

B2. Mirels, H.
"Boundary Layer Behind Shock or Thin Expansion Wave Moving into Stationary Fluid", NACA TN 3712 (1956).

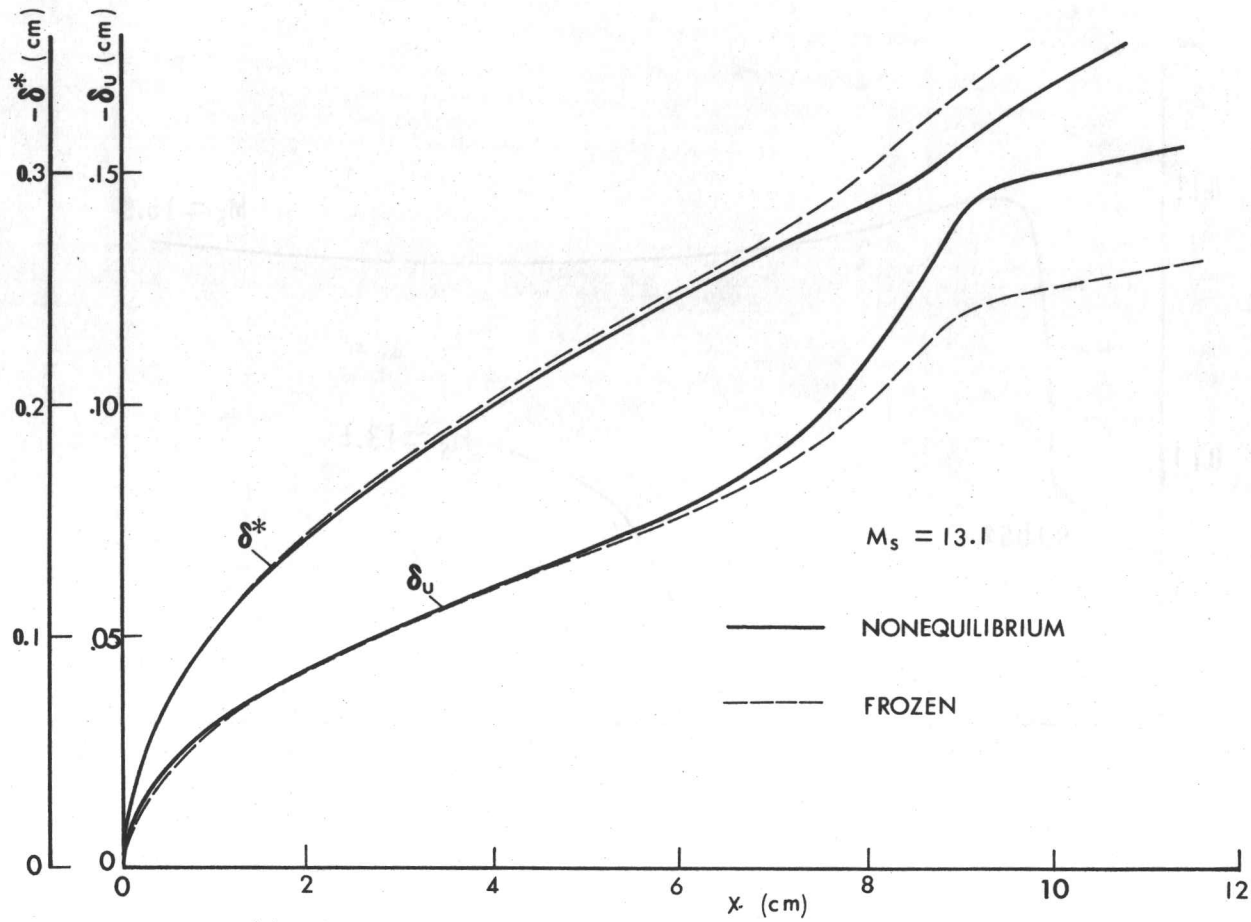

FIG. B1(a) VARIATIONS OF SIDEWALL BOUNDARY-LAYER DISPLACEMENT THICKNESS δ^* AND VELOCITY THICKNESS δ_u WITH DISTANCE X FOR (a) M_s = 13.1, p_o = 5.16 TORR AND T_o = 300 K, AND (b) M_s = 15.9, p_o = 5.10 TORR AND T_o = 298 K. SOLID LINES (——): NONEQUILIBRIUM FLOW; DASHED LINES (--): FROZEN FLOW.

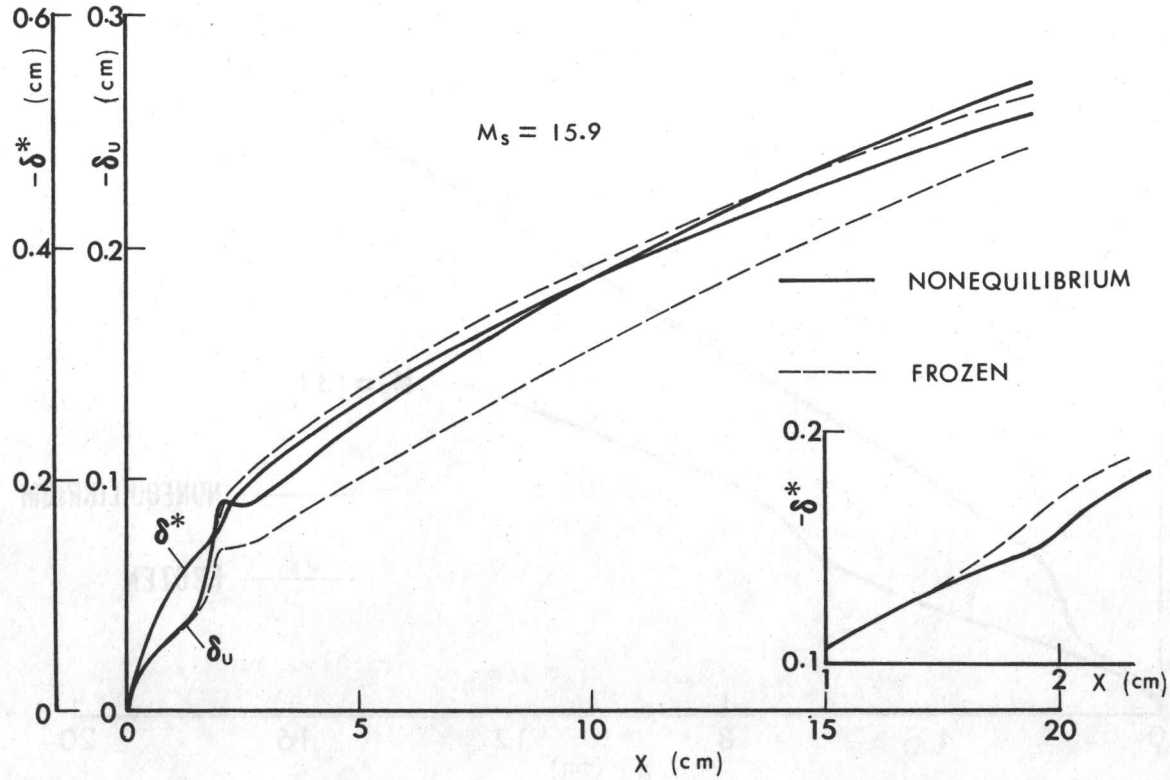

FIG. B1(b) VARIATIONS OF SIDEWALL BOUNDARY-LAYER DISPLACEMENT THICKNESS δ^* AND VELOCITY THICKNESS δ_u WITH DISTANCE X FOR (a) M_s = 13.1, p_o = 5.16 TORR AND T_o = 300 K, AND (b) M_s = 15.9, p_o = 5.10 TORR AND T_o = 298 K. SOLID LINES (——): NONEQUILIBRIUM FLOW; DASHED LINES (--): FROZEN FLOW.

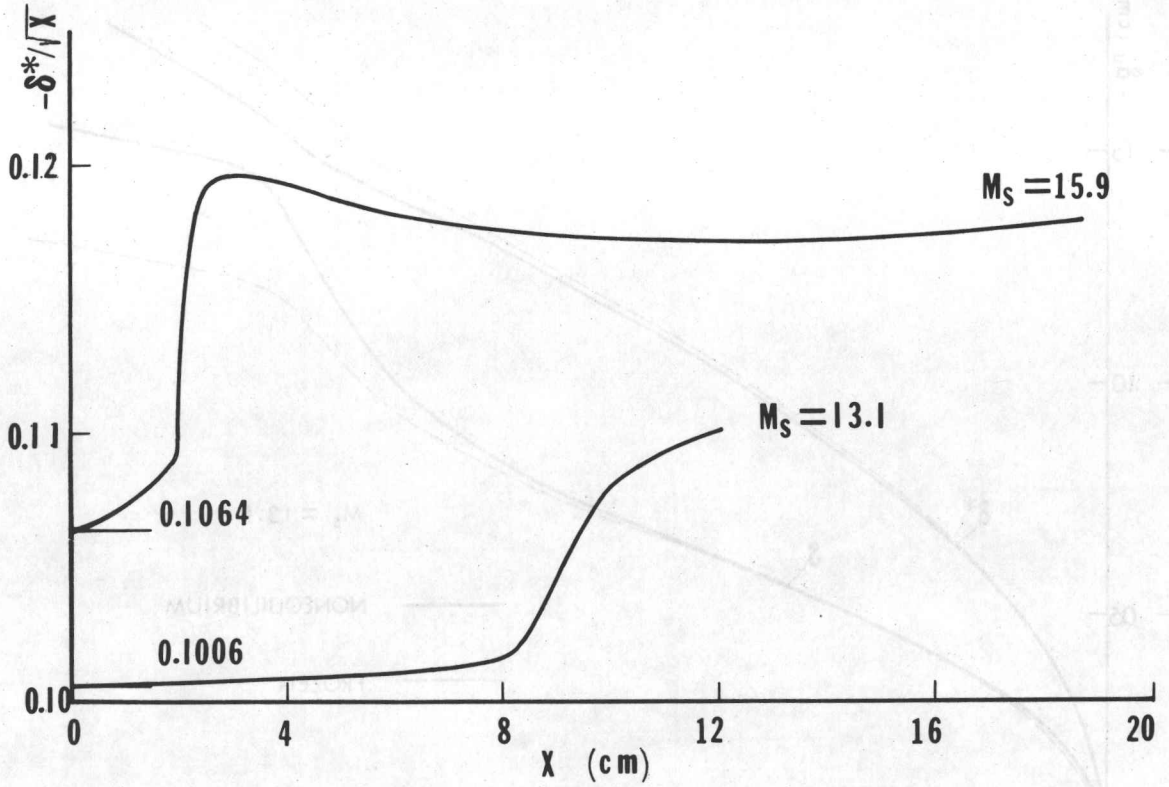

FIG. B2 VARIATIONS OF SIDEWALL BOUNDARY LAYER $\delta^*/\sqrt{X}$ WITH DISTANCE X FOR (a) M_s = 13.1, p_o = 5.16 TORR AND T_o = 300 K, AND (b) M_s = 15.9, p_o = 5.10 TORR AND T_o = 298 K.

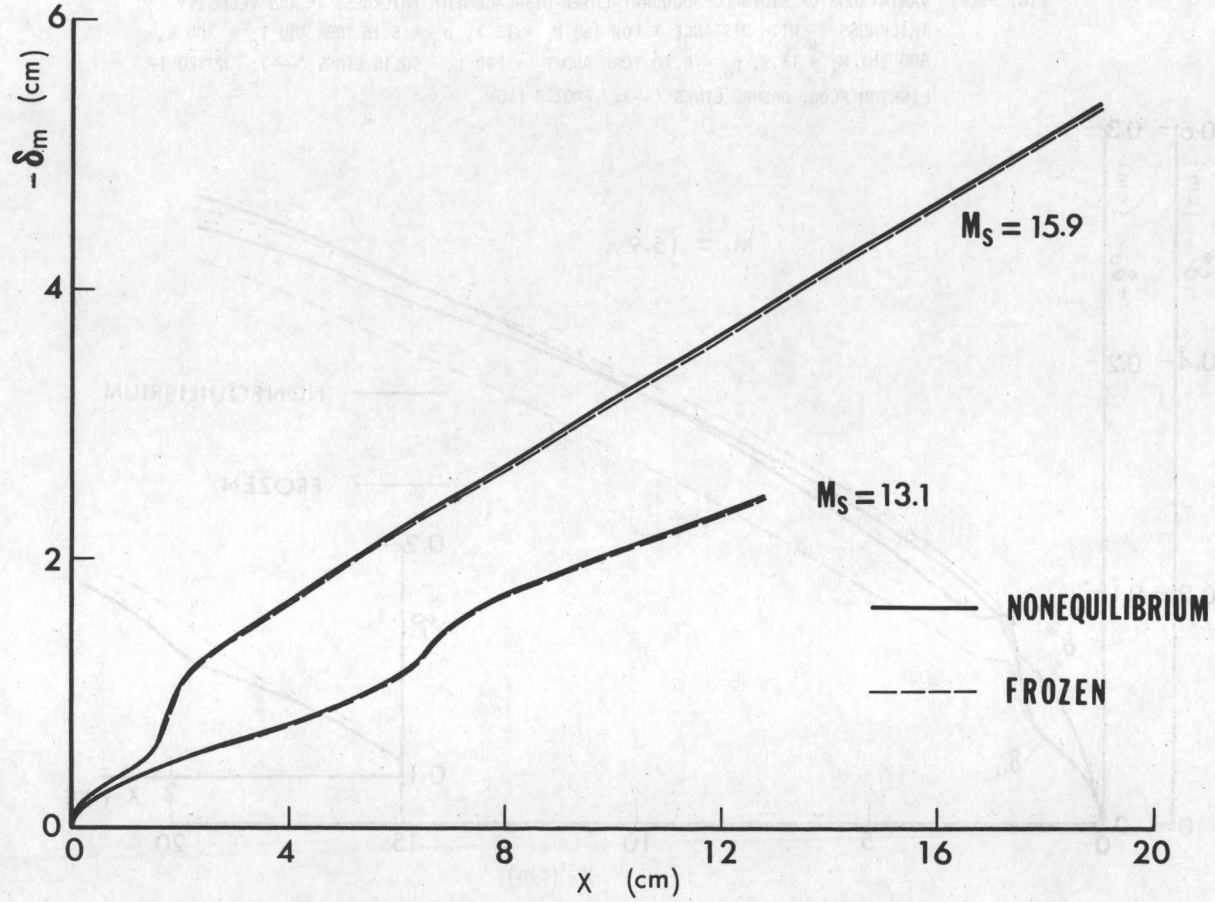

FIG. B3 VARIATIONS OF SIDEWALL BOUNDARY-LAYER MOMENTUM THICKNESS δ_m WITH DISTANCE X FOR (a) M_s = 13.1, p_o = 5.16 TORR AND T_o = 300 K, AND (b) M_s = 15.9, p_o = 5.10 TORR AND T_o = 298 K.

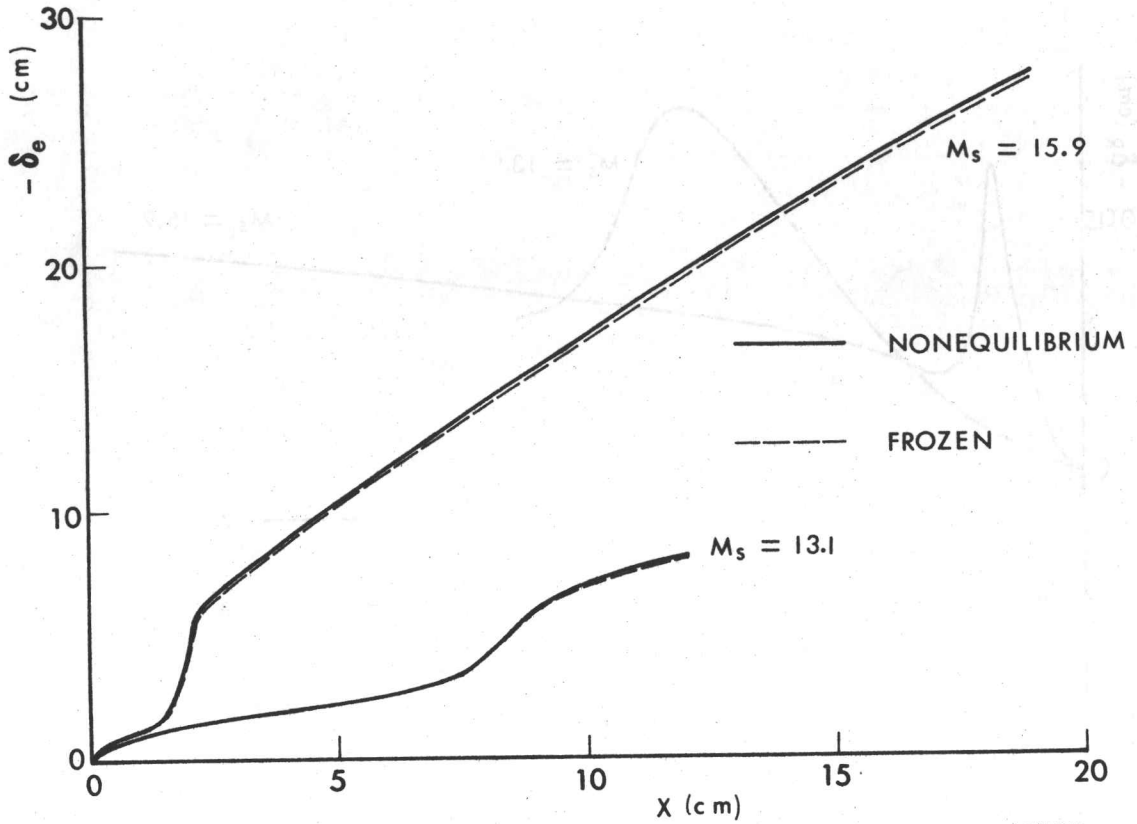

FIG. B4 VARIATIONS OF SIDEWALL BOUNDARY-LAYER ENERGY-DISSIPATION THICKNESS δ_e WITH DISTANCE X FOR CASES WITH (a) M_s = 13.1, p_o = 5.16 TORR AND T_o = 300 K, AND (b) M_s = 15.9, p_o = 5.10 TORR AND T_o = 298 K.

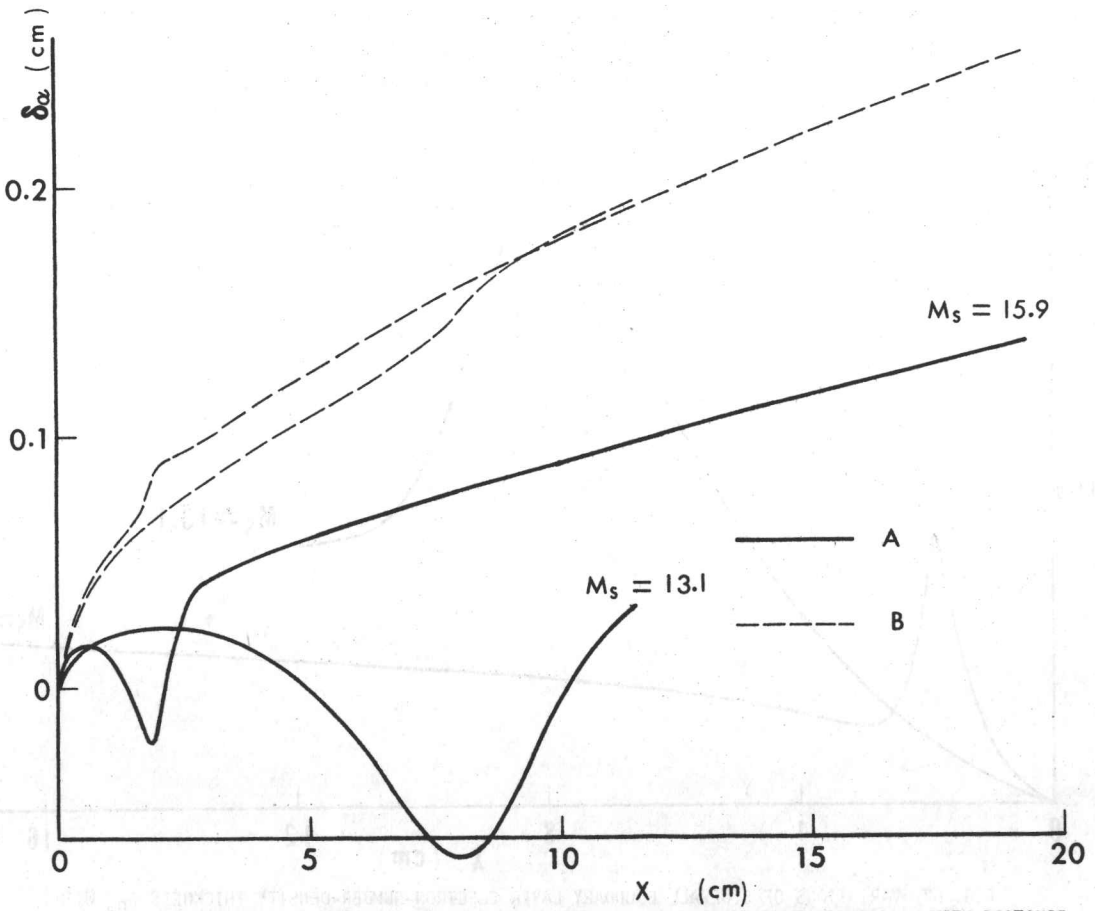

FIG. B5 VARIATIONS OF SIDEWALL BOUNDARY LAYER DEGREE OF IONIZATION THICKNESS $\delta\alpha$ WITH DISTANCE X FOR (a) M_s = 13.1, p_o = 5.16 TORR AND T_o = 300 K, AND (b) M_s = 15.9, p_o = 5.10 TORR AND T_o = 298 K. [FOR NOTATIONS, SEE FIGS. B1(a), B1(b).]

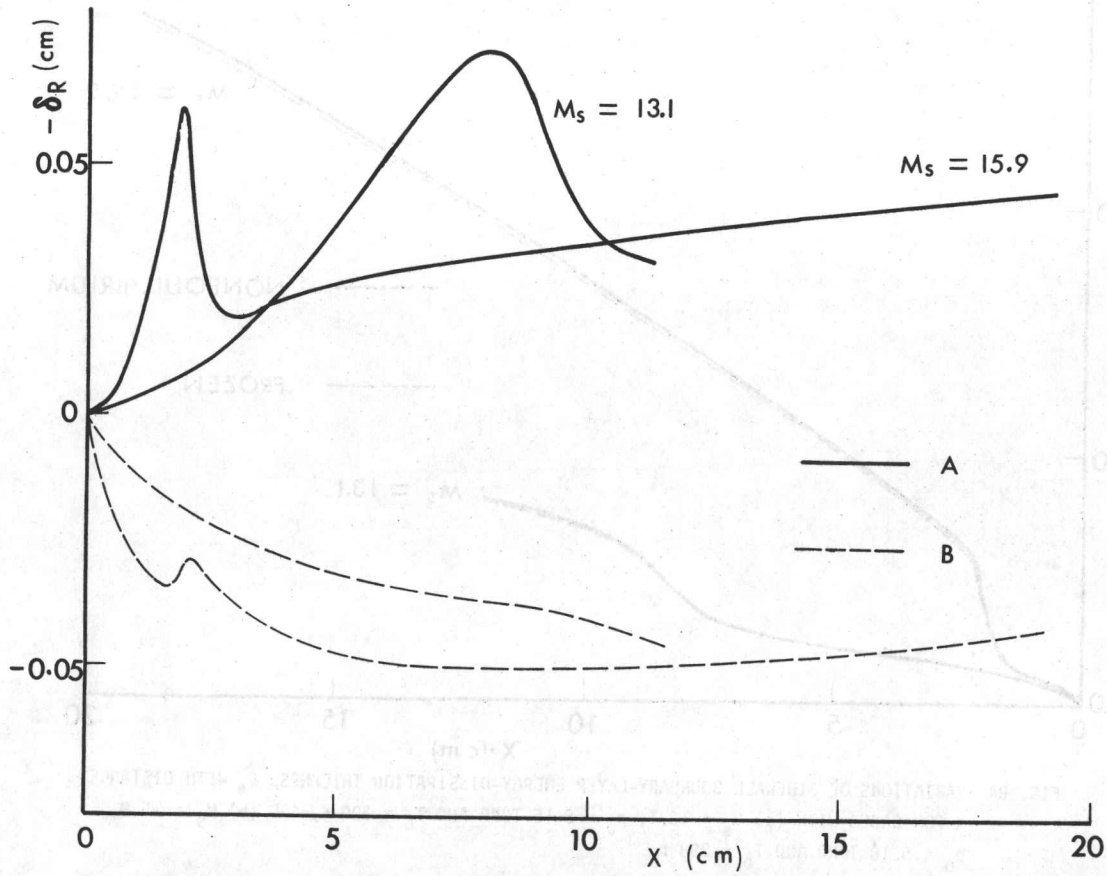

FIG. B6 VARIATIONS OF SIDEWALL BOUNDARY LAYER RADIATION-ENERGY-LOSS THICKNESS δ_R WITH DISTANCE X FOR (a) M_s = 13.1, p_o = 5.16 TORR AND T_o = 300 K, AND (b) M_s = 15.9, p_o = 5.10 TORR AND T_o = 298 K. CURVE A: NONEQUILIBRIUM FLOW; CURVE B: FROZEN FLOW.

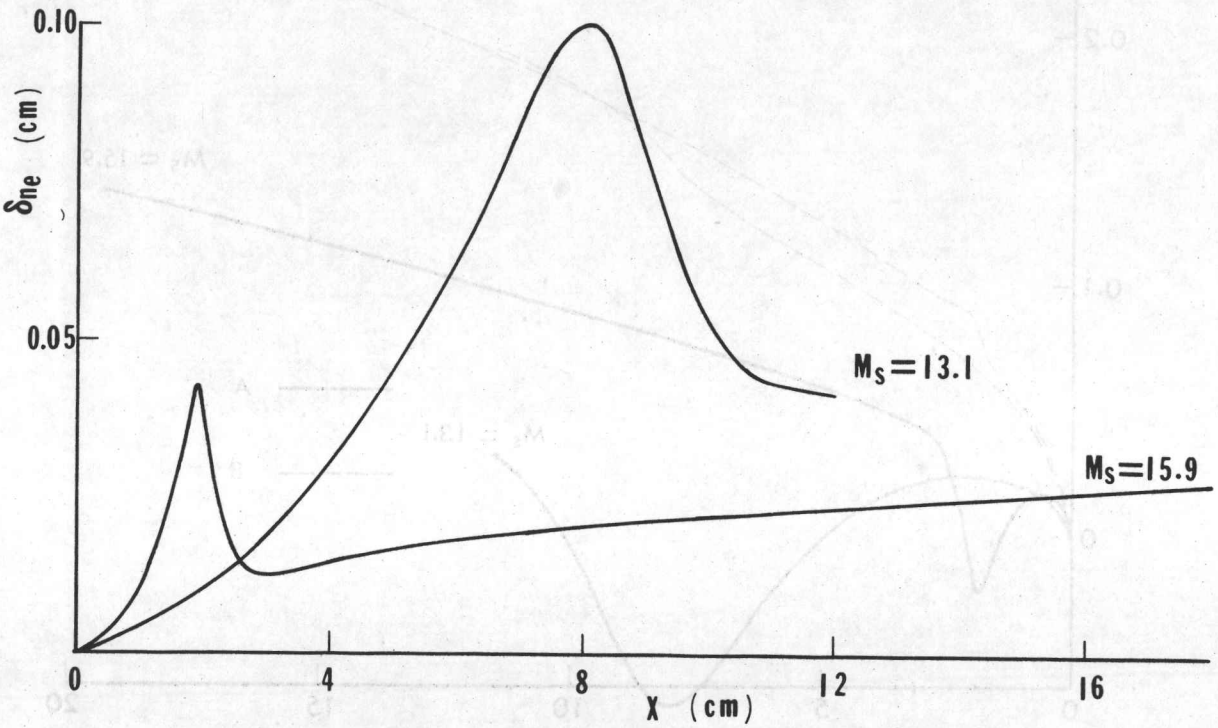

FIG. B7 VARIATIONS OF SIDEWALL BOUNDARY LAYER ELECTRON-NUMBER-DENSITY THICKNESS δ_{n_e} WITH DISTANCE X FOR (a) M_s = 13.1, p_o = 5.16 TORR AND T_o = 300 K, AND (b) M_s = 15.9, p_o = 5.10 TORR AND T_o = 298 K. [FOR NOTATIONS, SEE FIGS. B1(a), B1(b).]

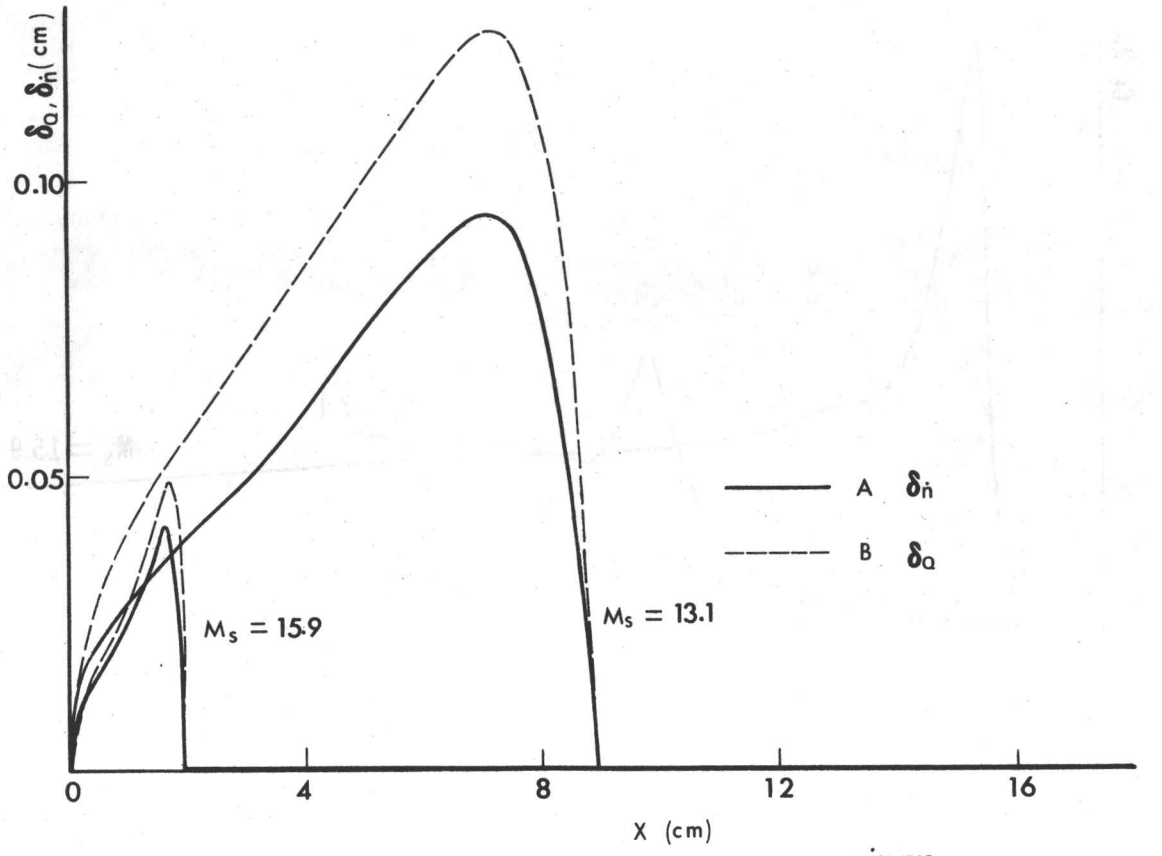

FIG. B8 VARIATIONS OF SIDEWALL BOUNDARY LAYER ELECTRON-ENERGY-TRANSFER-RATE THICKNESS δ_Q AND ELECTRON-PRODUCTION-RATE THICKNESS $\delta_{\dot{n}}$ WITH DISTANCE X FOR (a) M_s = 13.1, p_o = 5.16 TORR AND T_o = 300 K, AND (b) M_s = 15.9, p_o = 5.10 TORR AND T_o = 298 K. CURVE A: δ_Q; CURVE B: $\delta_{\dot{n}}$.

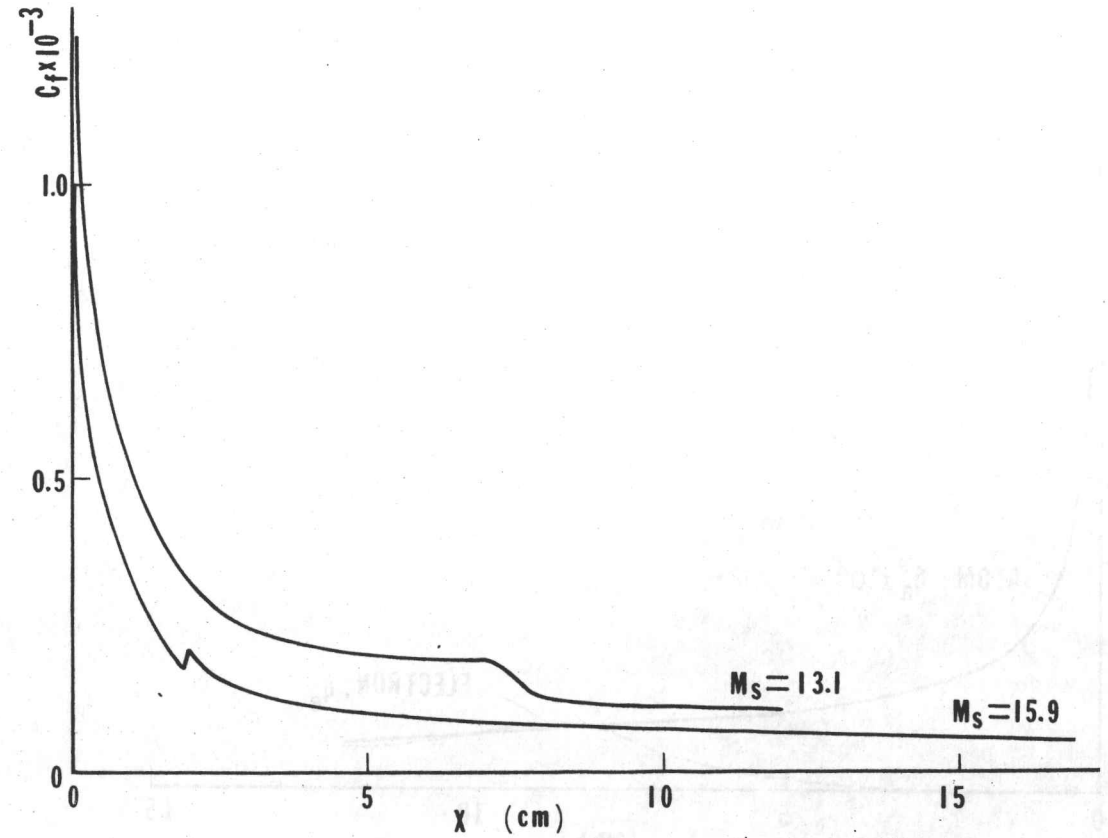

FIG. B9 VARIATIONS OF SIDEWALL BOUNDARY LAYER LOCAL-SKIN-FRICTION COEFFICIENT C_f WITH DISTANCE X FOR (a) M_s = 13.1, p_o = 5.16 TORR AND T_o = 300 K, AND (b) M_s = 15.9, p_o = 5.10 TORR AND T_o = 298 K.

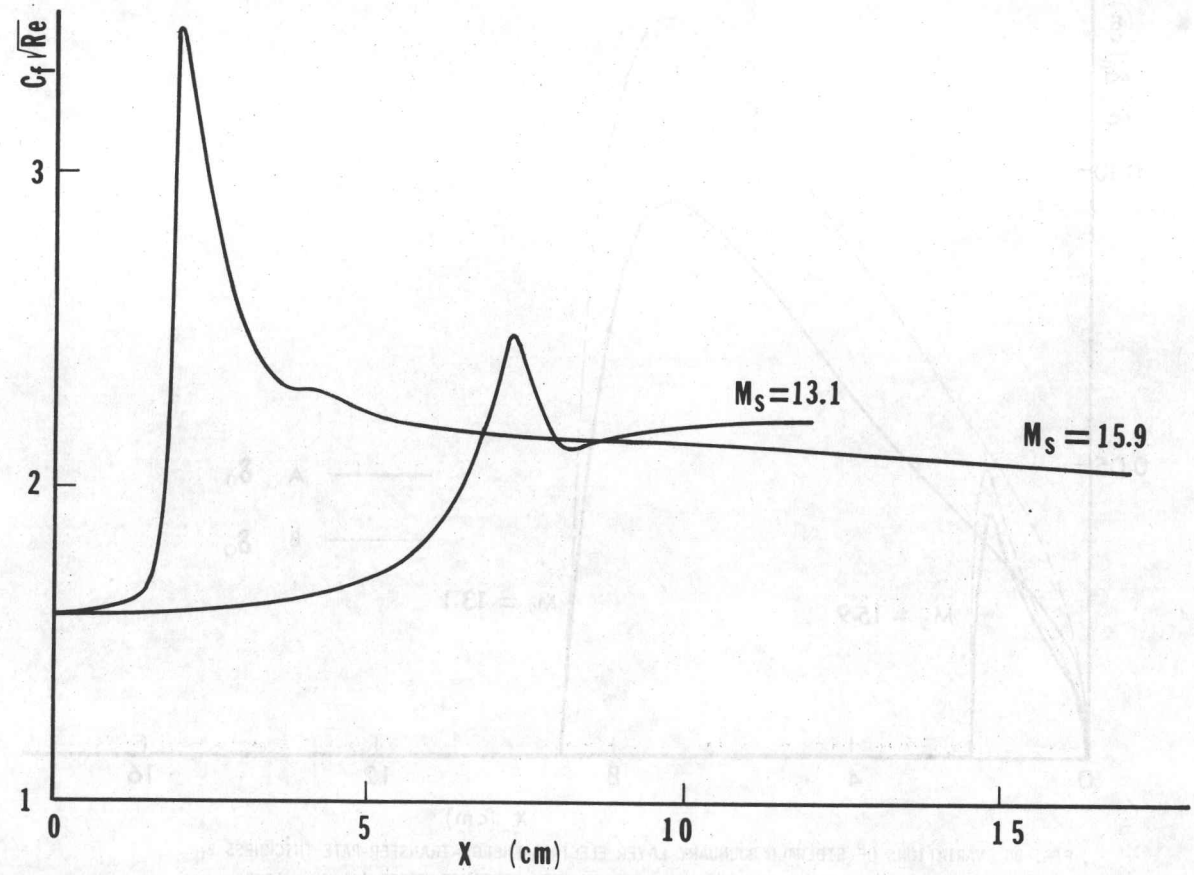

FIG. B10 VARIATIONS OF $C_f\sqrt{Re}$ WITH DISTANCE X FOR (a) M_s = 13.1, p_o = 5.16 TORR AND T_o = 300 K, AND (b) M_s = 15.9, p_o = 5.10 TORR AND T_o = 298 K.

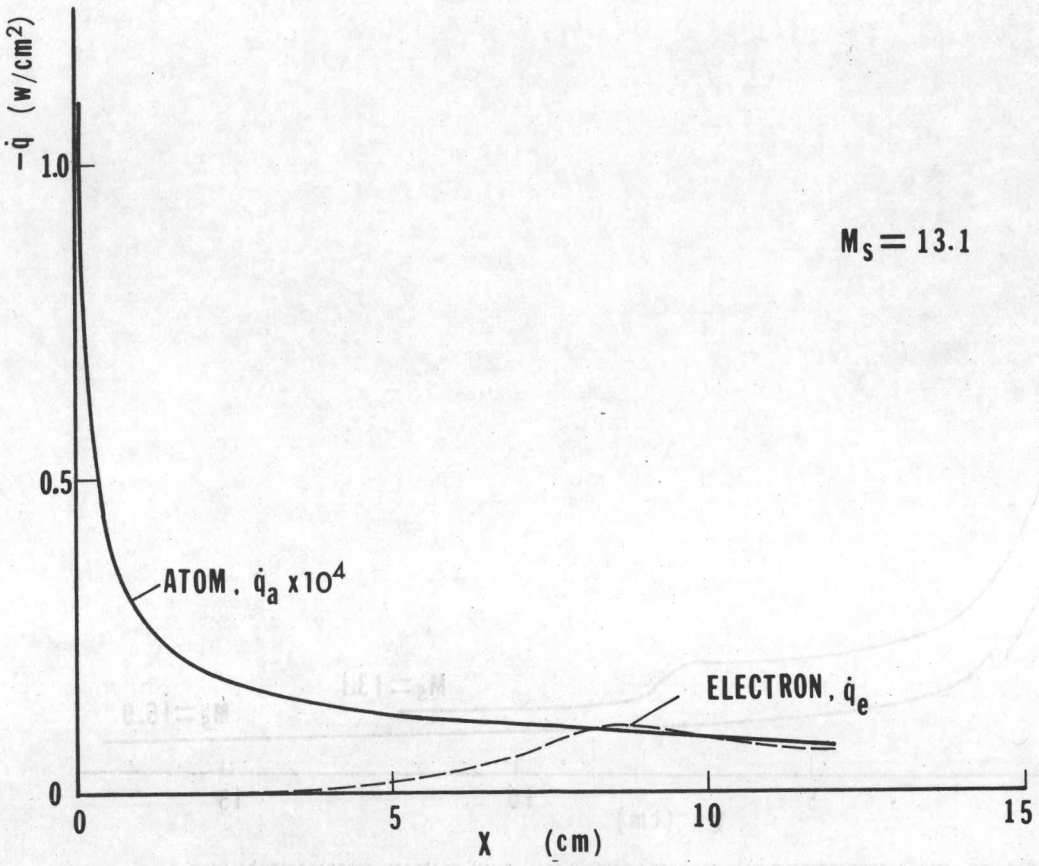

FIG. B11(a) VARIATIONS OF SIDEWALL BOUNDARY LAYER HEAT TRANSFER DUE TO ATOMS $\dot{q}_a$ AND ELECTRONS $\dot{q}_e$ WITH DISTANCE X FOR (a) M_s = 13.1, p_o = 5.16 TORR AND T_o = 300 K, AND (b) M_s = 15.9, p_o = 5.10 TORR AND T_o = 298 K.

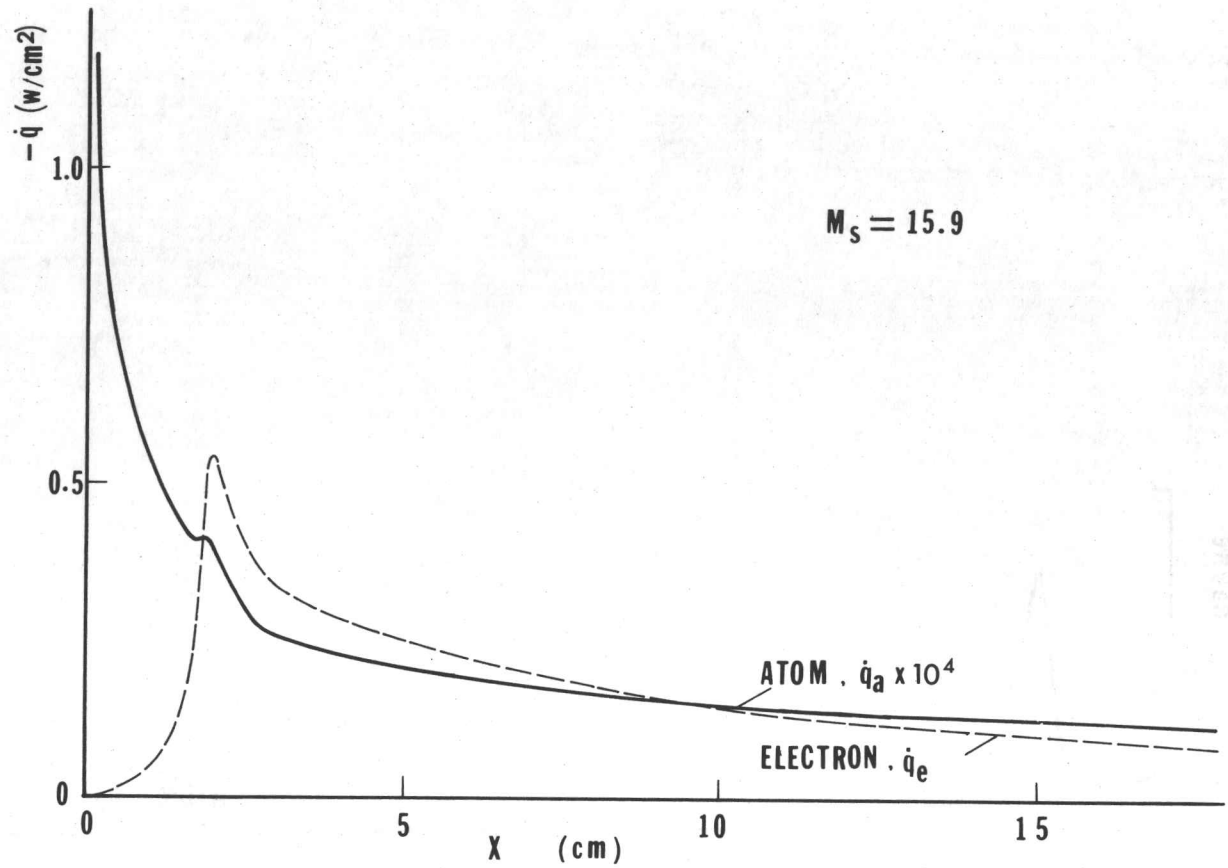

FIG. B11(b) VARIATIONS OF SIDEWALL BOUNDARY LAYER HEAT TRANSFER DUE TO ATOMS $\dot{q}_a$ AND ELECTRONS $\dot{q}_e$ WITH DISTANCE X FOR (a) M_s = 13.1, p_o = 5.16 TORR AND T_o = 300 K, AND (b) M_s = 15.9, p_o = 5.10 TORR AND T_o = 298 K.

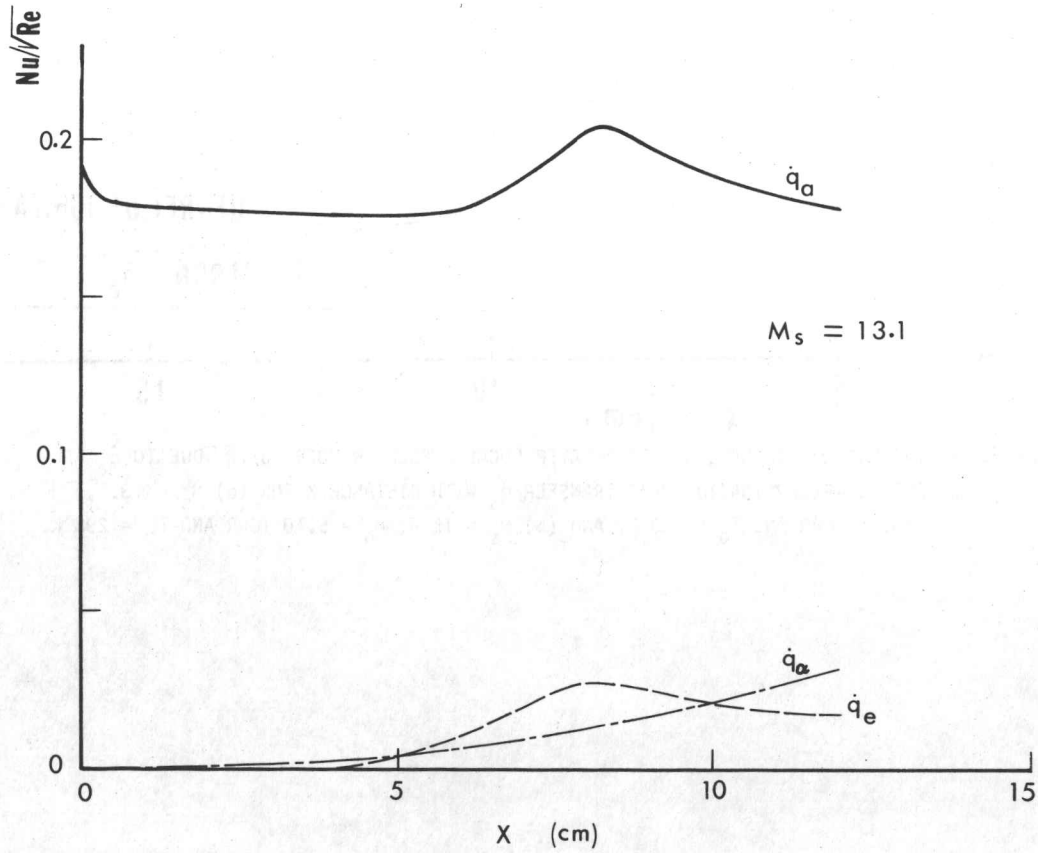

FIG. B12(a) VARIATIONS OF SIDEWALL BOUNDARY LAYER LOCAL NUSSELT NUMBER Nu/$\sqrt{Re}$ DUE TO $\dot{q}_a$ AND $\dot{q}_e$ AND ION-RECOMBINATION HEAT-TRANSFER $\dot{q}_\alpha$ WITH DISTANCE X FOR (a) M_s = 13.1, p_o = 5.16 TORR AND T_o = 300 K, AND (b) M_s = 15.9, p_o = 5.10 TORR AND T_o = 298 K.

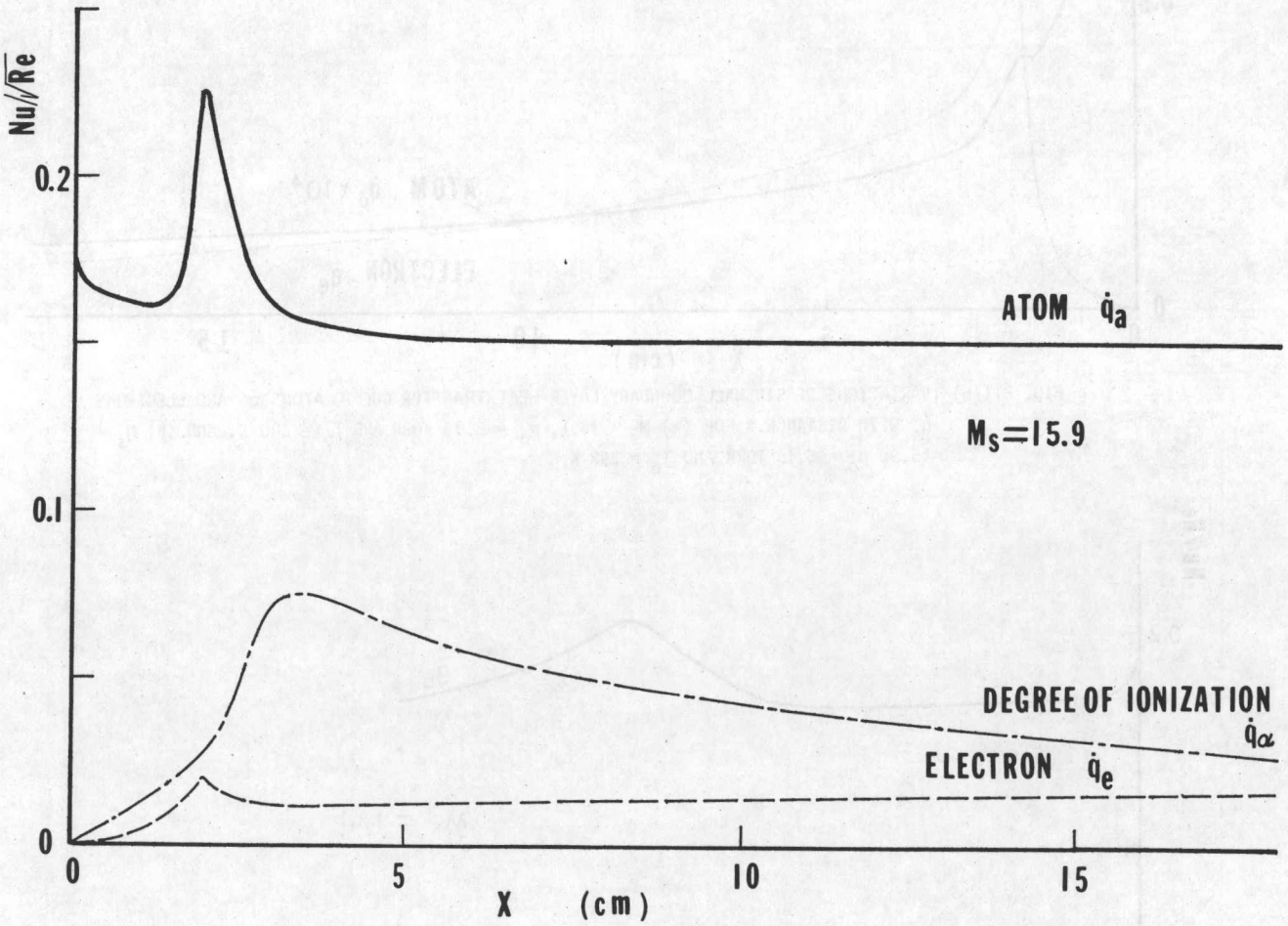

FIG. B12(b) VARIATIONS OF SIDEWALL BOUNDARY LAYER LOCAL NUSSELT NUMBER $Nu/\sqrt{Re}$ DUE TO $\dot{q}_a$ AND $\dot{q}_e$ AND ION-RECOMBINATION HEAT-TRANSFER $\dot{q}_\alpha$ WITH DISTANCE X FOR (a) M_s = 13.1, p_o = 5.16 TORR AND T_o = 300 K, AND (b) M_s = 15.9, p_o = 5.10 TORR AND T_o = 298 K.

UTIAS Report No. 233

Institute for Aerospace Studies, University of Toronto (UTIAS)
4925 Dufferin Street, Downsview, Ontario, Canada, M3H 5T6

Takayama, K., Liu, W. S. Approx. 60 pages 2 tables 35 figures

1. Shock-wave structure 2. Laminar boundary layer 3. Ionizing argon
4. Shock-tube flow

I. Takayama, K., Liu, W. S. II. UTIAS Report No. 233

Analyses are made of the mutual interactions between shock structure and the sidewall laminar boundary-layer and their effects on the quasi-steady flat-plate laminar boundary layer in ionizing argon shock-tube flows. The mutual interactions are studied using effective quasi-one-dimensional equations derived from an area-averaged-flow concept in a finite-area shock tube. The effects of mass, momentum and energy non-uniformities and the wall dissipations in the ionization and relaxation regions on the argon shock structure are discussed. The new results obtained for shock structure, shock-tube laminar sidewall and quasi-steady flat-plate boundary-layer flows are compared with dual-wavelength interferometric data obtained from the UTIAS 10 cm x 18 cm Hypervelocity Shock Tube. It is shown that the difference between the results obtained from the present method and those obtained by Enomoto based on Mirels' perfect-gas boundary-layer solutions are significant for lower shock Mach numbers ($M_s \sim 13$) where the relaxation lengths are large (~ 10 cm). In general, the present results agree better with our experimental data than our previous results for uncoupled ionizing flows.

Available copies of this report are limited. Return this card to UTIAS, if you require a copy.

UTIAS Report No. 233

Institute for Aerospace Studies, University of Toronto (UTIAS)
4925 Dufferin Street, Downsview, Ontario, Canada, M3H 5T6

Takayama, K., Liu, W. S. Approx. 60 pages 2 tables 35 figures

1. Shock-wave structure 2. Laminar boundary layer 3. Ionizing argon
4. Shock-tube flow

I. Takayama, K., Liu, W. S. II. UTIAS Report No. 233

Analyses are made of the mutual interactions between shock structure and the sidewall laminar boundary-layer and their effects on the quasi-steady flat-plate laminar boundary layer in ionizing argon shock-tube flows. The mutual interactions are studied using effective quasi-one-dimensional equations derived from an area-averaged-flow concept in a finite-area shock tube. The effects of mass, momentum and energy non-uniformities and the wall dissipations in the ionization and relaxation regions on the argon shock structure are discussed. The new results obtained for shock structure, shock-tube laminar sidewall and quasi-steady flat-plate boundary-layer flows are compared with dual-wavelength interferometric data obtained from the UTIAS 10 cm x 18 cm Hypervelocity Shock Tube. It is shown that the difference between the results obtained from the present method and those obtained by Enomoto based on Mirels' perfect-gas boundary-layer solutions are significant for lower shock Mach numbers ($M_s \sim 13$) where the relaxation lengths are large (~ 10 cm). In general, the present results agree better with our experimental data than our previous results for uncoupled ionizing flows.

Available copies of this report are limited. Return this card to UTIAS, if you require a copy.

UTIAS Report No. 233

Institute for Aerospace Studies, University of Toronto (UTIAS)
4925 Dufferin Street, Downsview, Ontario, Canada, M3H 5T6

Takayama, K., Liu, W. S. Approx. 60 pages 2 tables 35 figures

1. Shock-wave structure 2. Laminar boundary layer 3. Ionizing argon
4. Shock-tube flow

I. Takayama, K., Liu, W. S. II. UTIAS Report No. 233

Analyses are made of the mutual interactions between shock structure and the sidewall laminar boundary-layer and their effects on the quasi-steady flat-plate laminar boundary layer in ionizing argon shock-tube flows. The mutual interactions are studied using effective quasi-one-dimensional equations derived from an area-averaged-flow concept in a finite-area shock tube. The effects of mass, momentum and energy non-uniformities and the wall dissipations in the ionization and relaxation regions on the argon shock structure are discussed. The new results obtained for shock structure, shock-tube laminar sidewall and quasi-steady flat-plate boundary-layer flows are compared with dual-wavelength interferometric data obtained from the UTIAS 10 cm x 18 cm Hypervelocity Shock Tube. It is shown that the difference between the results obtained from the present method and those obtained by Enomoto based on Mirels' perfect-gas boundary-layer solutions are significant for lower shock Mach numbers ($M_s \sim 13$) where the relaxation lengths are large (~ 10 cm). In general, the present results agree better with our experimental data than our previous results for uncoupled ionizing flows.

Available copies of this report are limited. Return this card to UTIAS, if you require a copy.

UTIAS Report No. 233

Institute for Aerospace Studies, University of Toronto (UTIAS)
4925 Dufferin Street, Downsview, Ontario, Canada, M3H 5T6

Takayama, K., Liu, W. S. Approx. 60 pages 2 tables 35 figures

1. Shock-wave structure 2. Laminar boundary layer 3. Ionizing argon
4. Shock-tube flow

I. Takayama, K., Liu, W. S. II. UTIAS Report No. 233

Analyses are made of the mutual interactions between shock structure and the sidewall laminar boundary-layer and their effects on the quasi-steady flat-plate laminar boundary layer in ionizing argon shock-tube flows. The mutual interactions are studied using effective quasi-one-dimensional equations derived from an area-averaged-flow concept in a finite-area shock tube. The effects of mass, momentum and energy non-uniformities and the wall dissipations in the ionization and relaxation regions on the argon shock structure are discussed. The new results obtained for shock structure, shock-tube laminar sidewall and quasi-steady flat-plate boundary-layer flows are compared with dual-wavelength interferometric data obtained from the UTIAS 10 cm x 18 cm Hypervelocity Shock Tube. It is shown that the difference between the results obtained from the present method and those obtained by Enomoto based on Mirels' perfect-gas boundary-layer solutions are significant for lower shock Mach numbers ($M_s \sim 13$) where the relaxation lengths are large (~ 10 cm). In general, the present results agree better with our experimental data than our previous results for uncoupled ionizing flows.

Available copies of this report are limited. Return this card to UTIAS, if you require a copy.